Inelastic X-ray Scattering as a Probe for Temperature of Transient States

Dissertation
zur Erlangung des Doktorgrades
an der Fakultät für Mathematik, Informatik und Naturwissenschaften
Fachbereich Physik
der Universität Hamburg

vorgelegt von

Lennart Paul Wollenweber

Hamburg

2023

Promotionsinformationen

Gutachter/innen der Dissertation:	Prof. Dr. Nina Rohringer Dr. Ulf Zastrau
Zusammensetzung der Prüfungskommission:	Prof. Dr. Nina Rohringer Dr. Ulf Zastrau Prof. Dr. Beata Ziaja-Motyka Dr. Michael Martins Prof. Dr. Jochen Liske
Vorsitzende/r der Prüfungskommission:	Prof. Dr. Jochen Liske
Datum der Disputation:	23.04.2024
Vorsitzender des Fach-Promotionsausschusses PHYSIK:	Prof. Dr. Markus Drescher
Leiter des Fachbereiches PHYSIK:	Prof. Dr. Wolfgang J. Parak
Dekan der Fakultät für MIN:	Prof. Dr.-Ing. Norbert Ritter

Zusammenfassung

Ein beträchtlicher Teil der experimentellen Forschung an Röntgen-Freie-Elektronen-Lasern (XFELs) widmet sich der Erforschung von kurzlebigen, extremen Materiezuständen, die oft durch Laser erzeugt werden. Diese Zustände, wie hochionisierte Plasmen und Hochdruckzustände ähnlich dem Inneren von Planeten, existieren nur für Nanosekunden oder kürzer. Dennoch spielen ihre Eigenschaften entscheidende Rollen unter anderem in der Entwicklung von Planeten und der Zündung von Trägheitsfusion. Ein umfassendes Verständnis dieser extremen Zustände erfordert Kenntnisse aller thermodynamischen Parameter, wobei sich die Temperaturmessung als besonders anspruchsvolle Aufgabe herausgestellt hat.

Diese Arbeit beschreibt, wie hochauflösende inelastische Röntgenstreuung (IXS) an XFELs als Diagnose für die Temperaturmessung kurzlebiger transienter Zustände etabliert wird. Der erste Abschnitt präsentiert die Ergebnisse der Inbetriebnahme des IXS-Aufbaus am High Energy Density (HED) wissenschaftlichen Instrument am European XFEL, begleitet von einer statischen Machbarkeitsmessung der Temperatur in Diamant unter Verwendung von *detailed balance* der Phononen.

Anschließend erforscht die Arbeit die Anpassung des *detailed balance*-Prinzips für dynamisch getriebene Proben. In einem Experiment wird ein Laser mit hoher Wiederholungsrate eingesetzt, um Eisen in einen transienten Zustand bei erhöhten Temperaturen zu versetzen.

Schließlich werden experimentelle Daten präsentiert, bei denen hochauflösende inelastische Röntgenstreuung zur Messung der Doppler-Verbreiterung verwendet wird und so Temperaturinformationen durch die Maxwell-Boltzmann-Geschwindigkeitsverteilung zugänglich werden. Die Ergebnisse zeigen die Temperaturentwicklung der Ionen in einer Goldfolie nach Anregung mit einem ultrakurzen Laserpuls und ermöglichen Schlussfolgerungen über den Elektron-Ion-Kopplungsparameter. Diese Arbeit trägt zur Weiterentwicklung von IXS als Diagnosetechnik bei, um die komplexen Temperaturdynamiken kurzlebiger Zustände zu erfassen, die in intensiven Laser-Festkörper-Wechselwirkungen auftreten.

Abstract

A significant portion of experimental research conducted at X-ray Free-Electron Lasers (XFELs) is dedicated to the exploration of transient and extreme states of matter, often generated by lasers. These states, such as highly ionized plasmas and high-pressure matter similar to planetary interiors, exist only for nanoseconds or less. Yet, their properties play crucial roles amongst others in planetary evolution and inertial confinement fusion (ICF) target ignition. A comprehensive understanding of these extreme states requires knowledge of all thermodynamic parameters, with temperature measurement emerging as a particularly challenging task.

This thesis describes endeavors to establish high-resolution inelastic X-ray scattering (IXS) at XFELs as a diagnostic tool for the temperature measurement of short-lived transient states. The initial section presents the commissioning results of the IXS setup at the High Energy Density (HED) scientific instrument at the European XFEL, accompanied by a static proof-of-principle temperature measurement in diamond utilizing the detailed balance of phonons.

Subsequently, the thesis explores the adaptation of the detailed balance technique to dynamically driven samples. In a high-repetition rate experiment, a laser is employed to excite iron to a short-lived state at elevated temperatures.

Finally, experimental data is presented wherein high-resolution IXS is utilized to measure Doppler broadening, providing temperature information through the Maxwell-Boltzmann velocity distribution. The results showcase the temperature evolution of the ions in a gold foil following excitation with an ultra-short laser pulse, enabling conclusions about the electron-ion coupling parameter. This work contributes to the advancement of IXS as a diagnostic tool for unraveling the complex temperature dynamics of transient states created in intense laser-solid interactions.

Eidesstattliche Versicherung /

Declaration on oath

Hiermit versichere ich an Eides statt, die vorliegende Dissertationsschrift selbst verfasst und keine anderen als die angegebenen Hilfsmittel und Quellen benutzt zu haben.

Hamburg, den 13.12.2023 Unterschrift: _____

Acknowledgements

I extend my heartfelt gratitude to all those who have been part of my journey over the past five years, culminating in the completion of this thesis. Foremost, I am deeply indebted to my supervisor at the European XFEL, Ulf Zastrau. He took me under his guidance at a time when my knowledge of HED science was barely existing, and his mentorship has been instrumental in my growth over the years. I express sincere appreciation for his unwavering support, trust, patience, and motivation.

I am thankful to Nina Rohringer for her interest and support in this project, even though most of the work happened some distance away.

Special thanks go to Karen Appel and Thomas Preston for their patient responses to my numerous questions, consistent support during beamtimes and setup work, and the many insightful conversations within the wooden halls of XTOB.

I express my gratitude to Bob Nagler and Thomas White for their generous invitation to participate in their experiments, providing access to valuable data that contributed significantly to this work.

I would like to acknowledge our external collaborators Gianluca Gregori, Justin Wark, Oliver Karnbach, Emma McBride, Ben Ofori-Okai, and Adrien Descamps for their invaluable input, advise, and support during our experiments at the HED instrument.

Further, I would like to thank Motoaki Nakatsutsumi, Jan-Patrick Schwinkendorf, and Hauke Höppner for their sustained effort in setting up the lasers for our experiments and all the practical tricks about laser work I could learn from you.

I am grateful to Erik Brambrink, Victorien Bouffetier, and Mohammadreza Banjafar for their support and advice on hydrodynamic and particle-in-cell simulations.

My time at the European XFEL was greatly enhanced by the collaborative spirit of the members of the HED and HIBEF teams, and I extend my thanks to all involved.

I owe much to my fellow PhD students and office mates Markus Schölmerich, Nicole Jahnke, Christian Plückthun, Anand Dwivedi, and Khachiwan Buakor for the countless fruitful work discussions and the equally beneficial (and much more frequent) off-topic conversations. And of course Johannes Kaa, even though he sat in a different office most of the time. I also thank all other PhD students at the European XFEL, past and present,

for the enjoyable times we shared both on and off campus.

Lastly, I want to express my gratitude to my family—my parents Elke and Harald, and my sisters Lisa, Miriam, and Melanie—for their interest in my work, and for their encouragement and occasional nudges when needed.

Contents

Chapter 1

Introduction

This thesis details the endeavors undertaken over the past five years to develop and establish high-resolution inelastic X-ray scattering (IXS) as a diagnostic tool for transient matter states at X-ray Free-Electron Lasers (XFELs), with a particular emphasis on using IXS to measure temperature in warm dense matter states.

Warm dense matter states exist at the boundary between solid-state matter and plasmas, characterized by thermal energy levels high enough to match electric binding energies in solids, resulting in temporary losses of atomic order [1]. Despite being uncommon in our everyday experience, warm dense matter is a prevalent state throughout the universe, found inside planets and influencing their geological behavior, such as Earth's dynamo effect [2]. Further occurrences on Earth, besides meteor impacts [3,4], are mostly artificially generated for research and technology.

Warm dense matter is produced in the interaction of intense lasers or particle beams with solid matter [5–7]. It therefore appears during basic research experiments, production of new materials [8–10], and industrial welding [11,12]. Another important occurrence in research and technology is during the compression of inertial confinement fusion (ICF) targets [13] for future energy production.

A complete characterization of a warm dense matter state requires knowledge of its density, pressure, temperature, and ionisation state. Obtaining all these parameters allows the formulation of an equation of state (EOS) for the measured conditions [14,15]. As most experiments are unable to measure all parameters simultaneously, the missing values are often taken from tabulated EOS values. Most of the times, the tables themselves are only interpolated from known conditions and not measured for every point. This is a strong motivation to conduct accurate measurements at points within the interpolated regions to obtain more reliable material parameters from EOS tables.

As the methods employed in laboratories to produce warm dense matter states result in short-lived, rapidly changing systems usually in a small volume, the diagnostics are not trivial. Most electronics lack the temporal resolution to keep pace with the evolution of the produced states, optical methods are usually only surface

sensitive, and the small volumes allow only low emission yields. Never mind physically attaching a probe to the target volume.

Of these four thermodynamic quantities, the easiest measurement to perform is probably to probe the density. It can be done with any bulk structure probe, usually x-ray, neutron, or electron diffraction, which simultaneously informs about whether the material is still solid or already molten [16–19]. For the short-lived, transient warm dense matter states produced in laboratory experiments, the recently available ultrafast x-ray [20] and electron probes [21, 22] are a great diagnostic tool. The intense femtosecond pulses almost take a still frame image of the ion positions, which yields an unmatched temporal resolution in dynamic systems.

For the measurement of pressure in high-energy laser experiments, velocity interferometer system for any reflector (VISAR) [23–25] has become the standard method. It requires that the rear surface of the sample is capable of reflecting a laser into an interferometer. The movement of the surface at shock breakout produces changes in interference due to the Doppler effect. This can be used to calculate the surface velocity and can be related to the pressure inside the systems via the Rankine-Hugoniot equations [26, 27].

The ionisation state of the sample system can be determined from x-ray emission spectroscopy, if the photon energy is above an absorption edge and thus excites fluorescent radiation, or if an ionic transition is excited resonantly.

Lastly, the temperature comprises a parameter very difficult to measure. In high-temperature (keV) plasma studies, streaked optical pyrometry (SOP) is usually employed to determine the temperature. SOP collects the thermal emission of the sample with a spectrometer coupled to a streak camera or colour-filtered diode array to determine its black body temperature. This method works well for hot and/or long existing contained plasmas but fails due to lacking time resolution of the electronics below the nanosecond time scale. Additionally, the signal level drastically drops when the temperature is lower at only some eV, which is the case for warm dense matter, as the emissivity of the sample given by the Stefan-Boltzmann law scales with T^4 [28, 29]. Also, the method is only sensitive to optical radiation emitted by the surface and contains no information about the volumetric conditions.

Starting from the other end of the temperature range, a method often used in solid-state physics to determine temperature is the Debye-Waller effect in the intensity of a x-ray diffraction signal. As the order inside a crystalline material diminishes due to rising thermal motion of the atoms, the intensity of the crystalline diffraction line drops. This change of intensity relates the materials temperature to its Debye-temperature [30, 31]. Using this method requires the knowledge of the Debye-temperature, which unfortunately changes with pressure and temperature itself [32, 33]. In addition, the diffraction intensity is also dependent on the micro structure of the sample, which can change in unpredictable ways when a shock wave passes through the material [34]. This makes the method even more unreliable in laser shock experiments. Lastly, it completely fails for non crystalline samples or when the sample reaches melt conditions.

The work presented in this thesis follows the approach of using inelastic x-ray scattering from bound elec-

trons, co-moving with the atoms, to determine the samples temperature. This can be achieved by two different techniques. First is collective scattering from phonons in crystalline solids or ion acoustic modes in amorphous materials [35, 36]. X-ray photons scattering from these collective modes can gain or lose energy, typically on the few meV scale. Spectrally resolving the scattered radiation gives rise to Stokes and anti-Stokes peaks, which correspond to the creation and annihilation of a phonon, respectively [37, 38]. The intensity ratio of these two features is a direct measurement of the temperature via the detailed balance principle [39]. This measurement can yield additional information about the sample system, like speed of sound or thermal diffusivity, too.

The second approach to measure temperature with IXS is to go to higher momentum transfers into the non-collective regime and measure the Doppler broadening of the individual atomic motion [40]. If the sample system follows a Maxwell-Boltzmann distribution, the measurement of the velocity distribution is directly connected to a temperature. The spectral broadening due to the thermal motion for warm dense matter states lies similarly to the phonons and ion acoustic modes in the tens of meV range.

Both methods therefore require a spectrometer with high resolving power to measure this effect. As typical x-ray energies are on the order of keV, a spectral bandwidth of $\Delta E/E = 10^{-5}$ or better is required. This means for all common x-ray sources that monochromatisation to a high degree is necessary. So is the typical bandwidth of an undulator source on the order of 10^{-2}. As the inelastic scattering process itself occurs with a small probability, the measurement requires a huge photon flux from the source. Together with the precise timing requirements due to the short-lived nature of laser generated states, XFELs are the only suitable x-ray source for this kind of measurements. Their highly brilliant x-ray pulses can deliver $\sim 10^{12}$ photons within only a few tens fs [41]. With monochromatisation and low scattering cross section, they represent the only possibility to obtain an IXS signal from highly transient systems.

1.1 Structure of this Thesis

The main part of this thesis begins with an introduction to the theory behind the concepts touched upon within this work. It starts in chapter two with the interaction of high-power and high-energy lasers with solids as a way to generate warm dense matter states in the laboratory. It follows a brief overview of XFELs, their radiation generation and properties as a well suited tool to diagnose these transient laser generated states. Next is the theory dynamical diffraction and high-resolution inelastic x-ray scattering and how it can be applied as a probe for warm dense matter states, especially as a temperature diagnostic. The chapter is closed by a description of the technical realization of a high-resolution IXS instrument and a general overview of the two scientific instruments used in this thesis.

Next, the third chapter will briefly summarise the geophysical relevance of iron and motivate its use as a sample material in high-pressured experiments.

The fourth chapter will present and discuss the experiments conducted within the scope of this work. First,

the characterization of the IXS setup at the high energy density (HED) instrument and a demonstration of its capability to measure temperature lead by Gianluca Gregori (Univ. Oxford, UK) and Ulf Zastrau (European XFEL, GER) in collaboration with Emma McBride (SLAC, Univ. Belfast, UK) and Thomas White (Univ. Reno, NV, US) and others. Second, an experiment to investigate laser excited iron, lead by Gianluca Gregory, Oliver Karnbach (Univ. Oxford, UK), and myself. And third, two experiments to study the electron-ion equilibration rate in warm dense matter, lead by Bob Nagler (SLAC, CA, US) and Thomas White (Univ. Reno, NV, US).

The final chapter gives a summary of the performed work and outlines possible future experiments using high-resolution IXS to explore transient laser generated states at XFELs.

Chapter 2

Theoretical Concepts

This chapter introduces some of the concepts behind the physical processes covered by this work. It starts with the interaction of powerful laser pulses with solids, differentiating between ultra-short pulses of fs duration and longer pulses on the ns scale.

The next section treats the theory of x-ray scattering with a focus on the inelastic scattering process from phonons. It is followed by an introduction on how inelastic x-ray scattering can be used to measure ion temperature, both in the collective and non-collective regime.

The final section deals with the theoretical and technical aspects of the components necessary to perform high-resolution inelastic x-ray scattering experiments on transient states. It starts with free-electron lasers as a suitable x-ray source, goes over the used x-ray optics like monochromators and focusing devices, and ends with the x-ray detector built into the spectrometer.

2.1 Laser driven extreme states

Laser technology has made great advances since its invention in 1960 [42]. Today, pulsed lasers have been shown to be a reliable tool to generate extreme states of matter in the laboratory. Developments for ever higher pulse energy have lead to the availability of ns pulses with MJ energy capable of generating Gbar pressure states [43] and nuclear fusion conditions [44].

With the invention of chirped pulse amplification [45], it became possible to generate energetic laser pulses on fs timescales (cf. also Nobel prize in physics 2018). Peak power levels of 10 PW are possible [46] and 100 TW can be delivered to experiments at a repetition rate of 10 Hz [47]. This section will give a brief introduction on how such intense lasers interact with matter. For simplicity and technical reasons, we assume all laser-solid interactions to occur in vacuum. A more detailed foundation can be read e.g. in books by Gibbon [48], Fortov [49], and Drake [50].

2.1.1 Femtosecond laser drive

The interactions of intense lasers with matter have in common, that atoms are rapidly ionised by the strong electric fields. Then, the free electrons are accelerated in the light field. The energy the electrons attain depends on the intensity and determines further physical processes.

Ionisation can happen in several different ways. On the lower end of the intensity scale ($> 10^{10} \frac{W}{cm^2}$) is multi-photon absorption. Here, a single electron absorbs enough photons before it relaxes back into its ground state that the gained energy surpasses the ionisation energy E_{ion}. Including above-threshold ionisation [51], the final electron energy E_f is expressed as

$$E_f = (n+s)\hbar\omega - E_{ion}, \tag{2.1}$$

where n is the number of photon needed for multi photon ionisation, s the remaining energy, ω the light circular frequency, and $\hbar$ the reduced Planck constant (and consequently, $\hbar\omega$ being the photon energy of a single photon).

At higher intensities ($> 10^{14} \frac{W}{cm^2}$), the model for the laser-matter interaction is changed from a multi photon picture to the description of the interaction between the electric fields of the laser pulse and the Coulomb field of the atom, respectively. Here, the laser disturbs the electric binding of the electrons to the nucleus by distorting the atomic binding potential so strongly, that electrons can tunnel through the potential barrier (tunnel ionisation) or in case of even stronger fields just straight up leave the atom (over-barrier ionisation). As optical wavelengths are large compared with an atom, the disturbance to the binding potential can be approximated by a linear term. The modified Coulomb potential is

$$V(x) = -\frac{Ze^2}{x} - e\varepsilon x. \tag{2.2}$$

Over-barrier ionisation occurs, when the modifying field reaches a critical value

$$\varepsilon_{crit} = \frac{E_{ion}^2}{4Ze^3}. \tag{2.3}$$

With this expression as the laser peak field strength, the corresponding intensity is given by

$$I \simeq 4 \times 10^9 \left(\frac{E_{ion}}{[eV]}\right)^4 Z^{-2} \left[\frac{W}{cm^2}\right]. \tag{2.4}$$

The ionisation rates for tunneling can be obtained through quantum mechanical calculations [52]. In dense systems like a solid, collision ionisation will play an important role after enough initial free electrons are created

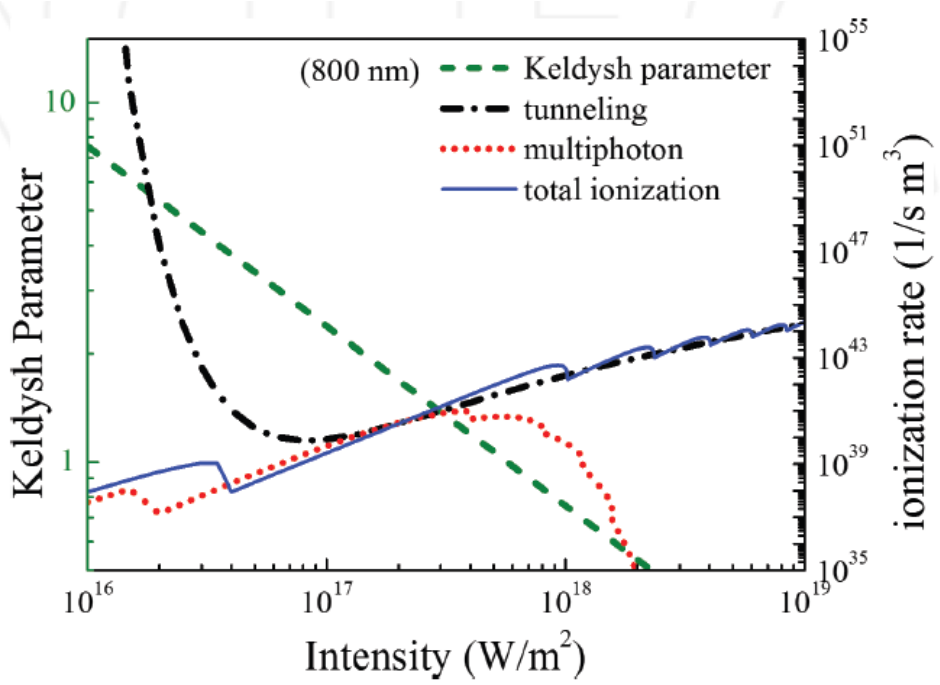

Figure 2.1: Calculated total ionisation rate (blue, solid) with separated multi photon (red, dotted) and tunnel ionisation (black, dash-dotted) components for different laser intensities under 400 nm irradiation. The corresponding Keldysh parameter (green, dashed) is shown, too. For $\gamma \approx 1.5$, the ionisation rates are of similar strength. Figure from Pan *et al.* [53].

by the laser field.

To determine which of the described models is the applicable process to describe intense laser photoionisation, one can calculate the so-called Keldysh parameter γ

$$\gamma = \omega\sqrt{\frac{2E_{ion}}{I_L}} \sim \sqrt{\frac{E_{ion}}{U_p}} \quad U_p = \frac{e^2E_L^2}{4m_e\omega^2}. \tag{2.5}$$

Here, U_p is called the ponderomotive potential and gives the average energy an electron obtains in the oscillating electric field of the laser. When $\gamma >> 1$, multi photon ionisation is the dominant process, with $\gamma << 1$ tunnel and over-barrier ionisation. As an example, for polymethylmethacrylate (PMMA), multi photon and tunnel ionisation rate are equal at $\gamma \approx 1.5$ [53] (Fig. 2.1).

Due to the multiple absorption events, after a few laser cycles a plasma will emerge at the surface of an irradiated solid with a plasma frequency ω_p

$$\omega_p = \sqrt{\frac{4\pi n_e e^2}{m_e}}, \tag{2.6}$$

with free-electron density n_e, elementary charge e, and electron mass m_e. The only free parameter here is the free-electron density n_e. Inverse plasma frequencies in a solid density plasma are in the sub-femtosecond range, meaning an electron can react on these time scales (cf. also Nobel prize in physics 2023).

Hydrodynamic expansion happens of the timescale of sound speed (of order km/s or few tens of picometer (pm) in 50 fs), due to its ultra-short (fs) duration, the laser pulse will interact with this solid density surface plasma before huge repositioning of the ions can happen. This results in the lasers electric filed forming a standing wave in front of the plasma with a small penetration into it, the skin depth,

$$l_s = \frac{c}{\omega_p}. \tag{2.7}$$

Note that for highly relativistic intensities exceeding $10^{18}\,\mathrm{W/cm^2}$ (resulting in the kinetic energy of the electrons being a multiple of their rest mass), a relativistic correction becomes necessary, and in case of a high collisionality, likewise corrections to the above formula can be made.

Electron - ion equilibration

The interaction with an intense ultra-short laser pulse leaves a solid target in a strong non-equilibrium: Through a variety of absorption mechanism a population of hot electrons is generated at the interaction site while the bulk remains unaffected. These hot electrons rapidly thermalise the electron system around the heating spot through electron-electron collisions [54, 55]. This process typically happens in solids on scales smaller 1 ps. The thermalised electrons diffuse into the bulk of the material along the thermal gradient. While moving, the hot electron bath loses energy due to electron phonon coupling. This process can be described by a two-temperature model [56] (TTM), which is a system of coupled partial differential equations for both the electron and ion subsystem

$$C_e \frac{\partial T_e}{\partial t} = \nabla(K_e \nabla T_e) - g_{ei}(T_e - T_i) + S_e(t) \tag{2.8}$$

$$C_i \frac{\partial T_i}{\partial t} = \nabla(K_i \nabla T_i) + g_{ei}(T_e - T_i). \tag{2.9}$$

Here, C_e and C_i are the specific heat capacities of electrons and ions, K_e and K_i the thermal conductivities, and $S_e(t)$ the heat source (laser pulse). g_{ei} is coupling constant that governs the heat transfer from the electron system to the ions due to the temperature difference. This occurs within a few ps for most materials (Fig. 2.2). After the electrons and ions are thermalised within the diffusion range of the electrons, heat transport over the lattice distributes the energy to further parts of the bulk.

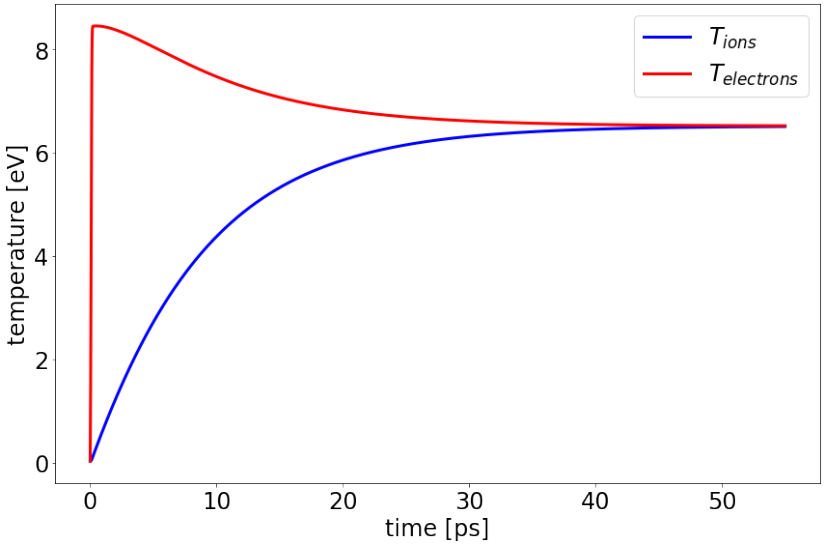

Figure 2.2: Generic temperature evolution after short pulse laser interaction in the two-temperature model with a constant coupling parameter. The electron system (blue) absorbs the laser energy and thermalises within a few hundred fs. Through collisions and electron-phonon coupling, the electrons lose energy to the ion system (red) until both systems reach thermal equilibrium. This occurs on a ps timescale.

In this thesis, experiments which use fs laser pulses to heat electrons and then measure the ion temperature evolution, and data interpretation using a (modified) two-temperature model, are discussed in chapter 4.3.

2.1.2 Nanosecond laser drive

When an intense laser pulse interacts with an absorbing surface for a longer time than fs, the high energy input begins to vaporise atoms from the surface, which is called ablation. If the intensity is even higher, this gas in front of the surface is ionised into a plasma cloud, which has less density further away from the surface (i.e., a density gradient). The laser is then no longer absorbed at the targets surface, but somewhere within the ablation plasma. The exact location is determined by the plasma critical density, meaning the density of the electrons corresponds to a plasma frequency ω_p which matches the laser light frequency. Further out, at lower density, electrons are too slow to follow the laser light oscillations and light can penetrate. Beyond the critical plasma density, electrons can follow the oscillations of the laser light and shield it. The density at the critical point is typically 10-100 times lower than the solid density of the target. Via electron thermal conduction, the continuously impinging laser energy is conducted through the plasma to the solid target.

At the ablation front, the energy from the plasma cloud heats up the solid density target, which vaporises and feeds into the plasma. The material moves through the plasma to the critical point and then escapes further into the surrounding vacuum. The pressure from the plasma acts onto the target and pushes a pressure wave into

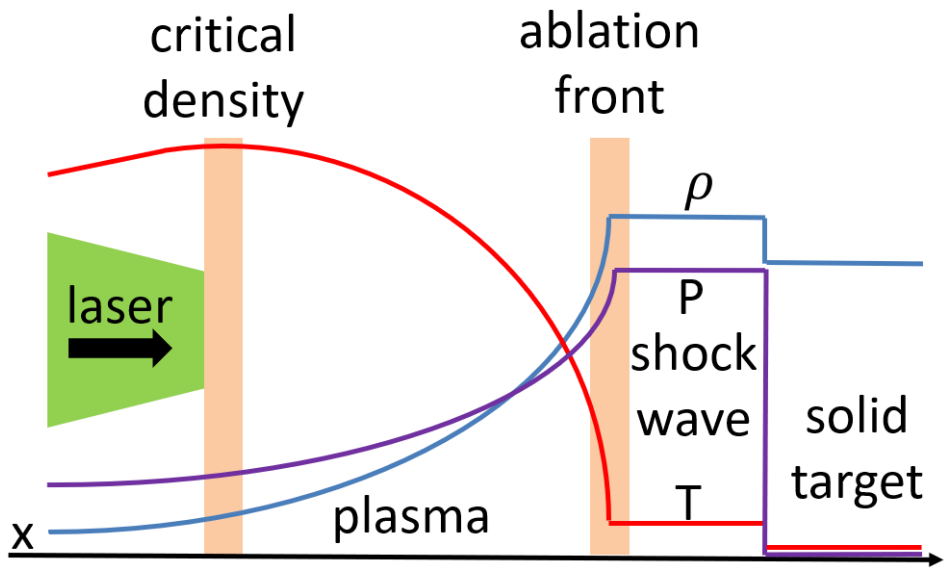

Figure 2.3: Sketch of the 1-dimensional interaction of an intense long pulse laser with a solid target. After the first interaction, the laser ionises the ablated material into a plasma. From then on, the laser is absorbed within the plasma, which transports the energy to the sample. At the ablation front, the target is heated enough to vaporise and feed into the plasma. Through the pressure of the plasma, a shock wave is sustained inside the solid target. A schematic profile of density ρ (blue), pressure p (purple), and temperature T (red) is also shown. Figure adapted from Fortov [49].

the solid (Fig 2.3).

Under a simplistic view neglecting non-linear effects in the absorption and light reflection by the plasma, the maximum reachable pressure is given by

$$p_{max} = I^{\frac{2}{3}} \rho_c^{\frac{1}{3}}. \tag{2.10}$$

Here, I is the laser intensity and ρ_c the critical density. It is also apparent, that in this simple model the pressure is not hugely dependant on any material parameters. Laser shock experiments are therefore a good method to obtain comparable data from different materials with the same setup, in contrast to impact or detonation experiments.

Resonant absorption of the laser should be avoided, as a huge number of hot electrons can be generated which penetrate the target and preheat it before the shock wave arrives. The temperature of these electrons can be estimated [57, 58] to be

$$T_H = 14 \left(I \left[10^{16} \frac{W}{cm^2} \right] \lambda^2 [\mu m] \right)^{\frac{1}{3}} [keV], \tag{2.11}$$

where I is the laser intensity and λ its wavelength. Many high-power lasers are operated in the infrared regime, where according to Eq. 2.11 a larger number of hot electrons are generated compared to visible wavelengths. Therefore, many shock lasers are frequency doubled or even tripled [59] to preserve the initial target conditions.

Another reason to go to shorter wavelengths/higher frequencies is the necessary laser energy to reach a certain pressure inside the target. This energy is related to the pressure and wavelength of the laser [60]

$$E \sim p^6 \lambda^{11}. \tag{2.12}$$

This is one reason why inertial confinement fusion experiments have switched their focus to indirectly driven targets, where the ablation is done through x-rays produced by irradiating a hohlraum around the target with the drive laser [13, 61].

2.2 Inelastic x-ray scattering

Non-resonant inelastic x-ray scattering (IXS) is a great tool to investigate the properties of condensed matter, liquids and plasmas. Especially at low energy transfers, it can be used to investigate phonons [35, 62] or collective modes [35, 63]. At higher energy transfers it can be connected to the dielectric function of the electron system. Here, I will give a short introduction to describe the theory for IXS as far as it is applicable to the data analysis in the thesis. A more complete derivation can be found in common textbooks, e.g. Squires [64], Schülke [65], Attwood [66], or Schwabl [67], or review articles like Burkel [68] and Sinha [69].

A multi-particle system of scattering non-relativistic electrons without spin contributions can be described by a Hamiltonian which consists of a part describing the electronic system H_0 and a part describing the interaction with an electromagnetic field H_{int}, $H = H_0 + H_{int}$. Neglecting photon creation and annihilation processes, the first order Hamiltonian reads

$$H = \sum_i V(\vec{r}_i) \; + \; \sum_i \frac{\vec{P}_i^2}{2m} \; + \; \frac{e^2}{2mc^2} \sum_i \vec{A}(\vec{r}) \cdot \vec{A}(\vec{r}). \tag{2.13}$$

Here, the first sum goes over the potential field at the position $\vec{r}$ of the ith electron. The second sum contains the kinetic energy of the scattering particles with mass m and momentum $\vec{P}$. Finally, the third sum, H_{int}, describes the scattering interaction between particles and electromagnetic wave where e is the elemental charge, c the speed of light, and $\vec{A}$ the vector potential. The vector potential expressed with photon creation ($a^\dagger$) and annihilation (a) operators takes the form

$$\vec{A}(\vec{r}) = L^{-3/2} \sum_{\vec{k}\alpha} c \sqrt{\frac{\hbar}{\omega_k}} \left(\vec{\varepsilon}_\alpha a_{k,\alpha}^\dagger e^{-i\vec{k}\cdot\vec{r}} + \vec{\varepsilon}_\alpha a_{k,\alpha} e^{i\vec{k}\cdot\vec{r}} \right), \tag{2.14}$$

where L^3 is a normalized volume with periodic boundaries, k the wave vector and α the polarization states with corresponding polarization vectors ε_α. The allowed photon states in this volume are wave vectors of the form $\frac{2\pi}{L}$ (x,y,z) with integer values. The number of allowed wave vectors going into the solid angle $d\Omega$ with polarization state α and energy between E' and dE' is then

$$\nu_{\vec{k}\alpha} = \vec{k}'^2 d\Omega \frac{L^3}{(2\pi)^3} \frac{1}{\hbar c}. \tag{2.15}$$

The flux ϕ of incoming photons per unit area and time is

$$\phi = \frac{c}{L^3}. \tag{2.16}$$

A parameter often used to describe scattering processes is the differential cross section, which is the current of photons scattered into a solid angle element. For a scattering process from a photon $(\vec{k},\alpha)$ and state $\mid n\rangle$ to a photon $(\vec{k}',\beta)$ and state $\mid m\rangle$, the transition probability per unit time is given by the transition matrix element W. With this, the differential cross section becomes

$$\left(\frac{d\sigma}{d\Omega}\right) = \frac{1}{\phi d\Omega}\sum_{\vec{k}'}^{d\Omega} W_{\vec{k}\alpha n\rightarrow\vec{k}'\beta m}. \tag{2.17}$$

The transition matrix element is obtained from Fermi's golden rule [70, 71]

$$\sum_{\vec{k}'}^{d\Omega} W_{\vec{k}\alpha n\rightarrow\vec{k}'\beta m} = \frac{2\pi}{\hbar}\nu_{\vec{k}'\beta}\left|\langle\vec{k}'\beta m \mid H_{int} \mid \vec{k}\alpha n\rangle\right|^2. \tag{2.18}$$

Inserting H_{int} from (Eq. 2.13) and the thermal average of the initial states and summing over all possible final states yields the partial differential cross section, the differential cross section per unit energy or double differential scattering cross section (DDSCS):

$$\left(\frac{d^2\sigma}{d\Omega dE'}\right)_{\vec{k}\alpha\rightarrow\vec{k}'\beta} = \frac{k'}{k}\left(\frac{e^2}{mc^2}\right)^2 \mid \varepsilon_\alpha^*\cdot\varepsilon_\beta \mid S(\vec{q},\omega). \tag{2.19}$$

Here, $\vec{q} = \vec{k} - \vec{k}'$ is the momentum transfer and $S(\vec{q},\omega)$ is called the dynamical structure factor, as it is explicitly dependant on the structure. For an energy transfer $\hbar\omega = E_n - E_m$, it can be written as

$$S(\vec{q},\omega) = \sum_{nm}\sum_{ij} p_n\langle n \mid e^{-i\vec{q}\cdot\vec{r}_i} \mid m\rangle\langle m \mid e^{i\vec{q}\cdot\vec{r}_j} \mid n\rangle\delta(E_n - E_m + \hbar\omega), \tag{2.20}$$

where p_n is the probability of the initial state $\mid n\rangle$ and δ the Kronecker delta. Integrating this expression over ω for a fixed incident energy and assuming small energy transfers yields the differential cross section

$$\left(\frac{d\sigma}{d\Omega}\right) = \left(\frac{e^2}{mc^2}\right)^2 \mid \varepsilon_\alpha^*\cdot\varepsilon_\beta \mid^2 S(\vec{q}) = \frac{3}{8\pi}\sigma_T \mid \varepsilon_\alpha^*\cdot\varepsilon_\beta \mid^2 S(\vec{q}), \tag{2.21}$$

where σ_T is the Thomson cross section [72, 73].

2.2.1 Collective and non-collective scattering

In a classical approach [74], the differential cross section for multiple scatterer can be expressed as

$$\left(\frac{d\sigma}{d\Omega}\right) = \langle\left|\sum_j \frac{e_j^2}{m_j c^2} e^{i\vec{q}\cdot\vec{r}_j}\right|^2\rangle \mid \varepsilon_\alpha^*\cdot\varepsilon_\beta \mid^2, \tag{2.22}$$

with $\langle\rangle$ indicating the average over all positions $\vec{r}_j$. The possible values for the position are on the order of typical length scales a in the system, like the Wigner-Seitz radius. If $qa \ll 1$, than all exponential terms within the sum can be taken as unity. Therefore, the resulting intensity of the scattered radiation scales with the number of scatterers squared times the strength of a single scatterer. This behaviour is typically called collective or coherent scattering.

$$\lim_{qa\to 0}\left(\frac{d\sigma}{d\Omega}\right) = \left|\sum_j \frac{e_j^2}{m_j c^2}\right|^2 \mid \varepsilon_\alpha^* \cdot \varepsilon_\beta \mid^2 = Z^2 \left(\frac{e^2}{mc^2}\right)^2 \mid \varepsilon_\alpha^* \cdot \varepsilon_\beta \mid^2 . \tag{2.23}$$

On the opposite, if $qa \gg 1$, then $e^{i\vec{q}\cdot\vec{r}_j}$ can assume a wide range of values, which average to zero. Thus, the intensity only scales with the number of scatterers. This is referred to as non-collective or incoherent scattering.

$$\lim_{qa\to\infty}\left(\frac{d\sigma}{d\Omega}\right) = \sum_j \left(\frac{e_j^2}{m_j c^2}\right)^2 \mid \varepsilon_\alpha^* \cdot \varepsilon_\beta \mid^2 = Z \left(\frac{e^2}{mc^2}\right)^2 \mid \varepsilon_\alpha^* \cdot \varepsilon_\beta \mid^2 . \tag{2.24}$$

In a more descriptive picture, since small units of q correspond to large scales $\lambda^* \sim q^{-1}$ contributing to the scattering, only the long-range collective motion of groups of electrons (electron density waves) are probed, and motions between individual electrons do not contribute to the signal. Likewise, for large values of q, only the very small length scales corresponding to distances between individual electrons make a difference in scattering strength, and whatever is happening on larger scales is not contributing.

Experimentally, in the context of hard x-rays of $5-15$ keV and solids, collective scattering (small q) occurs in the forward direction at scattering angles of a few 10s of degrees, while in back-scattering (close to 180° scattering angle) non-collective scattering occurs. In between these two cases, the regimes transition into each other and the process cannot be described cleanly be the one or the other model alone.

2.2.2 Inelastic x-ray scattering from phonons

At low energy transfers, vibrational modes of the lattice become a domineering contribution to the structure factor. With the adiabatic approximation [75], where the electron density instantaneously follows ionic motions, the electron density ρ of a crystal can be written as

$$\rho(\vec{q}) = \sum_l e^{-i\vec{q}\cdot\vec{R}_l}\left(\sum_{i(l)} e^{-i\vec{q}\cdot(\vec{r}_i-\vec{R}_l)}\right) = Zf(\vec{q})\sum_l e^{-i\vec{q}\cdot\vec{R}_l}, \tag{2.25}$$

where the first part sums over all l atoms in the lattice and the second sum goes over all electrons of the lth-atom at position $\vec{R}_l$, Z the number of electrons and $f(\vec{q})$ the atomic form factor, defined as the Fourier transform of the atomic charge distribution $\rho(\vec{r})$

$$f(\vec{q}) = \int \rho(\vec{r}) e^{i\vec{q}\cdot\vec{r}} d\vec{r}. \tag{2.26}$$

Under the assumption of a simple lattice containing only one species of atoms and a single atom per unit cell, the one-phonon structure factor [69] becomes

$$\begin{aligned} S(\vec{q},\omega) = \frac{Z}{\hbar} f^2(\vec{q}) e^{-2W} \frac{V}{(2\pi)^3} \left[\sum_{\vec{G}} \delta(\vec{q}-\vec{G})\right] \delta(\omega) + Z^2 f^2(\vec{q}) e^{-2W} \frac{V}{(2\pi)^3} \\ \times \sum_{\vec{q}_0 \vec{j}} \frac{1}{2m\omega_{\vec{q}_0\vec{j}}} \mid \vec{q}\cdot\vec{e}(\vec{q}_0\vec{j}) \mid^2 \{\langle n_{\vec{q}_0\vec{j}}\rangle \delta(\omega+\omega_{\vec{q}_0\vec{j}}) + \langle n_{\vec{q}_0\vec{j}}+1\rangle \delta(\omega-\omega_{\vec{q}_0\vec{j}})\} \\ \times \sum_{\vec{G}} \delta(\vec{q}\pm\vec{q}_0-\vec{G}). \end{aligned} \tag{2.27}$$

Here, the first term gives the purely elastic scattering with the unit cell volume V and the Debye-Waller factor $e^{-2W} = e^{-\langle(\vec{q}\cdot\vec{u}_l(t))^2\rangle}$, which gives the average displacement $\vec{u}_l(t)$ of the atoms. The second term gives the inelastic contribution from one phonon, which can either be created or annihilated. $\vec{e}(\vec{q}_0\vec{j})$ is the eigenvector of the phonon, $\vec{q}_0$ its momentum, $\vec{j}$ the polarization branch, and $\omega_{\vec{q}_0\vec{j}}$ the corresponding angular frequency. $\langle n_{\vec{q}_0\vec{j}}\rangle$ is the Bose-Einstein occupation factor and is given by

$$\langle n_{\vec{q}_0\vec{j}}\rangle = \frac{1}{e^{\hbar\omega_{\vec{q}_0\vec{j}}\beta}-1}, \;\; \beta = \frac{1}{k_B T}, \tag{2.28}$$

where k_B is the Boltzmann constant and T the temperature.

2.2.3 Temperature from detailed balance

From the last obtained result (Eq. 2.27) it can be seen that the inelastic scattering response from phonons is directly dependant on the Bose-Einstein occupation factor and therefore the temperature. A model independent measurement of the temperature can be performed by comparing the intensities of the Stokes (energy loss) and anti-Stokes (energy gain) lines in the spectrum of the scattered photons (Fig. 2.29):

$$\frac{I(-\omega)}{I(\omega)} = \frac{\langle n_{\vec{q}_0\vec{j}}+1\rangle}{\langle n_{\vec{q}_0\vec{j}}\rangle} = \frac{-\langle n(-\omega)\rangle}{\langle n(\omega)\rangle} = e^{\frac{\hbar\omega}{k_B T}}. \tag{2.29}$$

As the scattered off phonons are a collective motion of particles, it poses the criteria to be in the coherent scattering regime to detect this signal. For typical x-ray energies in the keV-range, this implies a forward scattering geometry with low momentum transfers. In addition to the temperature measurement, for some systems a highly resolved spectrum (showing the position and width of the spectrally resolved features) allows the determination of more material properties like the speed of sound from $c_s = \omega/q$ from the phonon separation from the quasi-elastic line and the thermal diffusivity $D_T = FWHM/2q^2$ from the width of the quasi-elastic line.

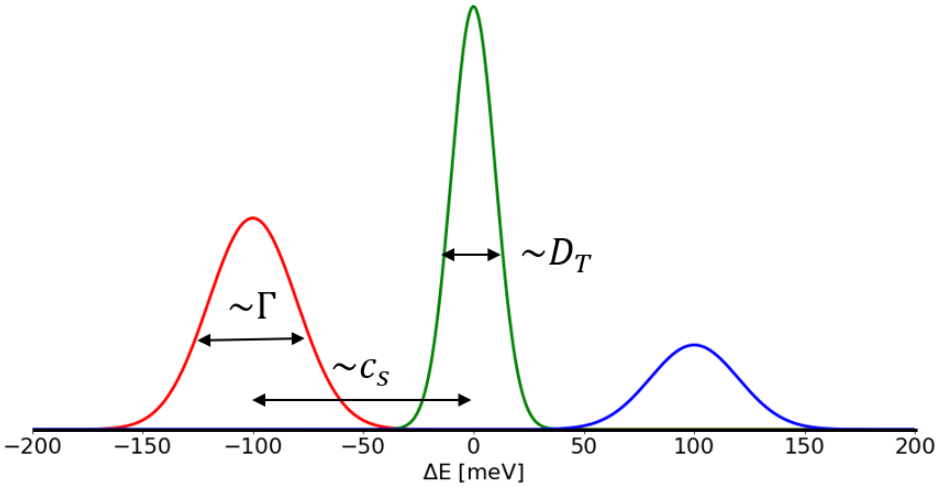

Figure 2.4: Simplified response from inelastic phonon scattering. The scattering spectrum consists of the quasi-elastic line (green) at zero energy transfer and two lines symmetric around it corresponding to phonon creation (red, Stokes) and annihilation (blue, anti-Stokes). The temperature can be determined via detailed balance from the intensity ratio of Stokes and anti-Stokes lines. Measuring this spectrum can also yield additional information about simple systems like the speed of sound c_s, thermal diffusivity D_T, and sound attenuation coefficient Γ.

2.2.4 Temperature from non-collective scattering

The light emitted by a moving particle is either shifted to lower or higher frequencies for an observer, depending on the direction of movement. A higher frequency is observed when moving towards the observer, a lower frequency when moving away. This modified frequency f is given by the Doppler shift [76]

$$f = f_0 \left(1 + \frac{v}{c}\right), \tag{2.30}$$

where v is the relative velocity of the particle to the observer and c the speed of light. The velocities are on the order of the speed of sound inside the material, meaning km/s in most solids. Therefore, it is not necessary to use relativistic formalism. Looking at an ensemble of particles emitting monochromatic light in thermal movement, the observed light will be broadened by higher and lower frequencies due to the random distribution of movement directions.

At high temperatures, as they exist after laser excitation of a solid, the atoms within the material can be assumed to follow the Maxwell-Boltzmann velocity distribution [77–79], as long as we deal only with one species of atoms and the laser energy is low enough to neglect relativistic effects

$$f(v)d^3v = \left(\frac{m}{2\pi k_B T}\right)^{\frac{3}{2}} e^{-\frac{mv^2}{2k_B T}} d^3v, \tag{2.31}$$

where m is the particle mass, temperature $T[K]$, the Boltzmann constant k_B, and velocity v. Rearranging Eq. 2.30 for v and inserting it into the velocity distribution yields a Gaussian profile with a FWHM value Δf of

$$\Delta f = \sqrt{\frac{8 k_B T ln2}{mc^2}} f_0. \tag{2.32}$$

As the particles are not emitting the x-rays but scattering them, the Doppler shift applies twice. The measured temperature in eV is therefore given by

$$T[eV] = \frac{1}{4} \frac{mc^2}{8 ln2} \left(\frac{\Delta E}{E_0} \right)^2, \tag{2.33}$$

where ΔE is the change to the nominal photon energy E_0. In contrast to the phonon measurement, the signal here originates from individual atoms moving independently from each other. Thus, it is necessary to measure in the non-collective regime. For kev-range x-rays, this implies a backscattering geometry at high momentum transfers.

2.3 Instrumentation

2.3.1 X-ray free-electron laser

Because of their short wavelength and deep penetration into high density matter, x-rays are a very good tool for diagnosing solid-density targets. There exist a variety of sources for x-ray radiation, all of them imprinting their own characteristics onto the generated x-rays. Due to the ultra-fast timescales of the plasma processes investigated in the scope of this work, only sources generating x-rays of a similar short duration make for a good diagnostic tool. Therefore, all experiments were conducted at an XFEL. Here, a short introduction to the working principles of an XFEL will be given, as well as an overview of the radiation properties generated by the self-amplification of spontaneous emission process (SASE, [80] and hard x-ray self-seeding (HXRSS, [81]). A more detailed introduction to FEL theory is given by Saldin *et al.* [82] or Freund & Antonsen [83], while an introduction to the more technical aspects can be found e.g. in Jaeschke *et al.* [84] and Schmüser *et al.* [85].

Principles of XFELs

In a FEL, radiation is generated by free electrons, which travel in vacuum while passing through a periodic sequence of magnets, called an undulator (Fig. 2.5). Assume, the individual magnets all posses the same size and strength and are perfectly parallel to the electron beam axis with a periodicity of λ_u. The vertical magnetic field at the centre between the magnets is then given by

$$\vec{B} = -B_0 \sin(k_u z)\vec{e}_y, \tag{2.34}$$

where $k_u = \frac{2\pi}{\lambda_u}$, z the position along the longitudinal axis of the undulator, and $\vec{e}_y$ is a unit vector in vertical direction. Passing through this field, electrons go into a transverse motion in a plane parallel to the magnets due to the Lorentz force. This can be described by two coupled differential equations

$$\frac{\partial^2}{\partial t^2}x = \frac{e}{\gamma m_e} B_y \frac{\partial}{\partial t} z, \qquad \frac{\partial^2}{\partial t^2}z = -\frac{e}{\gamma m_e} B_y \frac{\partial}{\partial t} x. \tag{2.35}$$

Here, e is the electron charge and m_e the electron mass. γ is the Lorentz factor

$$\gamma = \frac{1}{\sqrt{1-\frac{v^2}{c^2}}} = \frac{1}{\sqrt{1-\beta^2}} \tag{2.36}$$

where v is the velocity and c the speed of light. In first approximation, $\frac{\partial}{\partial t} z$ can be assumed to be constant due to the electrons very high initial velocity along the longitudinal axis z, which is also much larger than the

velocity along the deflection axis. With the initial conditions $x(0) = 0$ and $\frac{\partial}{\partial t}x = \frac{eB_0}{\gamma m_e k_u}$, the resulting trajectory for an electron in the undulator field becomes

$$x(z) = \frac{K}{\beta\gamma k_u} \sin k_u z. \tag{2.37}$$

K is called the undulator parameter, which is defined as

$$K = \frac{eB_0\lambda_u}{2\pi m_e c}. \tag{2.38}$$

If the reduction of the longitudinal velocity is included, the equations of motions are

$$x(t) = \frac{K}{\gamma k_u} \sin \omega_u t, \qquad z(t) = \bar{v}_z t - \frac{K^2}{8\gamma^2 k_u} \sin 2\omega_u t, \tag{2.39}$$

with $\omega_u = \bar{\beta} c k_u$ being the undulator frequency and $\bar{v} = c(1 - \frac{2+K^2}{4\gamma^2})$ the average velocity. In the reference frame of an electron moving along the longitudinal axis of the undulator, the electron performs an oscillation along the transverse axis. Due to this oscillatory motion, an electron passing through the undulator emits an electromagnetic wave, whose power is given by the Larmor formula [74, 86]

$$P = \frac{e^2}{6\pi\varepsilon_0 c^3} \left(\frac{\partial}{\partial t} v\right)^2, \tag{2.40}$$

where ε_0 is the vacuum permittivity. With the equation of motion (Eq. 2.39) and neglecting the longitudinal oscillation, this results in the total radiation power in the first harmonic from a single electron in the reference frame of the moving electron

$$P_{tot} = \frac{e^2 c \gamma^2 K^2 k_u^2}{12\pi\varepsilon_0 \left(1 + \frac{K^2}{2}\right)^2}. \tag{2.41}$$

As the power is invariant under Lorentz transformation, this is equal to the radiation power in the rest frame. The electrons basically behave like an oscillating electric dipole moving at relativistic speed. Therefore, in the laboratory frame, the emitted light is concentrated into a narrow cone. Transformed into the laboratory frame, the radiation wavelength as a function of the emission angle θ with respect to the undulator axis arriving is given by

$$\lambda_{lab}(\theta) = \frac{\lambda_u}{2\gamma^2} \left(1 + \frac{K^2}{2} + \gamma^2\theta^2\right). \tag{2.42}$$

This is the wavelength emitted by every undulator at 3rd generation light sources. To reach higher peak brightness, all electrons within a bunch would ideally emit coherently in phase so the intensity scales with the number of electrons squared, $I = N^2 I_{single}$. With around 10^9 electrons per bunch, this composes a significant increase in intensity.

Unfortunately, it is practically impossible to confine this many electrons within the span of an x-ray wavelength to emit as a single entity. Also, as an optical resonator for x-rays has not yet been realised [87], XFELs operate in a single-pass amplifier mode, meaning the pulse passes the amplifier just once. These so-called high-gain FELs solve this problem through the process of microbunching.

During the microbunching process, the generated radiation interacts back with the electrons. Electrons gain or lose energy depending on their position in respect to the light wave. This results in a modification of their oscillation trajectory and through this a change to the longitudinal velocity $\bar{v}_z$. Through increasing feedback, the electrons will be concentrated in thin slices shorter than the form giving wavelength. Electrons in each of these slices emit light like one single particle, leading to an even stronger radiation field modulating the micro bunching (Fig. 2.5).

For a sustainable energy transfer within the undulator, the time difference between light wave and electrons in half an undulator period needs to satisfy the condition

$$c\Delta t = \lambda/2, \;\; \Delta t = \left(\frac{1}{\bar{v}_z} - \frac{1}{c}\right)\frac{\lambda_u}{2}. \tag{2.43}$$

The wavelength fulfilling this condition is in good approximation the same as the one for spontaneous undulator radiation (Eq. 2.42). Therefore, this radiation can serve as a seed for FEL amplification, together with its odd higher harmonics. For even harmonics, there is no sustained energy transfer.

Radiation properties

For XFELs, no (frequency-multiplied) optical lasers are available to seed the amplifications process with sub-nm wavelengths. Though, it is possible to amplify the spontaneous undulator radiation, as seen in the previous section (see 2.3.1). This method is called self-amplification of spontaneous emission (SASE) [80, 88]. It has the disadvantage, that every amplification process starts from noise. Within a single pass through the undulator, multiple modes that fit the FEL bandwidth will be amplified and no light pulse will look exactly like any other. X-ray pulses produced by the SASE process typically have a bandwidth of 20-40 eV in the keV photon energy range.

In the same manner as the spectral composition, the total pulse energy and relative intensities of singular modes underlies stochastic fluctuations. A SASE-FEL can produce powerful pulses in the low-keV regime. Average pulse energies of 3 mJ at 8 keV, corresponding to 2.3×10^{12} photons per pulse, have been demonstrated.

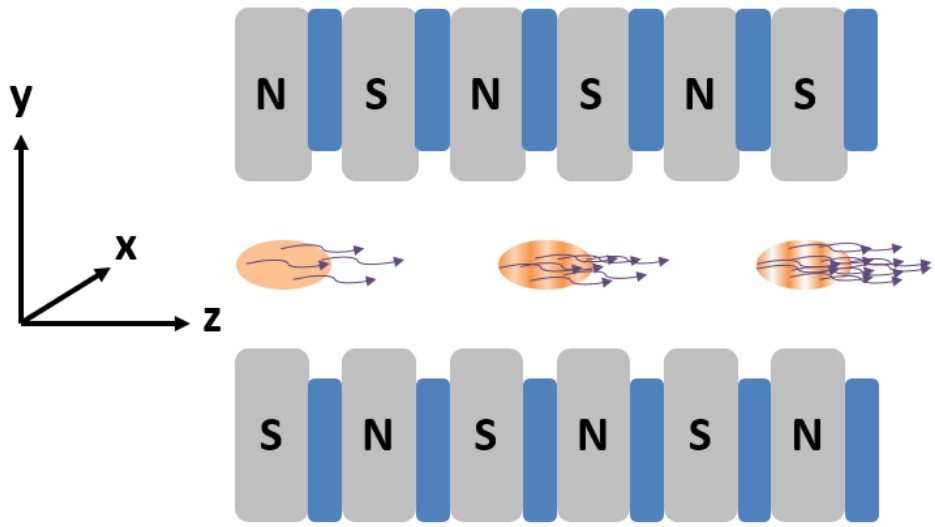

Figure 2.5: SASE process in an undulator. An electron bunch passes through the undulator from left to right. In the beginning, only spontaneous radiation is emitted from the randomly distributed electron cloud. As the passage progresses, the electrons are influenced by the radiation and microbunching starts to emerge. In saturation the complete electron bunch possesses a microbunched structure where each slice emits in phase. The radiation field grows exponentially.

The pulse duration of the x-rays is determined by the fraction of the electron bunch contributing to the lasing. Pulse durations in the range 10-50 fs are typical, durations below 1 fs could be measured [89].

The dominant mode of an FEL pulse after the undulator is usually the Gaussian TEM_{00} mode, as it has the best overlap with the electron bunch and therefore undergoes the highest amplification. Consequently, the pulses exhibit a high degree of transversal coherence. In contrast, there is no temporal coherence over the duration of the SASE pulse due to the presence of multiple amplified modes.

As many applications, like the high-resolution IXS techniques discussed above, require higher spectral resolution, monochromators are necessary to reduce the bandwidth of SASE pulses. Unfortunately, this greatly reduces the number of photons available at the experiment, so solutions have been found to increase the spectral density of the photons in a smaller bandwidth.

One already implemented method at operating XFELs is self-seeding [81,90]. For hard x-ray self-seeding (HXRSS), the undulator section needs to be split in two. In the first section, an x-ray pulse is generated through the normal SASE process. Then, the x-ray pulse is send through a monochromator that cuts out the part of the spectrum containing the desired photon energy. Meanwhile, the electron bunch gets diverted by a magnetic chicane. This first has the effect of protecting the monochromator from the GeV electron beam and second that it gives a variable delay to the electrons compared to the x-ray pulse while destroying any present microbunching. The light pulse passes through the monochromator, now showing an almost rectangular cut-out in the spectrum around

the requested photon energy. This modified pulse is followed by a temporal beating at the missing photon energy. The delayed electrons are overlapped with the beating, which now serves as a seed in the second undulator section.

The so obtained x-ray pulses usually posses only one, sometimes two, modes that get amplified with a resulting bandwidth on the order of 1 eV with a small SASE background. HXRSS pulses are usually weaker than SASE pulses due to the smaller available amplification length in the undulator. Nevertheless, the amount of photons at the requested photon energy is higher in the single seeded mode than in all but the brightest SASE pulses from the same undulator. Therefore, HXRSS is a good tool for experiments which require a narrow bandwidth, as it produces on average a higher spectral brightness than SASE. The weak SASE background can be cleaned with a monochromator which transmits a similar bandwidth to the seeded mode.

2.3.2 X-ray optics

All the experiments presented here in the scope of this work require an XFEL and specific set of x-ray optics to work properly. This optics set includes monochromators [2.3.2] to control the x-ray bandwidth, focusing optics [2.3.2] for controlling the x-ray beam size, x-ray analysers [2.3.2] to characterize the x-ray radiation after the target interaction and lastly, x-ray detectors [2.3.2] for collecting the gained information. In this section, the general working principles of these devices will be briefly explained. The explicit details of the used setups will be discussed later in the experiment chapter 4.

Monochromators

The x-ray pulses generated by the SASE process [80] in the undulators typically have an energy bandwidth $\Delta E/E \approx 10^{-3}$ [91], which is much wider than the intended meV resolution for photon energies in the keV range. Thus, for techniques requiring eV or below energy resolution, it becomes necessary to reduce the incident bandwidth. In the hard x-ray regime, crystal monochromators are mainly used for this purpose. These crystals work by Bragg reflecting a selection of photon energies out of an incoming beam. To preserve the low divergence and coherence properties of an FEL beam and also to deal with the high incident heat load, large perfect crystals are required for this purpose. For large perfect crystals, the weak scattering approximation of the kinematical scattering theory [92] fails, as multiple-scattering events can no longer be neglected. Instead, the so called dynamical diffraction theory [92–94] is used to describe the interaction. A detailed discussion can be found e.g. in the text books by Als-Nielsen & McMorrow [95], Authier [96], or, for the special case of high energy resolution, Shvyd'ko [97]. A brief introduction to the case of symmetric Bragg reflection, where the surface is parallel to the lattice planes, based on the approach by Ewald [93] be given here.

Dynamical diffraction theory. In the kinematical theory of diffraction, the amplitude of the scattered radiation is build up from the scattering of a single electron, an atom, the crystal unit cell and the crystal lattice. This all happens under the assumption, that the intensity of the x-rays is uniform over the depth of the crystal. The dynamical theory takes into account, that at each lattice plane a fraction of the intensity is refracted into the exiting wave and that there is a chance for multiple scattering events, where the x-rays are reflected in the direction of the incoming wave within the crystal. It then enables the calculation of the reflected intensity as a function of incident photon energy, angle, polarization, etc.

Consider a plane, linearly polarized electromagnetic wave

$$\vec{\varepsilon}(\vec{r},t) = \vec{\varepsilon_{ini}} \exp[i(\vec{K}_0 \cdot \vec{r} - \omega t)] \tag{2.44}$$

where $|\vec{K}_0| = \frac{2\pi}{\lambda} = \frac{E}{\hbar\omega}$ is the wave vector in vacuum and $\omega = \frac{E}{\hbar}$ the radiation frequency. The spatial electric field $\vec{\mathscr{D}}(\vec{r})$ excited by this wave within the crystal is obtained by assuming the crystal to be a medium with a periodic dielectric constant and solving Maxwell's equations for it

$$[-\nabla^2 - K^2]\,\vec{\mathscr{D}}(\vec{r}) = K^2\,\chi(\vec{r})\vec{\mathscr{D}}(\vec{r}). \tag{2.45}$$

The crystal susceptibility $\chi(\vec{r})$ can be expressed as a series over the reciprocal lattice vectors $\vec{G}$ as

$$\chi(\vec{r}) = \sum_G \chi_G \exp(i\vec{G}\cdot\vec{r}), \tag{2.46}$$

where the individual components χ_G are given by

$$\chi_G = -\frac{r_e F_G}{\pi V}\lambda^2 \tag{2.47}$$

with the classical electron radius r_e, unit cell volume V, and unit cell structure factor F_G. The structure factor of the crystal unit cell is given by

$$F_G = \sum_n f_n(\vec{G}) e^{i\vec{G}\cdot\vec{r}_n - W_n(\vec{G})}, \tag{2.48}$$

where $f_n(\vec{G}$ are the atomic form factors and $W_n(\vec{G})$ the Debye-Waller factors. The reciprocal lattice vector $\vec{G}$ is formed from a set of base vectors of the crystal lattice

$$\vec{G} = h\vec{b_1} + k\vec{b_2} + l\vec{b_3}. \tag{2.49}$$

The integer number h, k, and l are called Miller indices [98] and denote a set of lattice plane normal to $\vec{G}$ with interplanar spacing

$$d_G = \frac{2\pi}{\mid \vec{G} \mid}. \tag{2.50}$$

The solution to Maxwell's equation (Eq.2.45) under these periodic conditions are Bloch waves [75] of the form

$$\vec{\mathscr{D}}(\vec{r}) = \sum_G \vec{D_G}\ e^{i\vec{k_G}\vec{r}},\ \vec{k_G} = \vec{k_0} + \vec{G}. \tag{2.51}$$

Inserting this solution (Eq.2.51) into the wave equation (Eq.2.45) yields the fundamental equations of the dynamical diffraction theory, a system of linear equations for the plane wave components:

$$\vec{D_G} \ = \ \frac{K^2}{\vec{k_G}^{\,2} - K^2(1+\chi_0)} \sum_{G' \neq G} \chi_{G-G'}\, \vec{D_{G'}}. \tag{2.52}$$

Their solutions gives the radiation field inside the crystal. Because the $\chi_{G-G'}$ coefficients are small, the only significant contributions to D_G are when the pre-factor is also small, leading to the so-called excitation condition

$$k_G \approx K \mid 1 + \frac{\chi_0}{2} \mid, \tag{2.53}$$

meaning only wave vectors of this magnitude are excited. As the condition from (Eq 2.51) also needs to be fulfilled, possible wave vectors are restricted to those, where the momentum transfer from $\vec{k_0}$ is equal to a reciprocal lattice vector $\vec{G}$. Momentum- and energy conservation post requirements for the vacuum-crystal interface, which leads to an adjustment to the outgoing in-vacuum wave vector

$$\vec{K_G} = \vec{K_0} + \vec{G} + \Delta_G \vec{e}_z, \quad \Delta_G = \xi - \xi_G, \tag{2.54}$$

where ξ, ξ_G are wave vector corrections due to the vacuum-crystal interface applied along the inward pointing surface normal unit vector $\vec{e}_z$. The additional momentum transfer Δ_G can be rewritten as

$$\Delta_G = K(-\gamma_G \pm \sqrt{\gamma_G^2 - \alpha_G}), \tag{2.55}$$

with the parameters as follows

$$\gamma_0 = \frac{\vec{K_0}\vec{e}_z}{k}, \tag{2.56}$$

$$\gamma_G = \frac{(\vec{K}_0 + \vec{G})\vec{e}_z}{K}, \tag{2.57}$$

$$\alpha_G = \frac{2\vec{K}_0\vec{G} + \vec{G}^2}{K^2}. \tag{2.58}$$

A useful step is the redefinition of these parameters in terms of angles:

$$\gamma_0 = \cos\theta_G \sin\eta_G \cos\phi_G + \sin\theta_G \cos\eta_G, \tag{2.59}$$

$$\gamma_G = \cos\theta_G \sin\eta_G \cos\phi_G + \sin\theta_G \cos\eta_G - \alpha_G \frac{K}{G} \cos\eta_G, \tag{2.60}$$

$$\alpha_G = \frac{G}{K}(\frac{G}{K} - 2\sin\theta_G). \tag{2.61}$$

These parameters are defined by the angles of the incoming beam, where θ_G is the glancing angle, the angle between $\vec{K}_0$ and and the reflecting plane. It can take values between 0 and $\frac{\pi}{2}$. ϕ_G is the azimuthal angle of incidence, the angle between the $(\vec{K}_0, \vec{G})$ plane and the lattice plane, and take values from 0 to 2π. η_G is the asymmetry angle of the crystal, the angle between the surface normal and the reflection planes. The combination of these parameters gives the asymmetry parameter

$$b_G = \frac{\gamma_0}{\gamma_G}. \tag{2.62}$$

This parameter indicates how far off the symmetric case regarding the surface normal incoming and outgoing wave vectors are. In the case of symmetric Bragg reflections, it holds to very good approximation that $b_G = -1$.

To solve the system of equations, the electric field can be separated in two orthogonal linearly polarized components normal to $\vec{k}_G$, usually called π and σ

$$\vec{D}_G = D_G^{\pi}\vec{\pi} + D_G^{\sigma}\vec{\sigma}, \tag{2.63}$$

where

$$\vec{\sigma}_G = \frac{\vec{k}_G \times \vec{k}_0}{|\,\vec{k}_G \times \vec{k}_0\,|}, \qquad \vec{\pi}_G = \frac{\vec{k}_G \times \vec{\sigma}_0}{|\,\vec{k}_G\,|}. \tag{2.64}$$

After the polarization separation, the fundamental equations (Eq. 2.52) can be rewritten as

$$\sum_{G',s'} J_{GG'}^{ss'} D_{G'}^{s'} - (2\gamma_G \frac{\xi}{K} + \frac{\xi^2}{K^2}) D_G^s = 0, \tag{2.65}$$

$$J_{GG'}^{ss'} = \chi_{G-G'} P_{GG'}^{ss'} - \alpha_G \delta_{GG'}^{ss'}, \tag{2.66}$$

$$P_{GG'}^{ss'} = (\vec{s}_G \vec{s}'_G). \tag{2.67}$$

Here, s indicates the two polarization directions, $J_{GG'}^{ss'}$ is the scattering matrix of rank 2n with the polarization factor $P_{GG'}^{ss'}$ and Kronecker delta δ. Due to the small size of ξ, the quadratic term can be neglected in most cases; they only play a role for tiny grazing incidence angles. Then, the system of equations in ξ (Eq. 2.65) forms 2n equation for the plane wave components D_G^s. The non-trivial solution for the total filed inside the crystal is given by the sum over the wave fields $\vec{\mathscr{D}}_\nu(\vec{r})$ for each eigenvector

$$\vec{\mathscr{D}}(\vec{r}) = \sum_G e^{i(\vec{K}_0+\vec{G})\cdot\vec{r}} \vec{D}_G(z), \tag{2.68}$$

$$\vec{D}_G(z) = \sum_\nu \Lambda_\nu \vec{D}_{G(\nu)} e^{i\xi_\nu z}. \tag{2.69}$$

The Λ_ν coefficients may be obtained from the boundary conditions of the field inside the crystal. From (Eq. 2.44) it is clear, that the initial field entering the crystal is $\vec{D}_0(z_{front}) = \vec{\varepsilon}_{ini}$. In the Bragg geometry, the radiation is reflected out of the crystal through the front surface and there is no wave exiting the back side of the crystal, leading to the secondary boundary condition $\vec{D}_G(z_{rear}) = 0$.

The electric fields are usually not measured in an experiment. Instead, the reflectivity of a crystal is the typically used parameter. It is the ratio of the radiation fluxes between the incoming and outgoing beams. The flux density given by the Poynting vector can be obtained from the wave field, as $\mid D_G \mid^2$ is proportional to the Poynting vector for plane waves. In case of asymmetric reflections, the size of incoming and outgoing beam changes by the asymmetry factor b_G. This results in the reflectivity R of the crystal in Bragg reflection

$$R = \frac{1}{\mid b_G \mid} \frac{\mid \vec{D}_G(z_{front}) \mid^2}{\mid \vec{\varepsilon_{ini}} \mid^2}. \tag{2.70}$$

Multiple reflections can get complicated to calculate quickly due to the number of equations involved. In the following, the simple case of two-beam diffraction shall be used to derive some relevant results for

the high-resolution applications. Two-beams in this case means that the incoming x-rays excite two response waves inside the crystal, one transmitted further into the crystal and one getting Bragg-reflected. The system of fundamental equations (Eq. 2.65) then consists of four equations, two for each polarization. The polarization factor P becomes $P = 1$ for the σ-component and $P = \cos 2\theta$ for the π-component. As the general expression for the reflectivity takes a complicated form, it makes sense to look at the case relevant for the monochromators used within the scope of this work. One assumption is thick crystals, meaning that the penetration depth of the x-rays l_e is much smaller than the crystal thickness l. Next, photo-absorption shall be neglected. Also, none of the monochromators used in this work operate at particularly shallow incident angles, so the quadratic ξ-term can also be neglected. The penetration length is then given by

$$l_e(y) = l_e(0)\Im\left(\frac{1}{\sqrt{y^2-1}}\right) \tag{2.71}$$

with the extinction length $l_e(0)$

$$l_e(0) = \frac{\sqrt{\gamma_0 \mid \gamma_G \mid}}{K \mid P\chi_G \mid} \tag{2.72}$$

and the reduced deviation parameter y

$$y = \frac{\alpha b + \chi_0(1-b)}{2 \mid P\chi_G \mid \sqrt{\mid b \mid}}. \tag{2.73}$$

The reflectivity of this thick crystal with no absorption is given by

$$R = \left| -y \pm \sqrt{y^2-1} \right|^2. \tag{2.74}$$

It is a function of only the reduced deviation parameter (Eq. 2.73) and shows a region of total reflection for $-1 \leq y \leq 1$. When photo-absorption is included in the calculations, this region is no longer total reflective.

To make the theory easily applicable, the deviation parameter α (Eq. 2.61) can be rewritten in respect to real physical parameters [99]:

$$\alpha = \frac{2\lambda}{d_G(T)}\left[\frac{\lambda}{2d_G(T)} - \sin\theta\right], \tag{2.75}$$

$$\alpha = 4\frac{E_G(t)}{E}\left[\frac{E_{G(T)}}{E} - \sin\theta\right], \tag{2.76}$$

where $E_G = \frac{hc}{2d_G}$ is the Bragg energy. These expressions take also into account, that the distance d_G between the atomic planes is dependent on the temperature T. The width of the region of total reflection in terms of α is given by

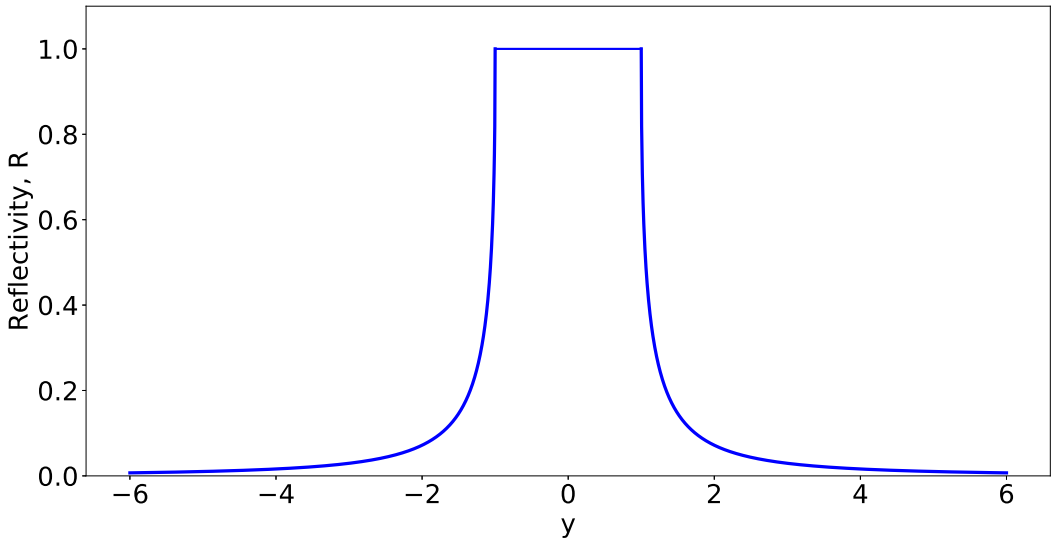

Figure 2.6: The reflectivity R of a thick crystal in Bragg geometry with no absorption as a function of the reduced deviation parameter y. Note the region of total reflection.

$$\Delta\alpha = 4\,\frac{|\,P\,|}{\sqrt{|\,b\,|}}, \tag{2.77}$$

witch the centre α_c at

$$\alpha_c = \chi_0'\,(1-\frac{1}{b}), \tag{2.78}$$

with χ_0' being the real part of the crystal susceptibility. The size of the width is typically on the order $\sim 10^{-6}$. So small changes in photon energy or crystal temperature can lead to drastic changes in reflectivity. α can also be rewritten in terms of the incidence angle θ and the angle θ_B as defined by Bragg's law $\lambda = 2\,d_G\,\sin\theta_B$

$$\alpha = 4\sin\theta_B\,[\sin\theta_B - \sin\theta]\,, \tag{2.79}$$

or, for small deviations $|\,\theta_B - \theta\,| \ll 1$,

$$\alpha = 2(\theta_B - \theta)\sin 2\theta_B. \tag{2.80}$$

For x-rays with wavelength λ at an incidence angle $\theta = \theta_B$, the deviation parameter is $\alpha = 0$. This only coincides with the centre of the total reflection region in the kinematic approximation, where multi-scattering

events and refraction at the crystal-vacuum boundary are neglected. According to (Eq. 2.46), α_c can be rewritten in terms of wavelength

$$\alpha_c = -2w_G^{(s)} \left(\frac{\lambda_c}{2d_G}\right)^2 \left(1 - \frac{1}{b}\right), \qquad w_G^{(s)} = -2\chi_0' \frac{d_G^2}{\lambda^2}, \tag{2.81}$$

with the asymmetry factor b becoming

$$b = \frac{\cos\theta_c \sin\eta \cos\phi_c + \sin\theta_c \cos\eta}{\cos\theta_c \sin\eta \cos\phi_c - \sin\theta_c \cos\eta}. \tag{2.82}$$

This gives in combination with (Eq. 2.75) a modified version of Bragg's law

$$2\,d_G \sin\theta_c = \lambda_c(1 + w_G), \qquad w_G = w_G^{(s)} \frac{b-1}{2b}, \tag{2.83}$$

$w_G^{(s)}$ being the symmetric scattering case defined in (Eq. 2.81, $b = -1$). In Bragg scattering geometry, the correction w_G is always positive, shifting the centre of the total reflection region to higher angles θ_c (higher photon energies E_c) than Bragg's law. Above it was shown, that total reflection does not only occur at a singular point, but in a region. From (Eq. 2.46, 2.73, 2.75) it is possible to obtain the wavelength borders of the region of total reflection at incidence angle θ_c

$$2d_G \sin\theta_c = \lambda_\pm(1 + w_G \pm \frac{\varepsilon_G}{2}), \quad \varepsilon_G = \frac{\varepsilon_G^{(s)}}{\sqrt{\mid b \mid}}, \quad \varepsilon_G^{(s)} = \frac{4 r_e d_G^2}{\pi V} \mid P F_G \mid, \tag{2.84}$$

with the total reflection regions width $\varepsilon_G = \frac{\lambda_- - \lambda_+}{\lambda} = \frac{\Delta\lambda}{\lambda} = \frac{\Delta E}{E}$, which is the relative spectral width of the reflection. $\varepsilon_G = \varepsilon_G^{(s)}$ for the symmetric reflection. The relative spectral width is almost constant over a wide spectral range, only the anomalous scattering corrections f' in F_G are photon-energy dependent (Fig. 2.7). These changes are very small, e.g. only permille over half a keV in silicon 14.4 keV [100]. For the most part, the central wavelength of the region of total reflection changes nearly linearly, which changes when the angles approaches 90°, where it can be modeled with a quadratic dependence

$$\lambda_c = \frac{2d_G}{1 + w_G^{(s)}} \left(1 - \frac{1}{2}\left(\frac{\pi}{2} - \theta\right)^2\right). \tag{2.85}$$

Due to this quadratic behaviour, the photon energy undergoes only very small changes for variations in the incidence angle when approaching backscattering geometries. With (Eq.2.48), the relative spectral width $\frac{\Delta\lambda}{\lambda} = \varepsilon_G^{(s)}$ reads in first approximation

$$\frac{\Delta\lambda}{\lambda} = \frac{4 \mid P \mid r_e d_G^2}{\pi V} \left| \sum_n f_n^{(0)}(\vec{G}) \exp\left(i\vec{G}\cdot\vec{r}_n - 2\pi^2 \frac{\langle v_G^2 \rangle}{d_G^2}\right)\right|. \tag{2.86}$$

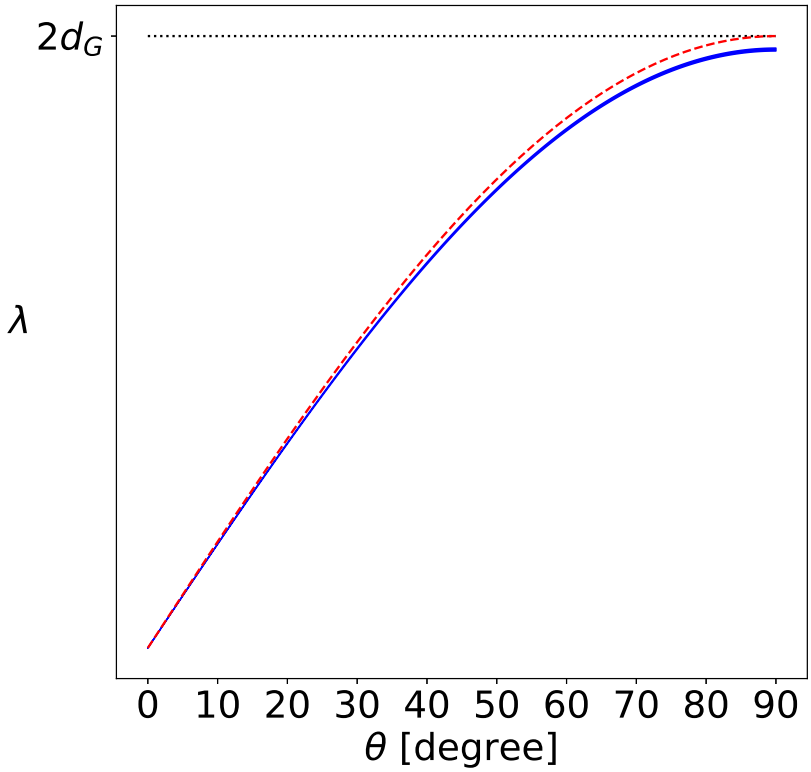

Figure 2.7: General behaviour of a symmetric Bragg reflection in (λ, θ)-space. The red dashed line shows the trend according to the kinematic Bragg law, ending at a wavelength of twice the lattice constant at 90° incidence angle. The solid blue line shows the same behaviour for the modified Bragg law, reaching a maximum wavelength of $(2d_G) / \left(1 + w_G^{(s)}\right)$. The area of the line represents the relative spectral width $\frac{\Delta\lambda}{\lambda}$, which is constant over the region.

It becomes apparent again, that the relative spectral width is independent of incident angle and photon energy. It does however depend on the crystal, in the form of the interplanar distance and scattering vector, atomic properties with the atomic form factor (Eq. 2.26), and the temperature in the form of the Debye-Waller factor. Thus, $\frac{\Delta E}{E}$ gets narrower, if the interplanar distance gets smaller or the Bragg energy $E_G = \frac{hc}{2d_G}$ gets larger. As it was shown that the relative spectral width is almost constant over the (λ, θ)-space, this means that in terms of absolute values the narrowest bandwidth is achieved for the low photon energies near 90° incidence. As an example, some values for the silicon monochromators used in this work are shown in table 2.1.

hkl	E (keV)	$\Delta\theta(\mu rad)$	$\Delta\theta/\theta$	ΔE(meV)	ΔE/E
	3	117.44	1.6×10^{-4}	402	1.3×10^{-4}
111	7.494	36.318	1.4×10^{-4}	995	1.3×10^{-4}
	10.896	24.295	1.3×10^{-4}	1435	1.3×10^{-4}
	3	-	-	-	-
533	7.494	83.227	5.5×10^{-6}	30	4.0×10^{-6}
	10.896	3.76	5.0×10^{-6}	43	4.0×10^{-6}
	3	-	-	-	-
931	7.494	-	-	-	-
	10.896	27.264	1.8×10^{-5}	10	9.8×10^{-7}

Table 2.1: Overview of Bragg reflections (and their higher orders) of monochromators at the three major photon energies used in this thesis. All reflections are calculated for the σ-polarization in silicon crystals. Calculations were done using *X0h* [101, 102].

For the symmetric Bragg case, the relative width can be related to the extinction length (Eq. 2.72)

$$\varepsilon_G^{(s)} = \frac{d_G}{\pi l_e(0)} = \frac{1}{\pi N_e}, \tag{2.87}$$

with N_e being the number of planes until the extinction length. In conclusion, the more atomic planes contribute, the narrower the reflection. Contrary to the x-ray wavelength, there is no simple general analytical expression for the angular borders of the incident angle for the zone of total reflection at a fixed wavelength. If the angle of incidence is not very close to normal incidence, the angular width can be given by

$$\Delta\theta = \Delta\theta^{(s)}\,\frac{1}{\sqrt{|\,b\,|}}, \qquad \Delta\theta^{(s)} = \frac{2\left|P\chi_G\right|}{\sin 2\theta_c}, \tag{2.88}$$

Figure 2.8: Left: two identical crystals reflecting in (+,-) geometry. The two crystals reflect the beam in opposite directions so the exiting beam passes in the same direction as the incoming beam. Right: two identical crystals reflecting in (+,+) geometry. As both crystals deflect in the same direction, the original beam pointing is not kept.

where $\Delta\theta^{(s)}$ again denotes the symmetric case. The angular acceptance of the reflections is known as the Darwin width. Neglecting the small modification to Bragg's law, this expression can be recast as

$$\Delta\theta^{(s)} = \Delta\varepsilon^{(s)} \tan\theta_c. \tag{2.89}$$

As seen in table 2.1, the angular acceptance of the reflection grows with the tangent of the Bragg angle and is largest in the backscattering geometry, where (Eq. 2.89) is actually no longer valid. The strong backscattering case will not be discussed here, as it is of no concern for the conducted experiments.

Monochromator geometry In a system of multiple Bragg crystals with large distances and angles between the crystals, the single crystals can be treated independently. This means that the radiation scattered from one crystal impinges on the next and no longer interacts with the first one. The total reflectivity of the system is then the product of all single crystal reflectivities,

$$R_{i,\ldots,j} = R_j(\vec{q}_{j,out}, \vec{q}_{0,in} + \ldots + \vec{q}_{j-1,out}) \cdot \ldots \cdot R_i(\vec{q}_{i,out}, \vec{q}_{0,in}), \tag{2.90}$$

where R is the reflectivity as a function of incoming and outgoing wave-vectors $\vec{q}$. Two identical Bragg crystals can be arranged to reflect either in the so called (+,+) or (+,-) geometry (Fig. 2.8).

In the (+,-) configuration, the acceptance angle of the second crystal $\theta_{2,in}$ is given by

$$\theta_{2,in} = \pi - \Psi + \theta_{1,out}, \tag{2.91}$$

where $\theta_{1,out}$ is the exit angle from the first crystal and Ψ the relative angle between the Bragg planes of the crystals , so 0 for parallel Bragg planes. For the central wavelength λ_c follows

$$\theta_{2,c,in} = \pi - \Psi + \theta_{1,c,out}. \tag{2.92}$$

The combination of the two equations 2.91 and 2.92 yields the reflection condition for the (+,-) geometry,

$$\theta_{2,in} - \theta_{2,c,in} = \theta_{1,out} - \theta_{1,c,out} \tag{2.93}$$

From the results of the previous paragraph (Eq. 2.83) it is possible to obtain an expression for the angle between the reflection planes where transmission occurs

$$\Psi = \pi + \frac{w^{(s)}}{2} \left(\frac{1}{b_2} - b_1 \right) \tan\theta_{c,1}. \tag{2.94}$$

This means that for symmetric reflection geometries ($b_2 = \frac{1}{b_1}$) the planes have to be exactly anti-parallel for the optimal transmission. As the angular acceptance of crystals is quite small, fine mechanical precision is needed to align two crystals in such a geometry. Alternatively, so called channel-cut crystals are employed, where the reflecting surfaces are cut out off the same monolith to assure the parallelism between the planes is as good as possible. In perfect alignment, the reflection regions of the two crystals exactly overlap and they fully transmit over their complete total reflection regions.

While, as visible in (Fig. 2.8), the (+,-) configuration conserves the beam pointing, it introduces an offset to the x-ray beam position. In beamlines that operate with and without monochromators like HED, it is of great advantage to have the x-ray beam always arrive at the same position. For these cases, a (+,-,-,+) four crystal geometry can be used to preserve the beam pointing without offset.

Monochromators at HED The HED instrument has two silicon monochromators, which both use different symmetric Bragg reflections. First, is a four-bounce quasi channel-cut Si (111) monochromator [103] in (+,-,-,+) geometry. It is distributed over two vacuum chambers, the first containing a set of crystals reflecting the beam up, the second one down. This monochromator can be cryogenically cooled to 70 K to reduce the effects of thermal expansion under irradiation by the intense x-rays and serves primarily to clean the SASE background from a seeded beam or as a pre-monochromator for the following high-resolution monochromator. It reduces the bandwidth to $\frac{\Delta E}{E} \sim 1.3 \times 10^{-4}$ or ca. 1 eV.

The second monochromator in a third vacuum chamber employs a Si (533) channel-cut crystal, which was manufactured by the x-ray optics group of the Friedrich-Schiller University Jena. Its channel width of 106 mm is adapted to the Si (111) pre-monochromator to compensate the vertical offset imposed by the first crystal set of the Si (111) pre-monochromator at a photon energy of 7.49 keV at the corresponding Bragg angle of 87.9°. Ensuring a zero offset to the nominal beamline has the advantage that the following beamline and diagnostics, as

well as laser optics in the experimental chamber, require no re-alignment when switching forth and back between the regular beam to the monochromatised beam. Using this Si(111)-Si(533) monochromator, the energy width of the incident beam would be reduced to a value of 30.8 meV or a bandwidth ΔE / E of 4×10^{-6}. Offline measurements with a double crystal diffractometer showed a broadening smaller than 10 % of the theoretical rocking curve width [104].

The (533) reflection was chosen because it yields the necessary resolution while having no lower order reflections. This is particularly important when using the setup to study warm-dense matter states, as the plasma emission itself could add strongly to the noise on the IXS signal. For example, when using the Si (444) reflection at an XFEL photon energy of 7.912 keV the scattering setup will also transmit via the Si (111) reflection at a quarter of the photon energy, 1.978 keV, which is emitted from the ablation plasma.

The Si (533) channel-cut crystal was cut from a monolithic ingot. The reflecting surfaces are oriented inward-facing and were sawn with a diamond blade and subsequently polished with SiC of decreasing grain size. Afterwards, the crystal was etched in a mixture of hydrofluoric acid, acetic acid, and nitric acid for 20 minutes. To increase the flatness of the surfaces, the crystal was polished a second time with 38 μm SiC, followed by the same etching process. Despite this, optical wavefront measurements yield a surface roughness with a root-mean-square (RMS) value of $\sim 5\,\mu$m and a peak-to-valley (PV) value of $\sim 20\,\mu$m. In comparison, the Si (111) crystals of the first monochromator stage are more easily accessible and were highly polished, which is technically possible because the crystals are separated in a quasi channel-cut, and have a RMS roughness of order 30 nm with a PV value on the order of 200 nm. Nevertheless, the two reflections from the Si (533) crystal preserve the spatial profile of the beam, most likely due to the high Bragg angle of $\sim 88^\circ$.

One of the main goals of the high-resolution IXS setup is to study extreme states of matter generated by optical drive lasers. The HIBEF user consortium has contributed two high-power lasers to the HED scientific instrument [47, 105, 106] which run at a maximum repetition rate of 10 Hz. Because of this, the monochromator was designed to be able to perform at this repetition rate. Higher pulse rates would be a rare case for these experiments, as, even at $f = 4.5$ MHz, the extreme state will have disappeared before the next pulse arrives after $f^{-1} = 220$ ns. At 10 Hz, the time between two pulses is sufficient to dissipate the heat deposited by the X-ray pulse at the location of the first reflection into the crystal bulk and support structures. Therefore, there is no loss of intensity between pulses due to expansion of the lattice spacing at the first reflection and the Darwin curves overlap at 10 Hz. In 2022, a Si (931) channel-cut was added to the vacuum chamber of the high-resolution monochromator. It operates at photon energies around 10.896 keV at a Bragg angle of $\sim 88^\circ$ and the crystal length is again adapted to the offset generated by the first Si (111) crystal set. This cut yields a spectral bandwidth of 11 meV or $\frac{\Delta E}{E} \sim 1 \times 10^{-6}$

Repeated measurements of the beam's spatial profile at different locations along the beam propagation have yielded a vertical divergence, which is the dispersive direction of the monochromators, of $\leq 1\mu$rad for this collimated beam. Thus, a further reduction of the divergence by asymmetric reflections, often necessary on

high-resolution monochromators at synchrotron radiation sources, where the divergence can be of the order of the crystal rocking curve, is not required for this setup.

Pulse duration considerations Short electromagnetic pulses, like the ones from a XFEL, require a contribution from many different frequencies. Thus, the strong monochromatisation of a FEL pulse may lead to an increase of the pulse duration. A measurement at European XFEL using electron beam techniques yielded a duration strictly shorter than 50 fs for a 7 keV SASE pulse, but more likely on the order of 15 fs [107, 108]. In order to find a minimum to the monochromatised pulse duration, we first model the XFEL pulse as a Gaussian resulting from an chirped electron beam. In this case, a 1.83 eV bandwidth corresponds to a pulse duration of 1 fs. Therefore, an FEL pulse monochromatised with a bandwidth of 30.5 meV FWHM would correspond to a duration of about 60 fs. Any chirp present would only increase the pulse duration. Using the previous assumption that the FEL pulse duration is shorter than 50 fs, we thus conclude that during experiments using high-resolution monochromators, the FEL pulse duration is determined by the bandwidth of the monochromator. The resulting pulse length of 60 fs, though longer than the SASE pulses, does not impose limitations for any experiments described in this thesis. Albeit, it will become relevant for the study of ultrafast electron dynamics before the thermalization of the electron system in fs-laser experiments.

X-ray focusing optics

For the combination with optical drivers, the x-ray spot on sample should considerably smaller than the optical focus. This way, only pumped sample material is probed by the x-rays without creating an undesired background from unexcited material. The x-rays exit the undulators of an FEL with a divergence in the μrad range. After the transport through long beamlines, e.g. almost 1 km at European XFEL, the beam diameter can easily reach several hundred μm at the experiment. This is too large for many laser drivers, which may require focal spots less than $10\,\mu m$ large to reach the experimentally required intensity - not to speak of x-ray heating experiments which require very tight foci. So it is necessary to be able to focus the x-ray beam down to spot sizes in the range of $20 - < 1\,\mu m$.

Nowadays, there exist a number of ways to focus x-ray beams: Kirkpatrick-Baez mirrors [109], multilayers [110], capillaries [111], zone plates [112, 113], and waveguides [114]. However, the experiments presented in this work use compound refractive lenses (CRLs), initially pioneered by B. Lengeler in the 1990s and later commercially manufactured by RXoptics [115]. CRLs work by refracting the x-ray beam, similar to optical lenses. For x-rays, the index of refraction n for x-rays can be expressed as

$$n = 1 - \delta + i\beta, \tag{2.95}$$

where δ composes the refractive part and β is part of the absorption coefficient $\mu = 4\pi\beta/\lambda$. The refractive

component is typically small, on the order of 10^{-6} and competes with absorption. The ideal material for lenses therefore posses a high refraction component together with low absorption. Beryllium has been found to be a good candidate for this purpose. The problem of the low refraction can be solved by adding many lenses together (hence the name *compound*). The focal length f of a stack containing identical lenses in the thin lens approximation (the length of the lens stack being small compared to the focal length) is then given by

$$f = \frac{R}{2N\delta}, \tag{2.96}$$

with R being the lenses radius of curvature and N the number of lenses. For photon energies in the keV range, lens stacks with 10-100 lenses and radii between 5 and 0.5 μm can reach focal spot sizes between 20 and 0.2 μm FWHM.

Analyser crystals

To transform the scattered x-rays from the sample into a usable signal, spherical diced crystal analysers [116–118] are used. As the analysers need to distinguish meV-level differences in the signal, they need to be cut from similarly perfect crystals as the monochromator. The analyser crystals are usually cut to the same crystal plane as the monochromator to ease the matching of photon energies. Also, the analysers should cover a high angular acceptance to collect as much scattered radiation as possible. As shown in the previous section about monochromators, a backscattering geometry is ideal for this.

For the experiments discussed in this work, circular silicon wafers of 10 cm diameter were cut with a saw to produce a grid of $\sim$ 10000 small square crystalites with an edge length of 1.6 mm. These dices were glued to a concave substrate to obtain a spherical curvature, a 1 m curvature radius in our case. Afterwards, the surfaces are etched away to remove any residual strain within the dices. The result is a spherical mirror composed of many individual strain-less perfect crystals that focuses the reflection from each dice to the same point. Every individual dice is a plane crystal that spectrally disperses the x-rays impinging onto it (Fig. 2.9). The dimension of each dice in the dispersive direction determines the width of the spectral window.

It is crucial to align the distances of source, crystal and detector properly, so that all dices are illuminated by the same range of Bragg angles, and that the reflection from all dices superimpose on the detector.

X-ray detectors

The final component to conduct hr-IXS experiment is a suitable x-ray sensitive are detector, in order to measure the x-rays after being reflected and spectrally dispersed by the analyser crystal. The two detector types used for IXS in the later presented experiments are both 2-dimensional area pixel detectors, ePix100 [119] and JUNGFRAU [120,121]. An ePix100 detector has 768 $\times$ 704 pixels and a pixel size of 50 μm. The JUNGFRAU

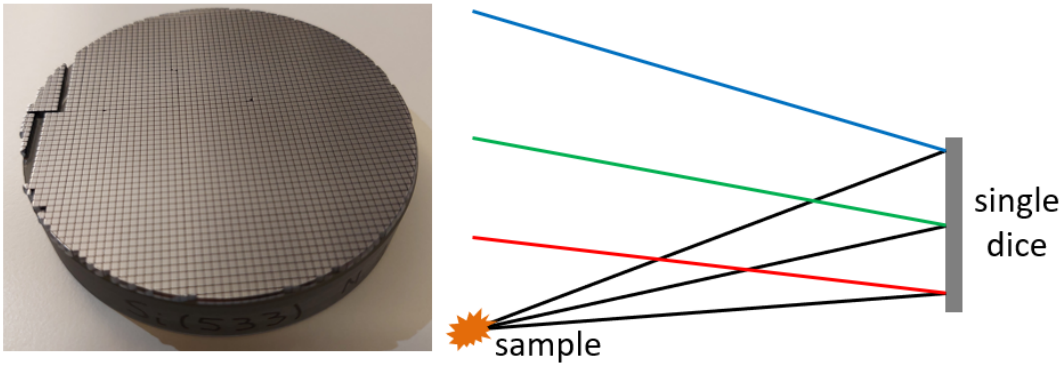

Figure 2.9: Left: photo of a Si (533) diced analyser with 10 cm diameter and 1 m radius of curvature. The top shows some damage in form of missing dices. Right: The sample emits x-rays in all directions. X-rays hitting an individual dice do so at different angles depending on the position. As the Bragg condition needs to be satisfied, different photon energies are reflected to distinct locations.

detector has eight modules 256×256 pixels arranged in a two by four rectangle and a pixel size of $75\,\mu$m. A specialised version for spectroscopy applications with a pixel size of $25 \times 225\,\mu m$ has since become available. Having the same amount of pixels per area but a three times smaller pixel pitch in one direction, it is ideal for experiments which require high sampling in one direction, and are not sensitive to the sampling in the perpendicular direction.

Both detectors are charge integrating with a silicon sensor, meaning that the charge an x-ray photon generates in each pixel is recorded. This implies that there is no minimum photon energy and that a photon doesn't need to be absorbed in a single pixel to be detected. Instead, the energy can be distributed over several pixels. Both detectors are able to continuously read out and transmit their data to the subsequent electronics and IT pipelines at rates exceeding 10 Hz. As laser driver and monochromator limit the repetition rate of the experiments to 10 Hz, there are no problems with the speed of the electronic readout.

Spectrometer geometry

For the detector to deliver usable data, it needs to be arranged in a specific position relative to analyser crystal and sample position. The spectrometers used in this work all employ Rowland-circle geometries [122–125]. Here, sample, analyser and detector are all positioned on a circle with a diameter equal to the bending radius of the analyser crystal. Sample and detector are placed on one side of the circle, facing the analyser on the opposite side. The distance s between sample and detector is determined through the Bragg angle of the probed photon energy

$$s = R \sin 2\theta, \tag{2.97}$$

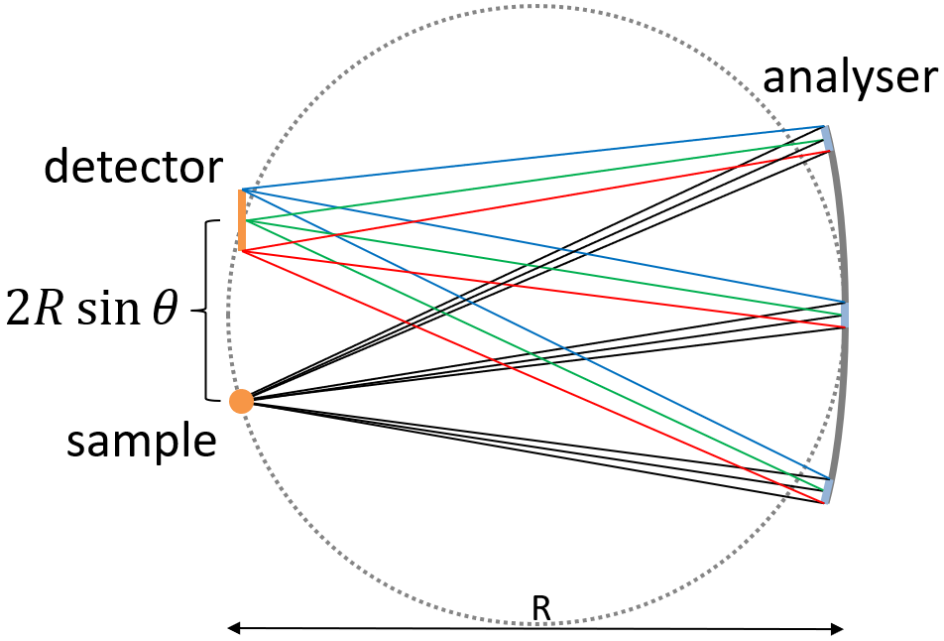

Figure 2.10: Spectrometer in Rowland circle geometry. Sample and detector sit on the left side, the analyser on the right. Radiation emitted by the sample is collected by the analyser. Through the spherical curvature, all dices on the Rowland circle are hit under the same angle, which leads to a superposition of all the dices spectra on the detector. As it is challenging to align sample, detector, and all dices on a perfect circle with sub-mm precision, the intrinsic resolution may broadened in an experiment. Figure adapted from Huotari *et al.* [124].

where R is the radius of curvature of the analyser equal to the circle diameter and θ the Bragg angle. With this geometry and the curved placement of the dices on the analyser, the detector sees a superposition of the images from individual dices. As every individual dice is dispersive, the image on the detector is magnified by a factor of two. In this 2-dimensional image, one direction spatially images the sample, the other encodes the spectral information from the scattered radiation (Fig. 2.10). The dispersion along the spectral axis is given by

$$\frac{\Delta E}{\Delta x} = \frac{E}{2R\tan(\Theta)}. \tag{2.98}$$

In the ideal case, the resolution of this spectrometer is only defined by the Darwin width $\Delta\theta_D$ of the reflection (Eq. 2.89

$$\frac{\Delta E}{E} = \frac{\Delta\theta_D}{\tan\theta}. \tag{2.99}$$

This is commonly called the intrinsic resolution of the spectrometer. The resolution can be impaired by broadening from several sources. First, the real source of the scattered radiation is no point source but a cylinder

stretching along the sample thickness t with an circumference equal to the x-ray focus spot size a. Therefore, the analysers see an effective source size s_{eff}

$$s_{eff} = t\sin(\theta) + a\cos(\theta). \tag{2.100}$$

The broadening due to the finite source size is then given by

$$\frac{\Delta E}{E} = \frac{s_{eff}}{R\tan\theta}. \tag{2.101}$$

Next, the detectors cannot resolve two photons, if their spectral separation after the dispersion through the analysers is smaller than the size of a pixel. This pixel broadening is equal to the dispersion over one pixel length and can be expressed as

$$\frac{\Delta E}{E} = \frac{p}{2R\tan\theta}, \tag{2.102}$$

where p is the dimension of a quadratic pixel. Lastly, there is a spectral broadening due to the fact that not all components can be perfectly aligned on the Rowland circle. For spherical bend crystal analysers, only the centre lies on the Rowland circle, as the circle has a diameter equal to the radius. So, all dices are no longer hit under the same angle, leading to a broadening of the spectrum. This effect is called *Johann error* and can be estimated [126] to be

$$\frac{\Delta E}{E} = \frac{\Delta\theta_J}{\tan\theta}, \tag{2.103}$$

where $\Delta\theta_J$ is weighted average over the distributions of Bragg angles over the analyser dimension. It can be approximated through

$$\Delta\theta_J = \frac{\left(\frac{A}{R\sin(\theta-\alpha)}\right)^2}{8\tan(\theta-\alpha)}, \tag{2.104}$$

where A is the radius of the analyser and α the asymmetry angle of the reflection. The Johann error can be bypassed in exact backscattering or with the use of Johansson crystal analysers. For these crystals the reflecting planes are not parallel to the surface. Instead, the surfaces follow a sphere with diameter R, while the crystal planes are aligned to a sphere with radius R. As these crystals are very difficult to produce, they are not widely used and were not employed in this work.

All experiments conducted in the scope of this work use three diced analysers simultaneously in order to collect more scattered photons. One analyser always sits above the x-ray beam axis, the other two are

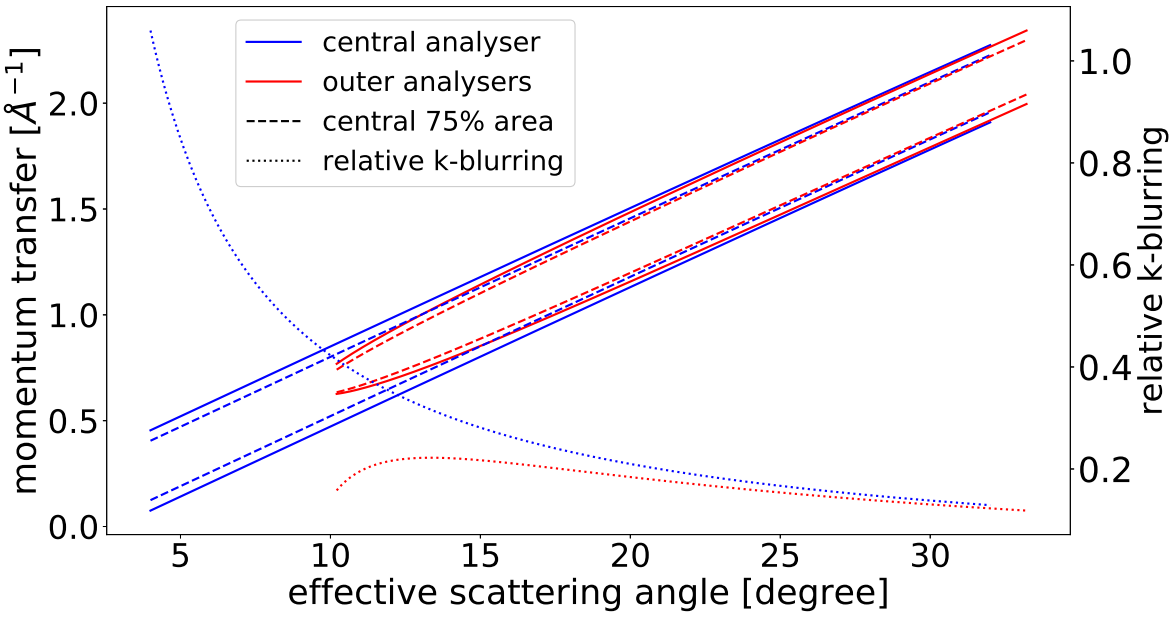

Figure 2.11: Acceptance of momentum transfers for the on-(blue) and off-axis (red) analysers. The dashed lines show the same for the case of masked analysers. The relative blurring of the central momentum transfer vector due to the dimensions of the analysers is shown by the dotted lines. Figure from Wollenweber *et al.* [127]

symmetrically offset to both sides. These two analysers observe the target under a different scattering angle Θ_{eff} than the on-axis analyser

$$\Theta_{eff} = \arccos(\cos(\Theta)\cos(\phi)), \tag{2.105}$$

where Θ is the on-axis scattering angle and ϕ the angle to the beam axis. As the analyser have a finite spatial extension, they do not only collect photons at one momentum transfer but an ensemble of scattering vectors. A visualisation of this effect is shown in Fig. 2.11 for the standard setup for forward scattering at the HED instrument.

2.3.3 Scientific instruments

As an example for a general setup of a FEL experiment station, I will give a brief overview of the High Energy Density scientific instrument at the European XFEL. Details of the very similar MEC instrument at the Linac Coherent Light Source (LCLS) can be found in the report by Nagler *et al.* [128].

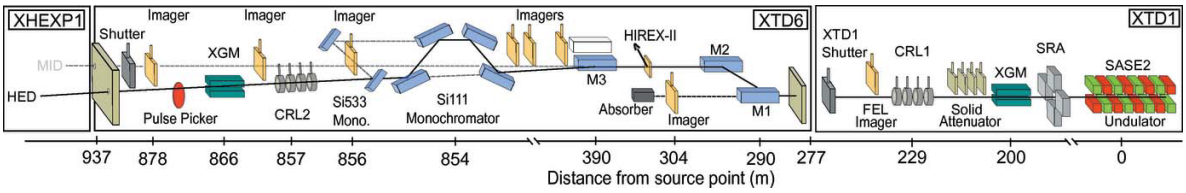

Figure 2.12: A sketch of the beamline from the undulator source leading up to the HED instrument including most beamline elements. The x-ray beam is generated in the undulators on the right. Figure from Zastrau *et al.* [131].

The High Energy Density scientific instrument

The HED scientific instrument is one of two endstations at the hard X-ray SASE2 undulator of the European XFEL [41, 129, 130]. It is designed to probe extreme states of matter with various X-ray methods. A general overview of the HED instrument is given by Zastrau *et al.* [131]. This section shall give a brief overview of the SASE2 beamline and HED instrument, beginning at the radiation source. An overview of the installations is shown in figures 2.12 and 2.13.

The beamline spans over two subsequent tunnels, XTD1 and XTD6, and has an overall length of ca. 1 km. The complete beamline is operated under UHV conditions. At the beginning, x-rays are generated in the hard X-ray SASE 2 undulator of the European XFEL [130, 132]. The undulator system has a length of roughly 175 m and contains two electron chicanes and diamond monochromators for self-seeding. It is driven by an electron accelerator, which accelerates electron macro-bunches at a base rate of 10 Hz. Each of the macro-bunches can contain between 1 and 2700 electron bunches separated by a minimum time of 220 ns or 4.5 MHz, which are distributed between the experiments at European XFEL. Usually, the machine is operated at a repetition rate of 2.25 MHz. An x-ray gas monitor (XGM) measures the x-ray pulse energy behind the undulators, another one is located towards the end of the tunnel, close to the experiments and downstream of all tunnel optics [133]. At several locations along the beamline, fluorescing screens out of doped diamond or YAG can be inserted into the beam to monitor the spatial profile with cameras [134].

Located 230 m behind the undulator exit is a set of CRLs (CRL1) which can either focus directly on target, create an intermediary focus before the target location or collimate the beam. Following this is a pair of horizontal offset mirrors to suppress higher harmonics of the fundamental photon energy of the undulators. After these mirrors exists the HIgh REsolution hard X-ray single-shot (HIREX) spectrometer [135], which can spectrally resolve single x-ray pulses. A third mirror shifts the x-ray beam between HED and the Materials Imaging and Dynamics (MID) instrument [136], whereas MID lies directly in line and HED requires the insertion of the third mirror to deflect the beam south by 1.3μrad. Further downstream, ca. 850 m after the undulators and 120 m upstream of the experimental area, the previously discussed monochromators are situated. A second set of CRLs (CRL2) is located behind the monochromators, which can focus the beam down to a minimal size of

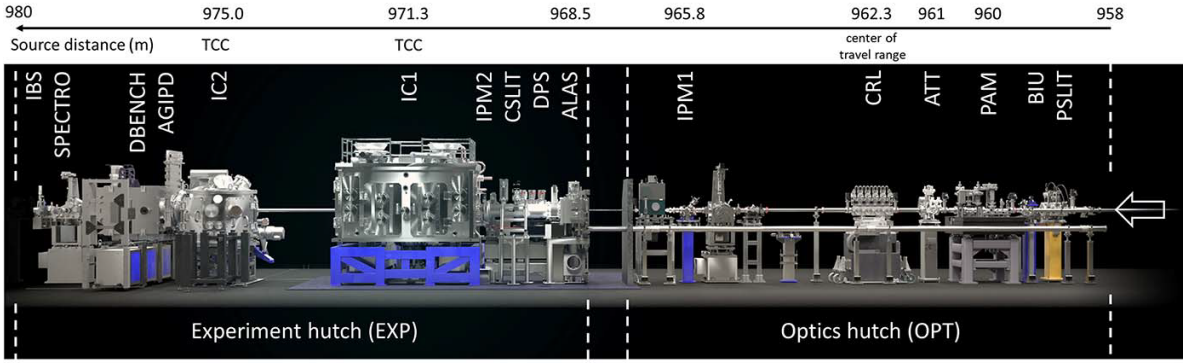

Figure 2.13: A model of the HED experimental hutch and and the optics hutch in front of it. The x-rays enter from the right. Figure from Zastrau *et al.* [131].

$\sim 15\,\mu$m at target location. The final element in the tunnel is a pulse picker to only let certain x-ray pulses pass for shot-on-demand experiments. This way, the undulator system with all electron feedbacks can still operate at nominal repetition rate, which is necessary for a stable operation of the FEL.

Leaving the tunnels and entering the experimental hall are the optics and experimental hutches of the HED instrument (Fig. 2.13). The optics hutch contains amongst others slits to cut off beam halos, another set of CRLs (CRL3) 9 m in front of the target, which can focus the beam below $10\,\mu$m at target location [137], and the photon arrival monitor. At the photon arrival monitor, a leakage of the fs-driving lasers at HED [47, 138] can be coupled with the x-rays to monitor timing on fs-scale while conducting an experiment.

In the experimental hutch, a differential pumping section connects the UHV beamline to the HV interaction chamber 1 (IC1), which is typically kept at a vacuum level of 10^{-5} mbar to enable compatibility with high-intensity and high-power laser experiments. IC1 has a size of of $\sim 2.5\,m \times 1.5\,m \times 1\,5m$ and its floor consist of an optical breadboard 30 cm below the x-ray beam level. In addition, one of the walls holds a set of circular vertical rails with sleds that can rotate around the chamber centre. IC1 can contain a variety of experimental setups, one of which is the IXS setup. Behind IC1 is room for a secondary interaction chamber, IC2, which is specialised for experiments with diamond-anvil cells and laser shocks [139].

Chapter 3

Iron in Earth's Interior

By mass, iron is the most abundant element on Earth. It constitutes about 80 % of Earth's core and is the 4th most common element in Earth's crust [140]. The core consists of two parts. A molten outer core and a solid inner core. The molten outer core, starting at 2870 km depth, consists of iron alloyed with ∼10 % of lighter elements by weight [141]. Second, beginning at 5125 km depth, the solid inner core contains ∼80 % iron, ∼10 % nickel, and some light element impurities [142]. Some conditions within the core, like density, can be inferred in-situ by seismological measurements. Others, like temperature, are usually interpolated from known conditions. In the outer core, pressures reach from 135 GPa at the core mantle boundary (CMB) to 330 GPa at the inner core boundary, where the iron-nickel composition has a density of $\sim 12.6 \frac{g}{cm^3}$.

The understanding of the properties of iron under core condition enables detailed modelling of Earth's behaviour and comprehension of geophysical effects like the dynamo effect [2] generating Earth's magnetic field. This magnetic field enabled the evolution of complex life on the planets surface by deflecting the ionizing stellar wind. In addition, it allows the validation of planetary formation and evolution models and the prediction of properties of Earth-like exoplanets. At the moment, the geodynamo is thought to originate from fluid motion inside the liquid outer core. Heat flow deep inside the planet therefore plays an important role not only for the geodynamo but also for the cooling rate of the planet, inner core growth and at some point volcanism [143].

Despite extensive studies into high pressure state of iron for more than five decades, some properties and conditions at Earth's core are still unknown and disputed. Probably the most important unmeasured thermodynamic parameter is the temperature. Its exact determination is a still ongoing process, attempted with static and dynamic compression experiments [144, 145]. These experiments and numerous simulations were able to impose boundaries on the temperature value at the inner core boundary, putting it in the region of $6230 \pm 500\,K$ [144].

Following the temperature, the crystal structure and melting line of iron under Earth's core conditions are still unknown. The observed anisotropy for sound waves propagating along the rotation axis or equatorial

plane could be explained by different crystal structures at high pressure and temperature [146]. Though recent experimental results seem to confirm the stability of the high pressure iron hcp phase [147] and a melt line slightly above estimated core temperatures [145], but inside the error bar [144].

Iron containing compounds are also a constituent of Earth's mantle. Their chemical and physical properties therefore influence the behaviour of a major part of Earth [148–150]. Current experiment schemes regularly measure density and crystallographic state by x-ray diffraction and electronic spin state by emission spectroscopy, but the temperature is inferred from equation of state data or from simulations. For example, Kaa *et al.* [149] use finite-element analysis to calculate their sample's temperature response to the absorption of the x-ray pulses during a pulse-train of European XFEL. An example about their temperature estimates is shown in Fig. 3.1 (left). Here, and in many other experiments, accurate temperature measurements using methods as presented in this thesis could therefore put experimental results on more solid grounds and help clarify many open questions about our home planet.

It is in this context that I designed the experiment presented in chapter 4.2. The goal of the experiment was to extend the previously demonstrated IXS temperature measurement (see chapter 4.1) to a dynamically driven sample. In this experiment, we used a laser to compress and heat an iron sample to conditions of high pressure and temperature, in order to have a relevant sample to demonstrate the temperature measurement on a dynamically driven sample.

Inelastic x-ray scattering in the meV range have been performed on high pressure hcp-iron samples in diamond anvil cells (DAC) to gain a more detailed understanding of vibrational, elastic, and thermodynamic properties. The measurement of the phonon density of states (Fig. 3.1 right) [151] in DAC allowed the determination of amongst others vibrational heat capacity and entropy as well as the Debye temperature.

The phonon density of states of iron at ambient pressure and for a pressure equivalent to the Earth's outer core (153 GPa) is shown (Fig. 3.1(right)). It can be seen that phonons modes exist between 20-40 meV at ambient pressure, whereas they move to higher energies with pressure, as density and consequently sound speed increases. Therefore, inelastic x-ray scattering from acoustic phonon modes in iron requires a energy resolution of a few 10s of meV. At room temperature ($300\ K \sim 25$ meV) these modes are only weakly populated, while at temperatures ~ 1000 K they will contribute significantly. Experimental results are presented in chapter 4.2 of this thesis.

Besides these fundamental reasons in basic science, there are a multitude of reasons to be found in applied sciences and technological applications to investigate the behavior of iron and iron-bearing compounds at conditions of high temperature, pressure, and its dynamic behavior in non-equilibrium on short time scales. These range from industrial applications which optimize the laser-cutting of steel with femtosecond lasers, to impact science, explosive conditions, stress-strain of steel in ground and space applications, and synthesis of new materials under high pressure-temperature conditions, to name a few.

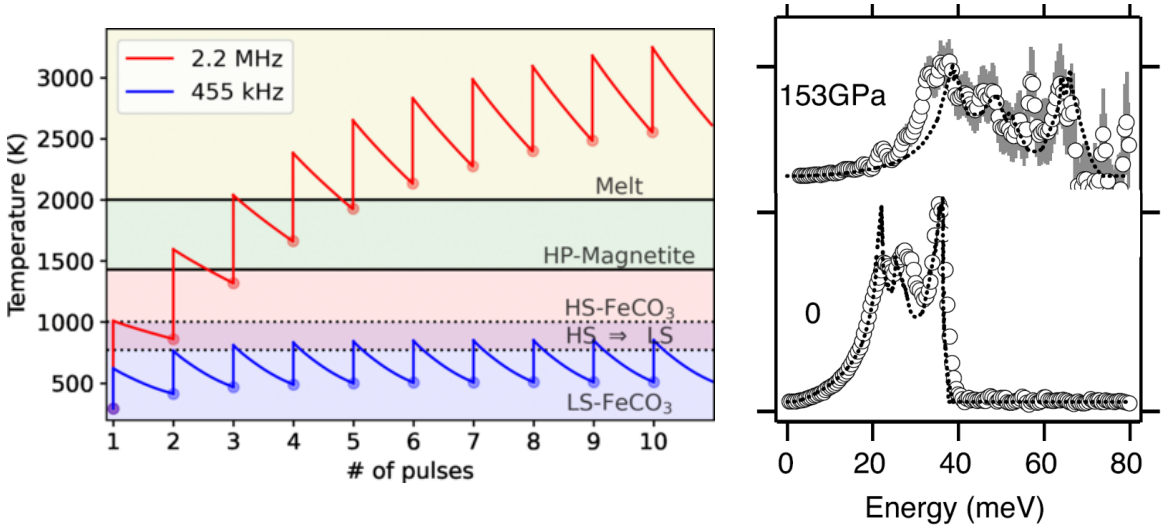

Figure 3.1: **Left**: Simulation of the x-ray heating cycle of iron carbonate within each train of x-ray pulses at 2.2 MHz (red line) and 455 kHz (blue line). Figure from Kaa *et al.* [149]. **Right**: Hcp-iron phonon densities of state. High-pressure states were generated inside a diamond anvil cell. The white circles are measurement results from nuclear resonant inelastic x-ray scattering (NRIXS), their errors indicated by the grey bars. The black dotted line shows a simulation result. Pressures of 153 GPa are reached within Earth's outer core. As the lattice compresses under high pressure, the phonon modes shift to higher frequencies. Figure modified after Mao *et al.* [151].

Chapter 4

Experiments

This chapter contains the analysis of the experimental data that was obtained within the span of this thesis. In particular, the presented data was collected during the following experiments: European XFEL HED 2191, HED 2656, LCLS MEC LV2518, and MEC LY2720.

4.1 Resolving low-frequency structural dynamics in static systems

The HED scientific instrument at the European XFEL entered user operation in May 2019. The aim of this very first experiment, referred to as HED 2191 "Resolving low-frequency structural dynamics at the HED scientific instrument", was to show the ability to resolve low frequency structural dynamics in solids and to prove that the platform, which we designed, can indeed perform an accurate temperature measurement. In particular, we first wanted to show that the combination of monochromator and diced analyser crystals can reach the design resolution. Previous measurements with an x-ray tube proved that the quality of the monochromator crystal is very good and thus can provide the necessary resolution [104]. One remaining question was whether this channel-cut crystal can sustain long-term FEL exposure without heating up too much and as a consequence loosing transmission. As a next step, we planned to show that we can distinguish between two well defined temperatures of a target material only from the analysis of the IXS signal. I have helped to prepare and setup the experiment, and participated in the control room shift during the experiment. Afterwards, I did the data analysis. The results of this beamtime have been published in peer-reviewed journals: Wollenweber *et al.* [127] and Descamps *et al.* [152].

4.1.1 Instrument resolution at HED with Si (533)

In this first part I will introduce the IXS setup at HED (European XFEL) and give an overview of the activities we did to characterize the IXS spectrometer.

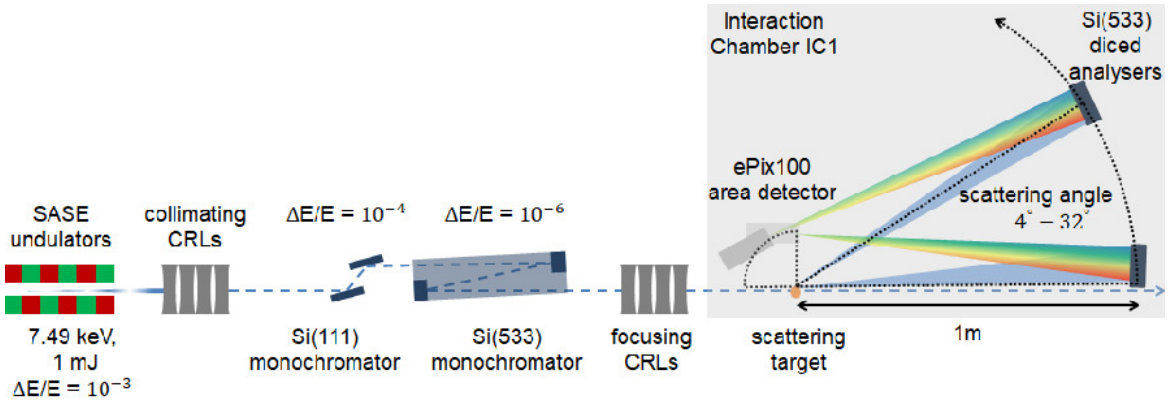

Figure 4.1: Schematic view of the high-resolution IXS setup at HED. X-ray pulses are generated in the SASE undulators on the left. Afterwards, the beam is collimated by a set of CRLs. The collimated beam passes a two-bounce Si (111) pre-monochromator to reduce the bandwidth and heat load impinging onto the subsequent Si (533) high-resolution monochromator. Then, the monochromatised beam is focused to a few μm spot at the target location by another set of CRLs. In the target chamber, the scattered radiation is collected by spherical diced Si (533) analyser crystals and focused on the detector above the target. Together, target, analysers, and detector form a Rowland circle of 1 m diameter. Figure from Wollenweber *et al.* [127].

Experimental Setup

The setup implemented at HED is conceptually based on the successful design used at the LCLS as described by McBride *et al.* [153]. A scheme of all important elements is shown in figure 4.1.

For this experiment, the XFEL was operated in single bunch SASE mode at a repetition rate of 10 Hz with a photon energy centred at $E = 7.49$ keV and a bandwidth of roughly $\Delta E = 20$ eV. The average pulse energy was 1 mJ, measured right after the source. The beam was collimated with CRL1 (see 2.3.3) and propagated to the monochromators. The Si (111) monochromator was operated at room temperature. We decided against the option to cool the crystal to cryogenic temperatures, as heat load effects are insignificant with single bunch operation (1 x-ray pulse every 100 ms), and cryogenic cooling introduces vibrations into the mechanical setup which translate into x-ray pointing jitter.

After passing through the monochromators, the beam was focused with CRL3 to a size of ca. 20 μm at the target location. All targets were mounted inside the Interaction Chamber 1 (IC1) at the nominal centre of rotation of the vertical rails, which holds the analysers. An ePix100 x-ray area detector was mounted 8 cm above the target to complete the Rowland circle geometry (see 2.3.2).

As the instrumentation was never used before this experiment, the first step was to show the resolving capabilities and with it the baseline for future measurements. The resolving power was measured by observing the x-ray scattering from a selection of amorphous solids. In particular, multiple Polymethylmethacrylat (PMMA)

(Goodfellows, Ltd) and amorphous SiO_2 samples of various thicknesses were used. The resolving power of our setup is too low to resolve the low-energy and strongly dampened modes of these materials, so only a quasi-elastic peak is visible in the scattering signal. This peak gives us an accurate measure of the achievable spectral resolution.

Diced-analyser alignment

Before the experiment, all three diced analyser crystals and the x-ray area detector were pre-aligned, first by measuring the distances of the Rowland circle to an accuracy of ¡ 0.5 cm with a paper ruler. Then, an optical laser positioned at the sample location was used to aim the optical reflection from the analysers onto the detector. This method does not guarantee that the analysers are aligned at the optimal Bragg angle and focusing distance. To increase the quality of scattering signal, an outer ring of ca. 1 cm width was installed and masked with aluminium foil on all three analysers, as some of the analysers' dices are missing or damaged along the edges which could result in stray reflections an undefined signal strengths. This measure has the additional benefit of reducing the Johann-error [122] of the spectrometer but leads to a slight signal decrease due to the reduced solid-angle coverage.

The analyser crystal acts like a spherical concave mirror and needs to be focused correctly to produce a sharp 1:2 image. Defocusing will result in a poor overlap of the spectra from each individual dice and this in turn will degrade the spectral resolution (2.3.2). For the optimization of the analysers focusing, the SASE beam was used instead of the monochromatized beam, as this gives the highest number of photons for quick alignment. As a result of the spectral width of the SASE pulses, a multitude of photon energies falls on the analysers and their whole spectral window is illuminated. The expected image on the detector in this case consists of three squares of width 3.2 mm, one for each analyser. All images of all dices overlap when these three squares have sharp corners and a minimum extension.

First, the foci of all three analyser crystals were separated to allow the analysis of the signals of individual analysers, as some of them were initially overlapping as a result of the optical pre-alignment. To find the best focus, the common detector and each individual analyser crystal were scanned along the focus direction at a step size of 1 mm, while being exposed to x-rays scattered from a 100 μm SiO_2 sample at the target location. Here, the parameter to optimize was the edge sharpness of the square reflections of the analysers. The focus of the central analyser is shown exemplary in figure 4.2 on the left side. The right side shows projections along the detector axes, where y is the dispersive direction of the setup. In disagreement with expectations, the size of the focus of $3.16 \times 3.16 mm^2$ shown here is slightly smaller than the expected $3.3 \times 3.3 mm^2$ from design calculations. A likely explanation for this is a misalignment of the Rowland circle to compromise between all three analysers because of mechanical limitations, which leads to a small demagnification of the image on the detector. At the same time, the focus shows a very good agreement with the square shape of the dices. As the

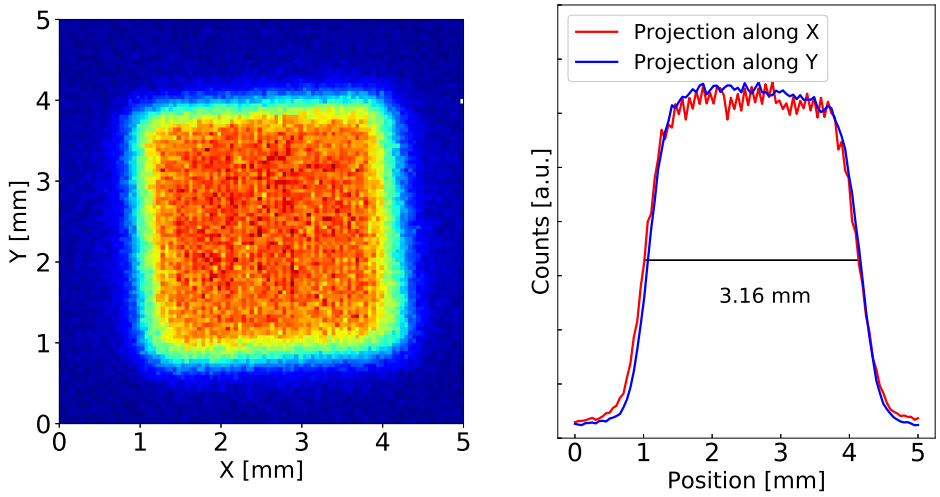

Figure 4.2: Left: Focus of the central analyser after optimisation of all three analysers and sample stage position. Right: The projections show a very good agreement with a square shape, which is sign for the high quality of the diced analysers. Albeit, the size is slightly smaller than expected, which is an indicator of flawed alignment.

focus is a superposition of the reflection of all dices, this shows the high quality of the analyser crystals. Both of the other analysers show a similar picture.

Following the successful SASE alignment, the monochromators were added into the x-ray beam. To achieve the widest spectral window, the Bragg angle of the high-resolution monochromator was adjusted until the position of the narrow bandwidth quasi-elastically scattered line was roughly in the middle of the formerly observed SASE squares. During the whole experiment, the left analyser consistently showed the weakest scattering signal, most likely due to some support structure in the vacuum chamber shadowing the crystal.

Data treatment

With the high-resolution monochromator in the beam the scattering signal on the detector gets quite weak, reaching from thick, elastically scattering samples with some 10s photons per shot to less than 1 photon per shot on average for very thin and/or only inelastically scattering samples. The detection of these single photon events can easily be done via algorithms for every single detector image. It can benefit from the fact that photons of similar photon energy create roughly the same amount of charge and thus analogue-to-digital-unit (ADU) counts inside the detector pixels. Thus, a histogram of the detector counts (Fig. 4.3) will have a peak at the amount of charge a single 7.5 keV-photon will generate. A strong elastically scattering sample will even have a small peak at twice that value, where two photons hit the same pixel. For this work, the charge at the centre of the first peak $\pm 20\,\%$ will count as a single hit. The largest peak of the histogram is at zero, as most

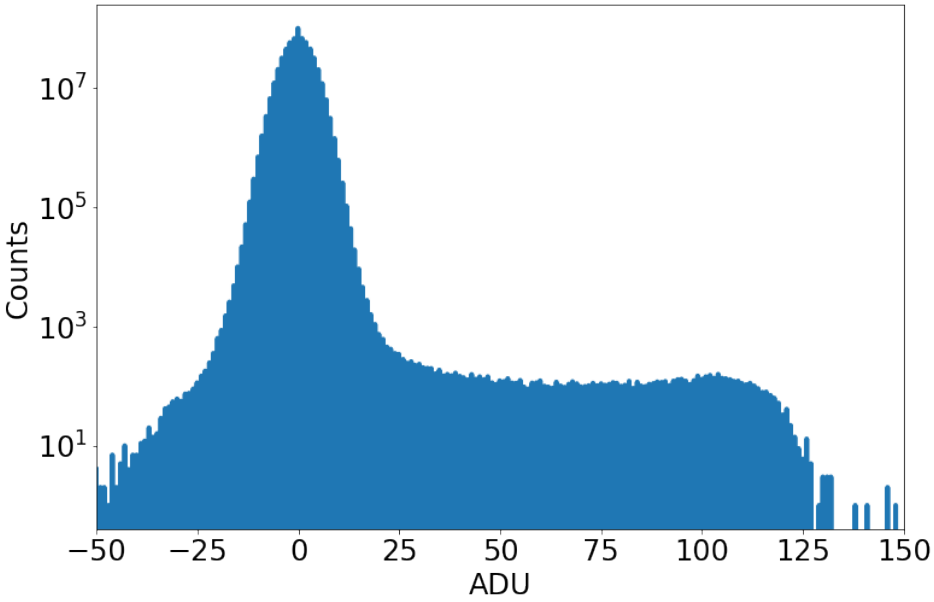

Figure 4.3: A histogram generated from 1099 background corrected images of an ePix100 detector from x-rays at 7.5 keV hitting a 50 μm PMMA sample. Most pixels on average are not hit by a photon and thus receive no charge, which produces the large peak at 0. From around 25 to 100 ADU exists an almost uniform distribution of generated charge, as single photons spread their energy over multiple pixels. After 100 ADU, the number of counts slightly rises. This corresponds to photons depositing most of their energy in a single pixel. 7.5 keV photons are unable to generate more charge than the cut-off at around 130 ADU.

pixels won't get hit by any photons and therefore have zero charge, except a small amount of readout noise. The area between those peaks shows a continuous distribution of generated charge. These are produced, when a photon doesn't generate the corresponding charge in a single pixel but distributes it over multiple pixels. The lower boundary for the detection of multi-pixel hits is set by the width of a Gaussian fitted to the readout noise peak.

Hence, the simplest form of a single-photon detection algorithm checks every pixel for its charge value. If it is within the previously mentioned charge band around the first peak, it counts as a single photon hit. When the algorithm detects a lower charge level, it sums up the charges of the surrounding pixels. If the result falls within the $\pm 20\,\%$ band, it again will count as a single photon hit, identifying it as a single photon hitting multiple neighboring pixels. Accounting for for double hits can be neglected due to their rarity. Going over every pixel and saving the hit positions for every detector image will yield the spectral distribution without any noise floor (background-free signal). An example of elastic scattering from a 250 μm SiO_2 target is shown in figure 4.4. The brightest spots indicate positions where more than ten photons hit the same pixel, down to single photon hits barely visible above the background. As each analyser images a radiation cone emitted by the sample, the

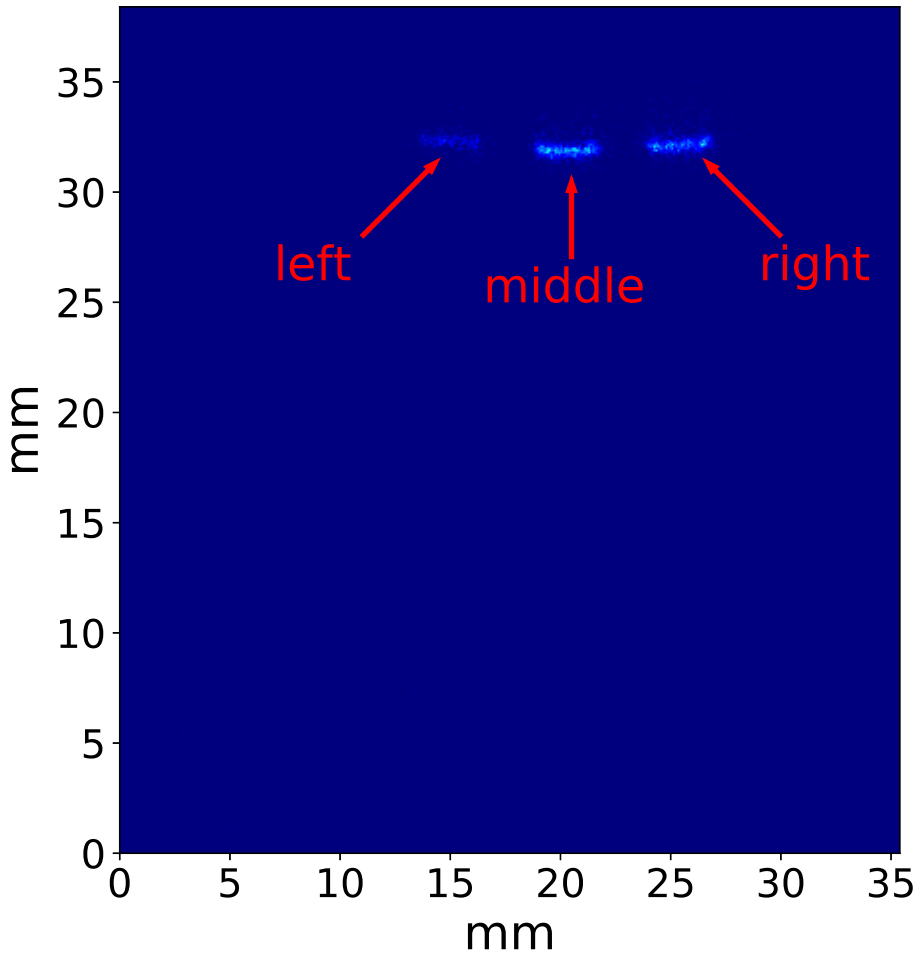

Figure 4.4: Quasi-elastic scattering signal from 250 μm SiO_2 after single photon counting from 960 individual detector images. The foci of all three analysers can clearly be seen in the top of the image. Both the left and the right analysers' foci are tilted by 9°, due to their position on the Rowland circle.

individual images show a curvature in the direction of the energy dispersive axis. Additionally, the spectra from the off-centre analysers are tilted by 9.4° due to their position on the Rowland circle.

To get an undistorted lineout from all scattered photons, curvature and tilt need to be corrected. For this I fitted a circle through the positions of the scattered photons on the 2D detector, weighted by intensity. Then the origin of the Cartesian coordinate grid, corresponding to the pixel array of the detector, is moved to the centre of the circle and transformed to polar coordinates. In the next step, the extrema of radius and polar angle are used to define a new Cartesian coordinate grid with the origin moved to the original circle centre. The original image is mapped to this new coordinate grid to correct the tilt of the outer analysers. This process can then be applied to the individual analysers images to correct the curvature.

Photon energy and dispersion

At the time of the experiment, the options at the HED instrument for measuring the absolute photon energy (e.g. spectrometers or calibration of monochromators) were still very limited. Unfortunately, the dispersion of the setup changes rapidly with the absolute photon energy. Possible transmittable photon energies are limited by design and pre-alignment of the setup, but there was still some leeway around the design photon energy of 7.494 keV. Therefore, the offset between the higher beam of the pre-monochromator and lower beam of the high-resolution monochromator, together with the known dimensions of the channel-cut crystal, were used to calculate the photon energy. The images of the x-ray beam were recorded on a YAG screen, which sits roughly 80 m behind the monochromators. An overlay of images with the x-ray beam after the Si(111) pre-monochromator and after the Si(533) high-resolution monochromator is shown in figure 4.5.

It is mechanically impossible to measure both beams at the same time, but the images were taken within a time span of approximately five minutes. Therefore, disturbances like a shift of the photon energy due to a drift of the linac electron energy are unlikely. The centre of mass of the average image of each beam was taken as a basis for the calculations. With this method, the x-ray wavelength λ is given by

$$\lambda = 2d\cos\left(\frac{\arctan\left(\frac{\Delta x}{l}\right)}{2}\right), \tag{4.1}$$

where d is the interplanar spacing of the Si (533) crystal, Δx is the offset between incoming and outgoing beam of the high-resolution monochromator, and l the distance between the two channel-cut surfaces. Entering an offset of $\Delta x = 7.96 \pm 0.2\,mm$ from the measured centres of mass, $l = 106 \pm 0.01\,mm$, and $d = 1.656446\,\text{Å}$ [154] into this formula yields a photon energy of $E = 7490.2 \pm 0.2\,eV$ at a Bragg angle of $87.85 \pm 0.05°$. The source of the errors is the uncertainty of the centre of mass position due to fluctuations of the FEL beam spot shape, intensity, and spatial jitter. For the determination of the spectrometer dispersion, the same calculation was done for measurements with slightly different Bragg angles of the high-resolution monochromator and hence slightly different photon energies. These calculated energy changes were correlated with the changing position of the quasi-elastic line on the detector. A selection of these steps is shown in figure 4.6.

Here, the shift of the quasi-elastic line relative to the zero position where the actual measurements were done, indicated by the central red line, is clearly visible. Two linear regressions yield values of 5.4 eV per motor step and 704 pixel per motor step, resulting in a spectrometer dispersion of

$$7.7 \pm 0.5\,\frac{meV}{pixel} \quad \text{or} \quad 0.15\,\frac{meV}{\mu m}. \tag{4.2}$$

Again, the error is stemming from beam instabilities but also motor backlash. If this dispersion value is taken and the photon energy calculated after equation 2.98 with a perfect Rowland circle diameter of 1 m, the resulting

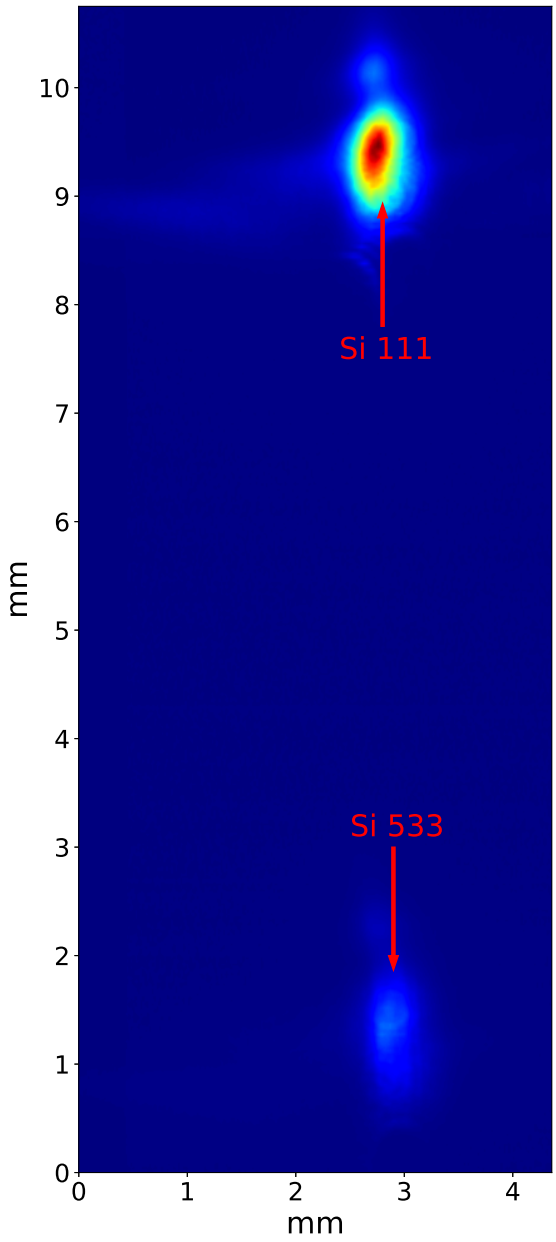

Figure 4.5: Overlay of pre-monochromator and high-resolution monochromator beams on a YAG screen. Each beam is averaged over approximately 2000 shots. The values of the pre-monochromator beam were divided by ten to keep the intensities comparable.

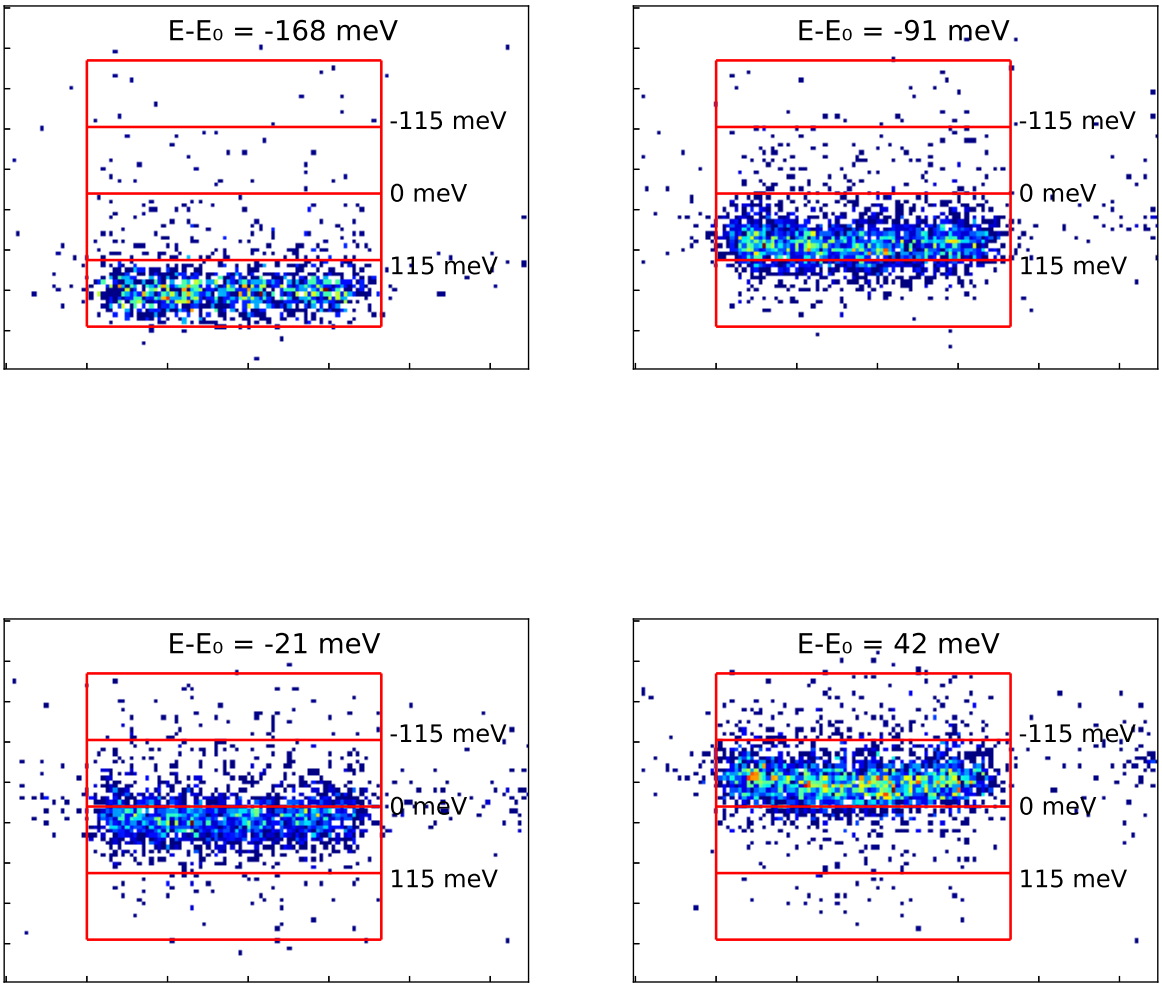

Figure 4.6: Signal from the central analyser crystal for different positions of the Bragg angle of the high-resolution monochromator channel-cut crystal. The outer red lines indicate the outline of the SASE squares. Modified after Wollenweber *et al.* [127].

photon energy is 7490.95 eV. This deviates from the previously stated 7490.2 eV, which yields a slightly lower dispersion of only $0.141\,meV/\mu m$. This value is at the outer edge of the given error interval of 6 %. The errors stated here solely stem from the uncertainty on the recorded beam positions. Further contributions could result for example from Rowland circle mismatches and inaccuracies of the analysers banding radii.

Spectrometer resolution

With the photon energy and dispersion of the setup known, it is possible to translate the pixel positions of the detector images into an absolute energy shift. The full width at half maximum (FWHM) value of the peaks is used here as a measurement parameter to judge the spectral resolution. A theoretical limit to the resolution is given by the convolution of the Darwin curves of the monochromator and analyser crystals. This value is 42.8 meV for a photon energy of 7490.4 eV. If one assumes a Gaussian distribution of all factors constituting to the resolution, the result is 44 meV after including pixel and source broadening [Table 4.1]. This result agrees with the best measured resolution from a 50 μm PMMA target (Fig. 4.7). The measured data is subjected to the Poisson counting error, indicated via the error bars. To retrieve the fwhm value of the spectral peak, the data was fitted with a Voigt profile. For the fitting the Python extension lmfit [155] was used.

Contribution	ΔE (meV)
incident bandwidth	30
analyser	30
pixel size	7
source size	7
Total	44

Table 4.1: A collection of all factors contributing to the resolution. All factors are assumed to contribute with a Gaussian shape. The overall resolution is taken as the convolution of all contributing factors

Since the diced analysers are a 1:2 imaging optic, the size of the scattering source can degrade the spectral resolution if it is larger than 1 pixel on the detector. To experimentally study the impact of source broadening on the spectral resolution, PMMA targets with thicknesses of 50, 500, and 1100 μm were used. It can be seen, that the width of the quasi-elastic peak correlates with the thickness of the sample (Fig. 4.8). Since the diced analysers are at an angle to the target, the effective target thickness t_{eff} each analyser sees is given by

$$t_{eff} = t \cdot \sin(\theta_{eff}) + f \cdot \cos(\theta_{eff}). \tag{4.3}$$

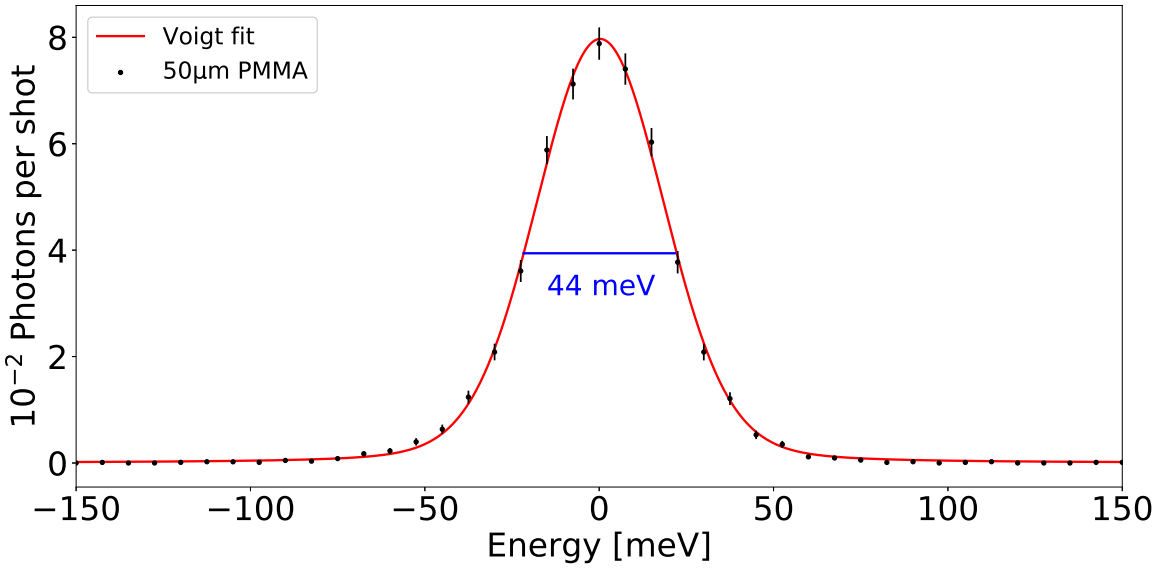

Figure 4.7: Spectrum from 50 μm PMMA from the middle analyser summed over 8500 XFEL pulses (black dots). The error indicated is the Poisson counting error. This is the highest resolution spectrum obtained during the characterization. The data points are fitted with a Voigt profile (red line). The position of the fwhm line of 44 meV is marked.

Here, t is the actual thickness, f the X-ray focus width on target, and θ_{eff} the effective scattering angle as defined earlier (Equation 2.105). This geometrical effect also explains why the two outer analysers generally have a worse resolution than the central analyser, as they see a broader source and consequently collect radiation from different source points. With the existing setup, target thicknesses below this value do not suffer from a decreased resolution. The observed values agree with results obtained previously with a similar setup at LCLS [153].

4.1.2 Proof of concept: Phonons in diamond

This section will describe the results obtained from a single crystal diamond target (supplier: Applied Diamond, Inc.). The aim of this measurements was to proof the capability to actually measure an inelastic signal and then accurately measure its temperature. A single crystal diamond was chosen as the target, as it exhibits no quasielastic scattering component which could hamper the inelastic measurement (in a perfect crystal, the only defects are at the surfaces). Also, due to the high sound speed in diamond, the phonons are quite distinct and farther away from the elastic line than in most solids, which will make it easier to resolve. The first series of measurements was done at room temperature, the second series with a resistive heater set to 500 K.

The diamond had a thickness of 250 μm, which is half the attenuation length at the used photon energy.

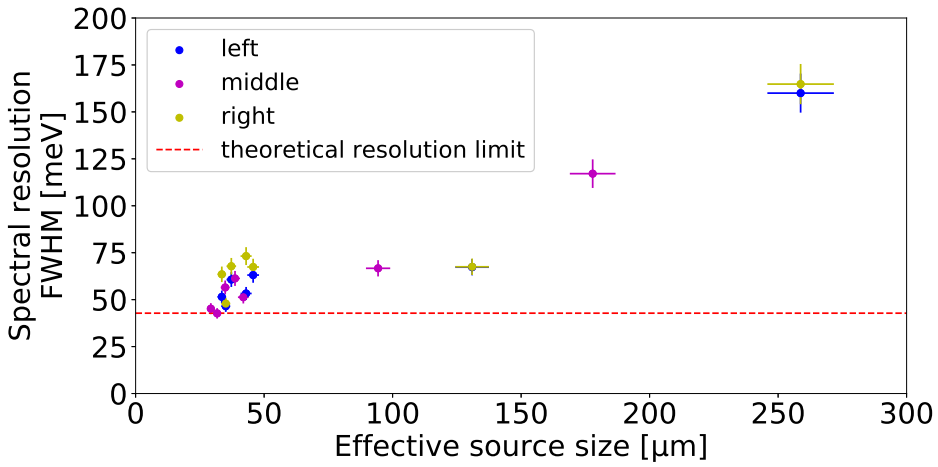

Figure 4.8: Target thickness and x-ray focus width strongly influence the energy resolution of the setup [Equation 4.3], because the analysers collect radiation from a larger area. The outer analysers (yellow and blue) show a lower resolution due to this source broadening. The resolution here is given as the FWHM of a pseudo-Voigt fit of the data. A theoretical limit of 42.8 meV is given to the resolution from the convolution of the Darwin widths of the monochromator and analyser crystals (dotted red line). Figure from Wollenweber *et al.* [127]

It was chosen as a compromise to get as much scattering as possible from a thick sample and at the same time keeping the source broadening effects as small as possible. Its surface was parallel to the (010) plane. It was rotated by 4.3° to hit the analysers at 8° along the (001) direction. The diamond was mounted to a resistive heater to accurately define and apply a constant temperature. As the 500 K chosen for the heated spectra is above the melting point of PMMA, amorphous 250 $\mu m SiO_2$ was used instead to determine the instrument function (Fig. 4.9). The set temperature on the resistive heater was measured to be $503\,K \pm 8\,K$ with a type K thermocouple (Accuglass).

The spectra obtained from the diamond clearly resolve two distinct peaks left and right from the elastic line. An eventual quasielastic contribution from impurities or defects within the crystal is not visible. It is either absent or weaker than the blue shifted photon peak. For the heated case, the blue-shifted peak becomes more distinct and the amplitude ratio of Stokes and anti-Stokes line shrinks (Fig. 4.10).

The intensity distribution scattered from the diamond can be fitted with the instrument function convoluted with sum of three Lorentzian peaks, accounting for red- and blue-shifted as well as quasielastic scattering. Leaving amplitude, width, and position of the contributing Lorentzians as free parameters, the resulting fits for all three analysers in both the hot and the cold case obtain a temperature from detailed balance that agrees with the set temperatures within the error bar, the largest difference being 8 %. The obtained phonon energies agree well with literature values [152, 156–158].

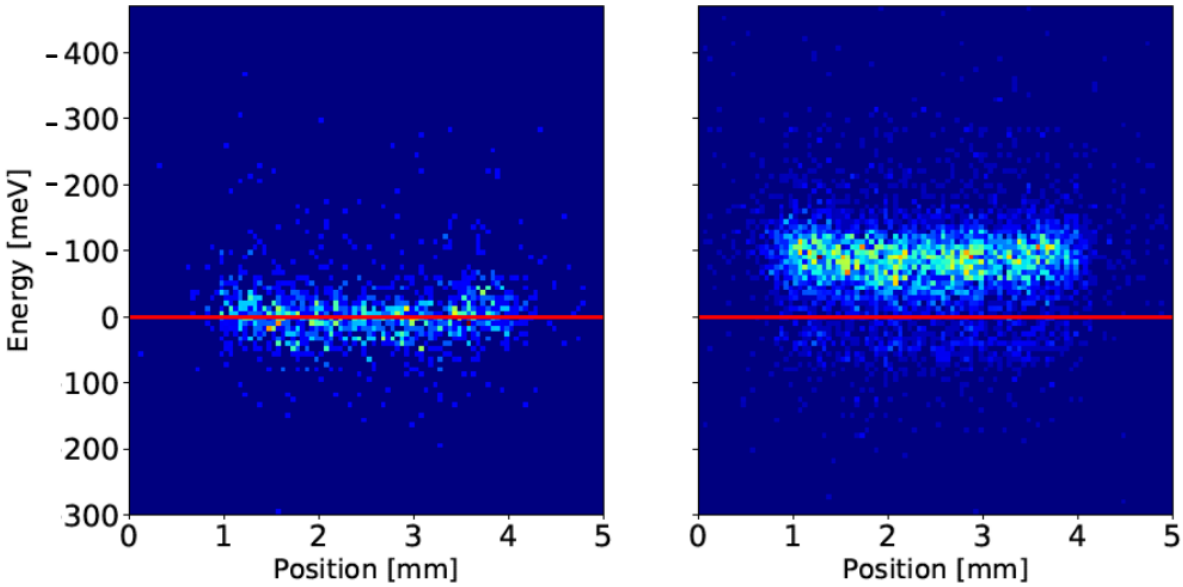

Figure 4.9: Comparison of the quasi-elastic scattering from an amorphous material (SiO_2, left) and a single crystal (diamond, right). The quasielastic scattering from the SiO_2 is centred around the elastic line (red) at zero energy transfer. The diamond shows no scattering here. Instead, an intense line of red shifted photons and a weaker line of blue shifted phonons are visible.

4.1.3 Summary

In this experiment we demonstrated the capabilities of the IXS platform at HED. For thin samples of 50 μm thickness or less near-theoretical resolution could be reached from quasielastically scattering samples. For thicker samples source broadening starts to play a role, as expected. A 10 Hz operation at the rate of the bunch trains at EuXFEL poses no problems, while multiple bunches per train do not contribute to the signal due to the x-ray induced heating and consequent loss of transmission in the channel cut monochromator. We further demonstrated that the setup can resolve phonons in single crystal diamond. These measurements could be used to accurately determine the temperature of the diamond via detailed balance of the Stokes and anti-Stokes lines at room temperature and at 500 K, set by a static resistive heater.

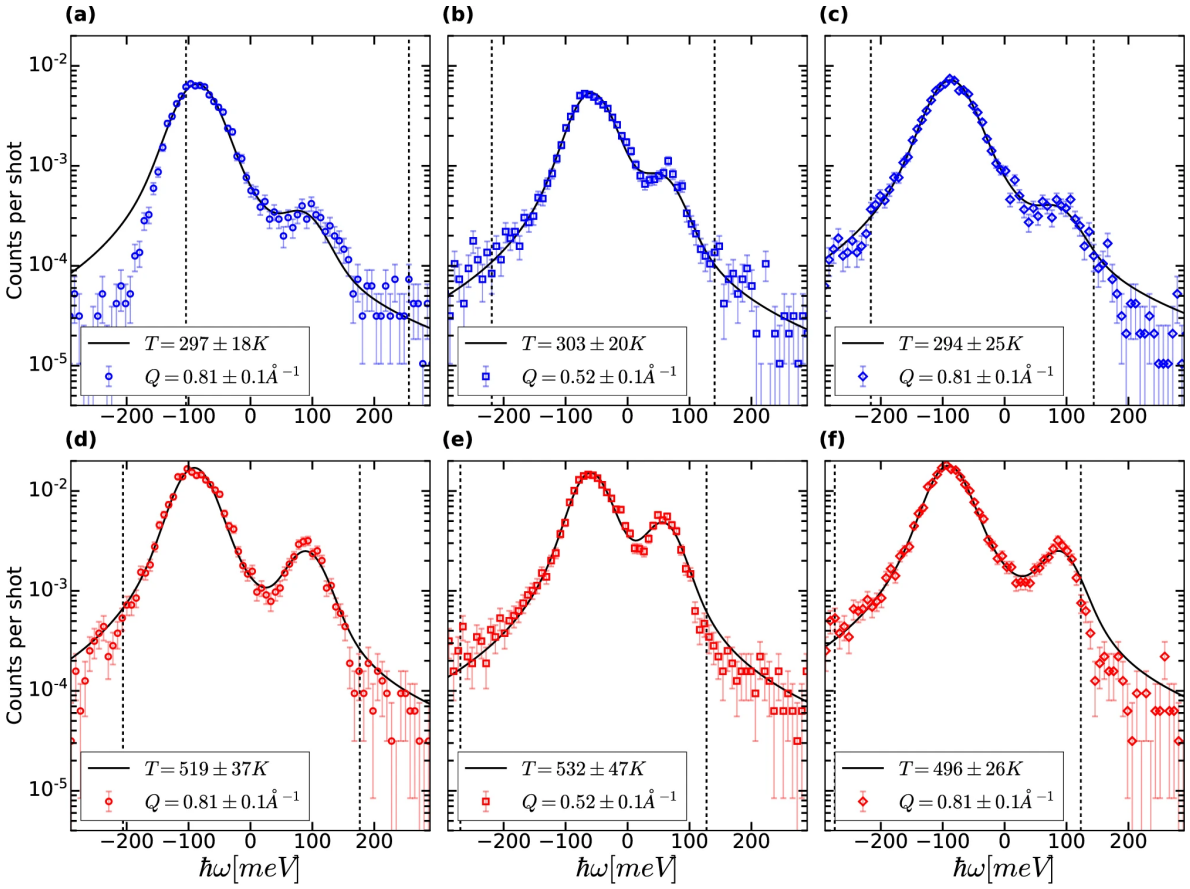

Figure 4.10: Top: cold diamond spectra for all three analysers. The two peaks for blue- and red-shifted photons are clearly resolved in the data points (blue). The fit (black) to determine the temperature was obtained from data points between the dashed vertical lines. These lines correspond to the edge positions of the SASE square. Bottom: Same as top. For the heated data points (red), the blue-shifted peak becomes more pronounced as the phonon occupation within the crystal rises. In both cases the measured temperature agrees with the set temperature within the error bars. Figure from Descamps et al. [152].

4.2 Transient Phenomena: Shocked Pulsed laser-heating of Iron

The next step after having demonstrated the static temperature measurement shown in the last chapter 4.1 is to transfer the measurement method to dynamically driven matter and the choice of a scientifically relevant target material. This was proposed in the HED proposal 2656, titled 'The transient response of solids under impulsive excitation'. As the scientific case of the proposal was split into an x-ray only and a part which uses an optical laser drive, I will concentrate here on the laser part of the experiment, as it was my main focus. The organisation of the x-ray only part was mainly done by Oliver Karnbach and the results are summarised in his PhD thesis [159]. My contributions to the experiment, of which I was the main proposer, were the following: Before the experiment, I was actively involved in the planning of the experiment and performed simulations to judge the feasibility. I worked on the mechanical setup of the x-ray diagnostic and optical setup inside the target chamber. I helped with the beam transport and characterization of the 1030 nm pp-laser, which had not been used before at HED. During the experiment, I worked shifts in the control room and performed work on the beamline as well as online analysis. After the experiment, I analysed the data.

4.2.1 Setup

The basic x-ray setup for this experiment is similar to the previously described setup for the spectrometer calibration (see chapter 4.1.1). However, since this new experiment aims to measure the temperature in a dynamically excited sample, a drive laser needs to be added to the setup.

The aim of the proposal was to increase the temperature, density and pressure of an iron sample by a shock wave. In order to drive a shock wave with a laser into a solid, a high energy laser pulse is required (see 2.1.2). Though, at the time of this experiment the dedicated laser at HED for this kind of experiments, the 100 J-class DiPOLE-100X nanosecond laser system [105, 160], was not yet operational. Instead, the 1030 nm stage of the SASE2 pump-probe laser [138] was the only laser with comparably long pulses and significant pulse energy available. Unfortunately, this laser is only able to deliver 40 mJ pulses of roughly 400 ps length, whereas ideally these type of shock wave experiments require up to 100 J with ns pulses, provided from May 2023 by the DiPOLE-100X laser.

To judge whether the much weaker pp-laser system would still be able to drive the samples into an scientifically relevant state, and if the induced transient changes would be detectable with the existing Si (533) x-ray diagnostics, I performed simulations with the MULTI hydrodynamics code [161]. The thickness of the iron foil was chosen to be 3.5 μm. This thickness corresponds to the photo-absorption length of iron at 7.5 keV photon energy and therefore provides the highest scattering signal, as it balances photo-absorption of the incoming photons and re-absorption of the scattered photons. The simulations used the equations-of-state (EOS) from the SESAME database (Los Alamos National Laboratory). Additionally, I made the assumption that about half of the initial laser pulse energy will be lost during its beam transport, so that only 20 mJ will impinge on the target.

Repeated measurements performed during the pp-laser setup yielded 27 mJ at focus position, which validated the assumption as reasonable.

Multiple simulations for different focal sizes were done, ranging from 10 μm fwhm to 50 μm, resulting in different laser intensities. For the final experiment, I opted to go for a 25 μm full-width-at-half-maximum (FWHM) focal spot, as the simulations predict that we would reach a reasonably high pressure and temperature state under these conditions (see Fig. 4.11) and at the same time would be easier to technically achieve within the given time constraint. It is also spatially large enough to provide some leeway concerning spatial overlap with the x-ray beam. Our goal was to follow the temporal evolution around 400 ps after the end of the laser pulse, where the simulation predicts an almost steady state over the complete length of the target except the ablation plasma (0.8 ps, light blue line in Fig. 4.11). This way, the scattered signal should mostly originate from a narrow temperature region, as the ablation plasma has a much lower density than the bulk target and thus contributes less to the signal.

The x-ray setup of the experiment inside the target chamber is similar to the one used in the previous section (Fig. 4.1). The DCAs are mounted to the vertical rails and form together with a detector above the sample a Rowland circle of 1 m diameter. The scattering angle of the DCAs was set to 23°, corresponding to a momentum transfer of $q = 1.52\,\text{Å}^{-1}$. X-ray area detectors downstream of the sample were used to collect additional diffraction data, which informs about the crystallographic structure, density, and potential melting of the sample. Before the sample, a HAPG von-Hamos spectrometer [162] was mounted in backscattering geometry, which was mainly used in the x-ray only part of the experiment. Instead of the ePix100 detectors used in the previous experiment, this experiment used only Jungfrau detectors for all x-ray diagnostics. The laser was focused onto the sample with an angle of ca. 10° to the x-ray axis with a lens of 750 mm focal distance (Fig. 4.12 , 4.13), resulting in a measured spot size of $\sim 22\,\mu m$ FWHM.

Contrary to the previous chapter, this experiment did not use SASE beam, instead the FEL was operated in self-seeded mode. Though the total number of photons is lower in this operation mode, due to the higher spectral density more photons should be transmitted over the monochromators, leading to a higher total scattering signal. The x-rays were focused down with the CRLs in the HED optics hutch to a size of $\sim 15\,\mu$m fwhm. Unfortunately, there was a problem with the Si (111) pre-monochromator at the time of the experiment: The cryogenic cooling of the crystal, meant to thermally stabilize the crystal under x-ray heat load, lead to an oscillating movement of the crystal and as a consequence a moving x-ray beam along both the horizontal and vertical axes (Fig. 4.14). This movement of the beam on the order of several hundred μm would have made it impossible to achieve spatial overlap between x-rays and laser at the focus point. This meant that we were unable to use the four-bounce monochromator scheme introduced in the last chapter and needed to improvise. As a solution, we angled the x-ray beam upwards with the last turning mirror of the beamline 460 m in front of the monochromators to directly go over the Si (533) high-resolution monochromator. This action lead to a vertical offset of several mm at the sample position between the x-ray beam with and without monochromator.

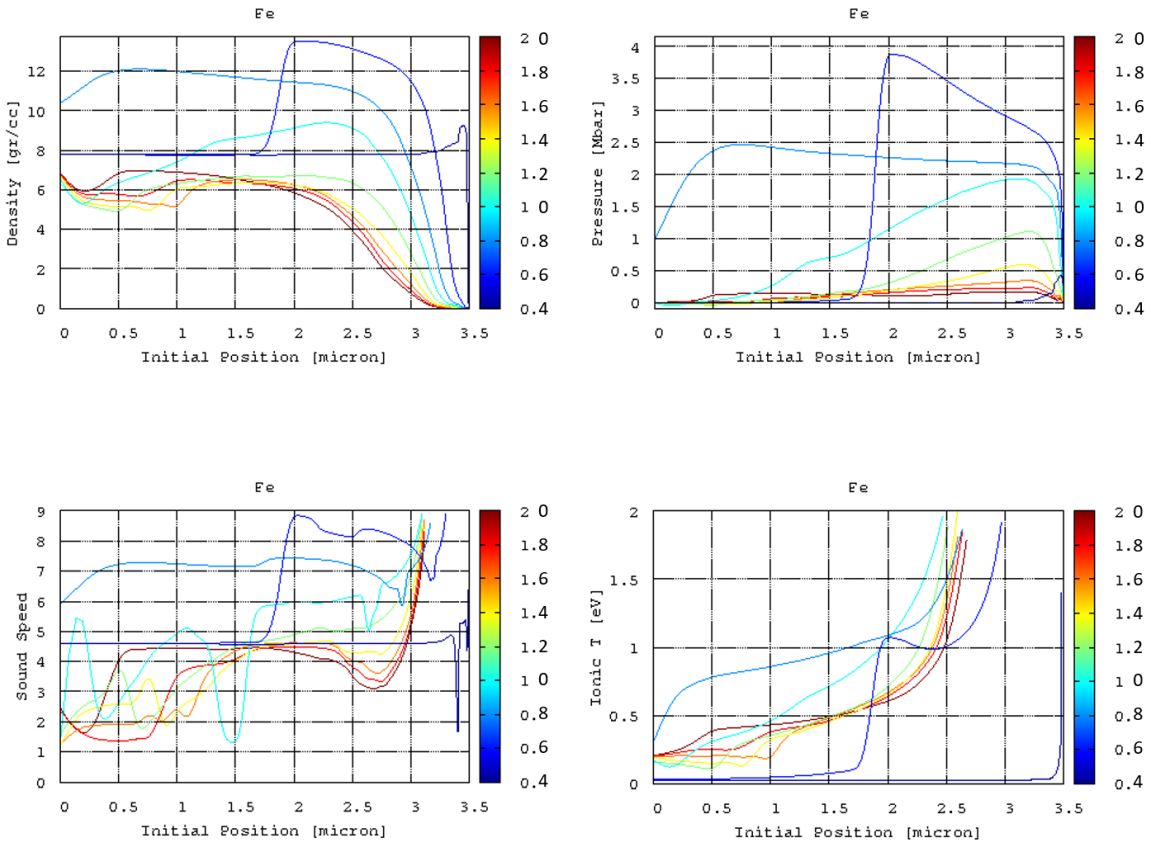

Figure 4.11: MULTI simulation of the pp-laser interaction with a 3.5 μm iron foil. The simulation assumes 20 mJ of laser energy impinging on the target within a 400 ps pulse with a Gaussian profile focused to a 25 μm fwhm spot. The colour scale on the right side of all graphs gives the time of the simulation in 200 ps steps. The x-axes indicate the position inside the foil, with the laser coming in from the right side. The y-axes on the left show the respective scales for the simulation parameters. Top left: mass density, top right: pressure, bottom left: sound speed and bottom right: ion temperature.

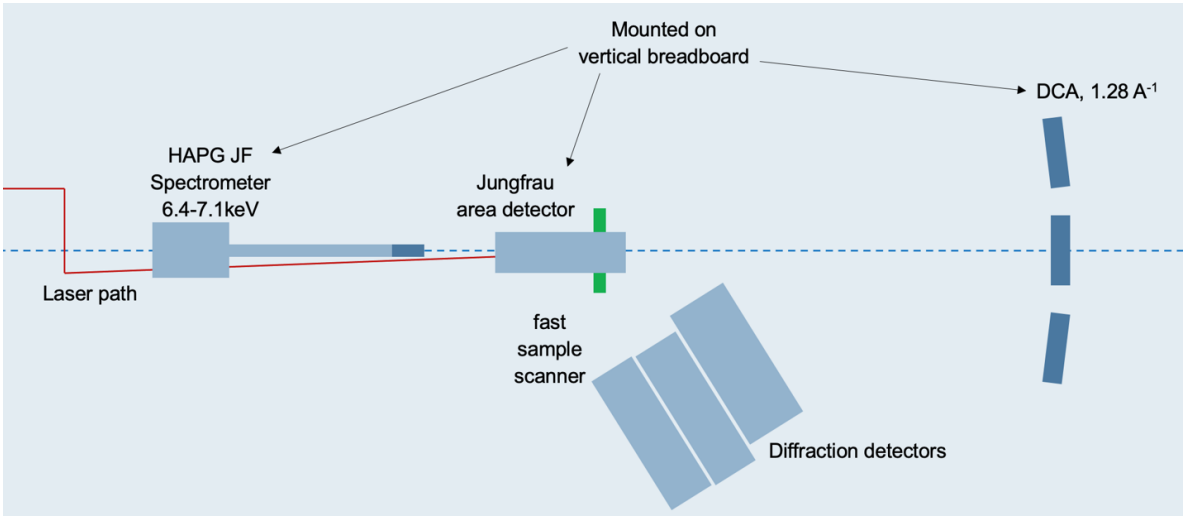

Figure 4.12: Schematic view of the experimental setup inside the vacuum chamber. The x-ray beam is depicted by the dotted blue line and enters from the left side. The laser path is shown in red. In the centre of the chamber is the sample scanner with the target frame (green box). Above the target sits the detector for the DCAs, which are situated 1 m after the sample at a scattering angle of 23°. Multiple detectors are mounted behind the sample at beam height to capture diffraction signals. Upstream of the sample is a HAPG backward scattering spectrometer mainly used in the x-ray only part of the experiment.

The pulse energy of the seeded beam, including the SASE pedestal, was around 200 μJ.

Due to these challenges during alignment, an additional unscheduled downtime of the accelerator and necessary time for the tuning of self-seeding, we eventually acquired a significant delay in the actual data taking. Additionally, we settled at a 2‰ higher photon energy than planned, 7501 eV instead of 7490 eV. This energy was measured by the HAPG-spectrometer, which is absolutely calibrated with emission lines. This small deviation, unrecognized during the experiment and only discovered during the subsequent data analysis, lead to a substantial change in the energy dispersion on the detector: According the dispersion equation Eq. 2.98, the resulting dispersion was now 0.244 meV/μm, about 60% larger than the 0.15 meV/μm in the diamond experiment.

Unfortunately, there exists no dedicated tool to measure the pulse-to-pulse arrival time between x-rays and the 1030 nm pump-probe laser. Instead, we used a photo diode connected to an oscilloscope to look at the optical transmission of the widened laser beam through a YAG crystal. Due to the x-ray induced opacity change, the optical transmission drops if both pulses arrive at the same time. As the signal-to-noise ratio was atrocious, we had to average the diode signal over 100 shots. This way, we defined 'time zero' at the point where the x-rays arrive at the theoretical laser intensity maximum. The laser experts on shift judged this method to have a precision no better than 400 ps. We managed to measure IXS spectra at two time delays, 300 and 450 ps after

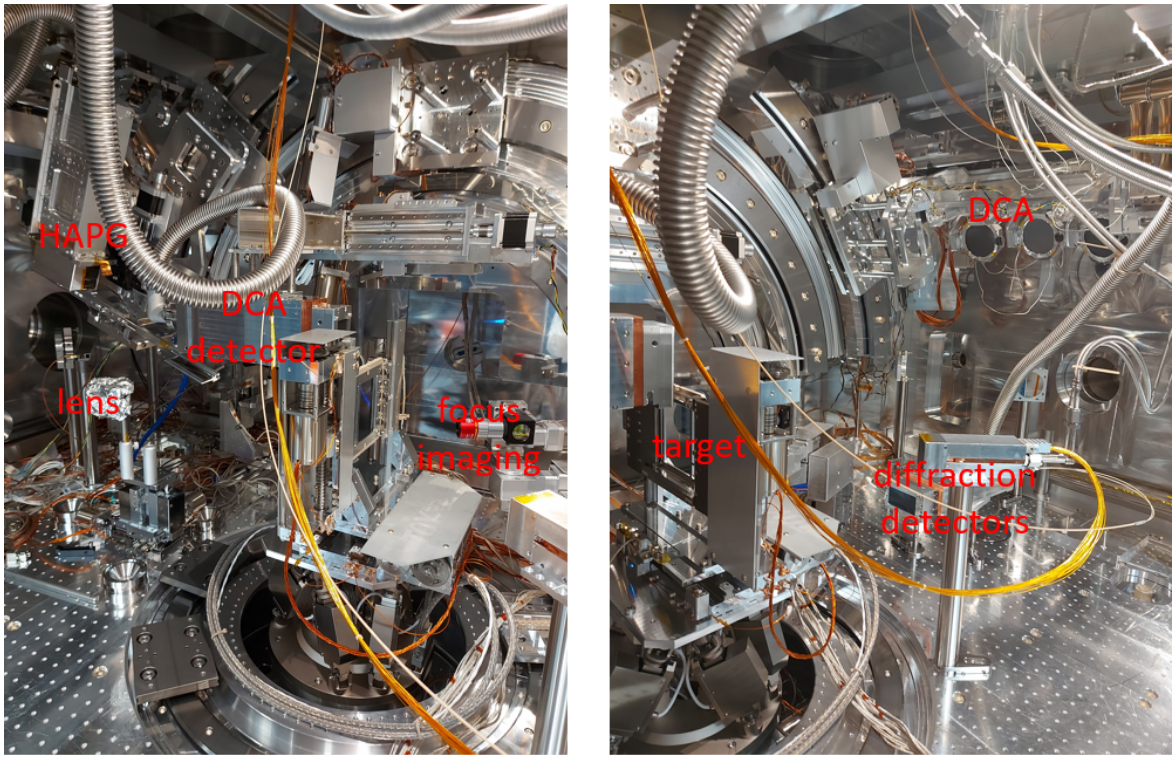

Figure 4.13: Photos of the IC1 vacuum chamber with the setup for experiment 2656. In the centre of the chamber is the sample scanner (labelled in the right image), which holds the target frames. Above and slightly upstream of the target is the detector for the DCAs. Below this detector sits the crystal for the HAPG spectrometer, its detector sits below the ceiling (labelled on the left). Located on the downstream side of the target are the DCAs, as well as detectors for diffraction (right photo). The focusing lens for the optical laser is covered by aluminium foil upstream of the target. The objective downstream of the target is for focus imaging (left photo).

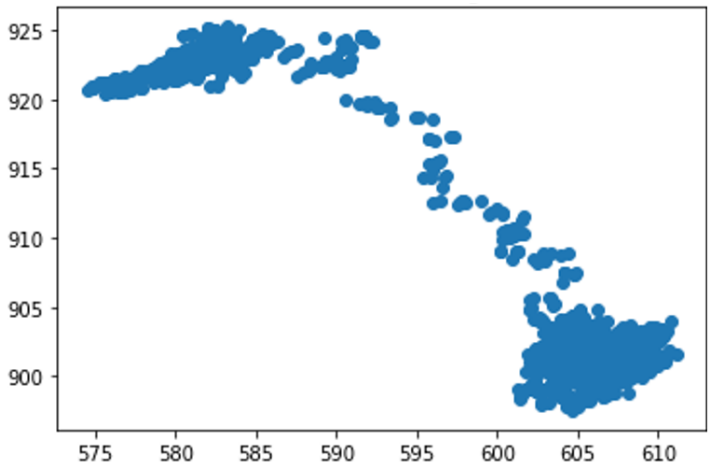

Figure 4.14: Beam pointing jitter introduced by monochromator. The points show the centre of mass of the x-ray beam on a YAG screen at the end of the SASE2 tunnel after passing through the Si (111) monochromator. Beam jitter due to the cryogenic cooling is clearly visible. The pixel differences of 25 horizontal and 23 vertical correspond to 0.55 mm and 0.7 mm movements.

the laser maximum, which were selected based on the hydrodynamics simulations.

The sample foils were bought from Goodfellow Cambridge Ltd. (304-839-07) and had a size of 50×50 mm at a thickness of $4\,\mu m$, which is close to the absorption length of iron at 7.5 keV and therefore the ideal choice for balancing the scattering signal against photo absorption. Also, for samples this thin, source broadening is negligible, as shown in the previous section, and the resolution is solely determined by the spectrometer resolution and the incident x-ray bandwidth. As we would need several hundred shots to obtain a sufficient amount of photons for a spectrum at each time delay, we chose a supporting frame with large windows to enable so called fly scans. Fly scans enable fast scans of the target while maintaining sufficient space between laser shots to not hit already excited material again without constant manual adjustments. For these scans, the x-ray beam starts blocked by a fast pulse picker. Then the sample motor starts accelerating up to a certain speed. When the motor is in constant motion, the pulse picker opens up and x-rays and laser start hitting the sample at a rate of 10 Hz. Before the motor decelerates at the end of a row, the x-rays are blocked again and the laser switched off. The motor stops, changes row and can directly start the next series in opposite direction. The foils were glued to frames, which could be inserted in the HED fast sample scanner, with an organic polymer adhesive (nail polish) (Fig. 4.15).

4.2.2 Results

As mentioned, the accidentally 2‰ higher photon energy in this experiment results in a higher dispersion and thus, a lower energy resolution. We measured a FWHM value of ~ 100 meV from a $50\,\mu$m PMMA sample,

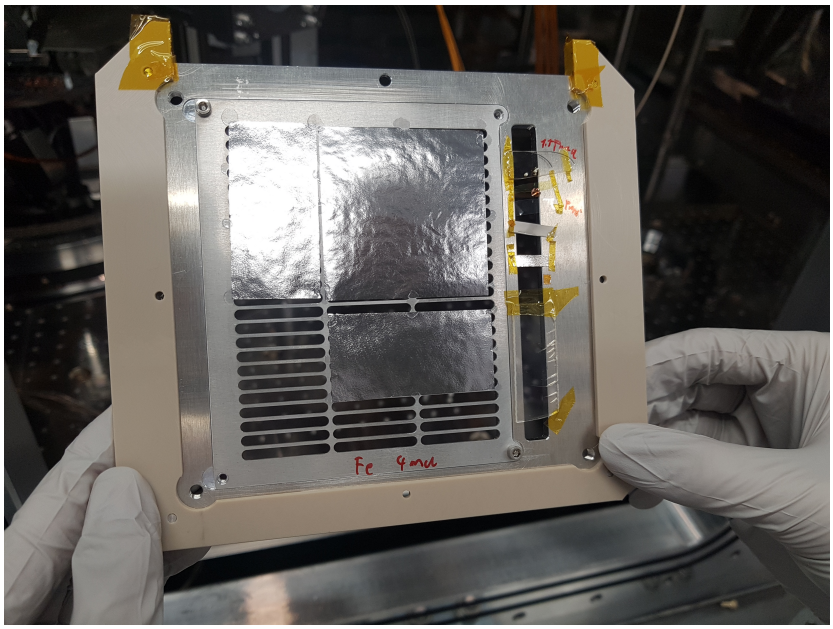

Figure 4.15: Frame for the sample scanner with 4 μm iron foil targets. The strip on the right side holds a number of calibration targets for diffraction and elastic scattering.

which is more than twice worse than previously obtained. A resolution of about 75 meV can be explained by the higher dispersion and thus, a worse resolution per pixel. The remaining 25 meV most likely result from defocusing of the analysers and detector by not placing both accurately in Rowland circle geometry. A distance mismatch of only 1.3 mm is already sufficient to explain the discrepancy with spreading from a point focus. All other contributing factors to the instrument function like the intrinsic crystal resolution, Johann-error, and source broadening are negligible.

With this resolution it is impossible to accurately measure phonons, as there is no discrete separation of the phonon peaks from the quasielastic scattering. This is a large problem, as the samples were polycrystalline foils, not single crystals without quasielastic contribution to the scattering like the diamond in the proof-of-principle experiment. It can be seen for a room temperature iron spectrum (Fig. 4.16) of the central analyser, that a certain asymmetry towards the red-shifted photon side exists. Each contributing factor can be fitted with a Voigt-profile, Stokes and anti-Stokes lines, as well as the quasielastic scattering to form in sum the measured spectrum. As quasielastic and inelastic scattering are not clearly distinguishable, it becomes difficult to constrain the individual profiles. To ease the task by reducing the free parameters, I set the width of all three Voigt profiles equal to the width of the elastic scattering from the PMMA, as the instrument function is the minimum achievable resolution and all features of the spectrum are naturally narrower.

Without further constraints, the temperature from detailed balance from several cold iron spectra we took throughout the beamtime comes out to be on average $392\,K \pm 24\,K$ with a mean phonon energy of $44.5\,meV \pm$

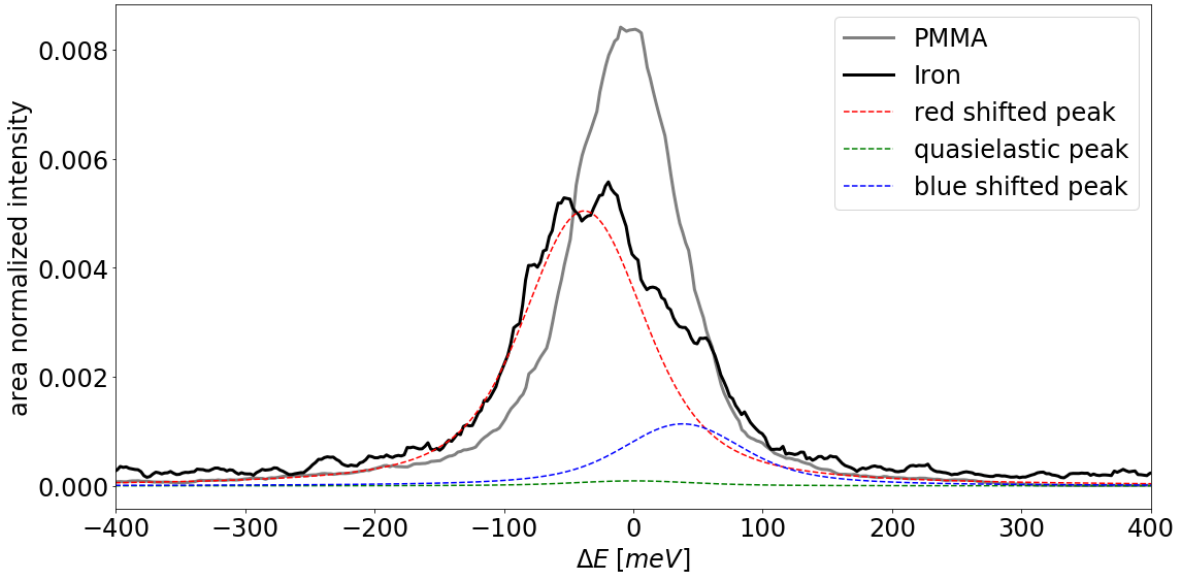

Figure 4.16: Area normalized spectra of room temperature PMMA and iron from the central analyser. The PMMA (grey) shows only quasielastic scattering symmetric around the incident photon energy. In contrast, the iron spectrum (black) exhibits a clear shift to the side of the red-shifted photons, indicating the presence of phonons, which are located at around 38 meV. The coloured lines are the result of a fit to show possible contributions of the red- and blue-shifted parts as well as the quasielastic scattering. The fine structure of the peaks results as an artifact from the sub-pixel shifting routine used to correct the curvature of the scattered signal.

$3.5\,meV$. As no phonons can exist above the Debye-frequency, I fixed the the phonon energy, but not the zero position, to 38 meV [163], which yields a slightly lower temperature of $380\,K \pm 27\,K$. I have used the Python library lmfit [155] for all fit tasks in this section. All fits have in common, that they show a very strong inelastic and almost no quasielastic scattering contribution. As the samples were no single crystals, but some *off-the-shelf* polycrystalline foils, we expected a significant quasielastic contribution. The inability to see this in the best fits results most likely from the bad resolution. All fits show an almost one-to-one correlation between the amplitude of the inelastic and quasielastic features. The presence of homogeneous rings in the diffraction data and absence of isolated Bragg spots is a clear indication for a polycrystalline sample with many small crystals in the x-ray focus.

From the diffraction data it became also clear, that we were unable to compress our samples at the chosen delay times (Fig 4.17). I have used the program Dioptas [164] for the angle calibration with a CeO_2 diffraction standard. Both 110 diffraction lines are slightly shifted to about 0.1° lower Bragg angles, which indicates a longer bond distance. This change corresponds to a density of around 7.78 g/cm^3, which indicates a temperature around 600 K [165, 166]. Under compression, it should naturally become shorter. The observed behaviour

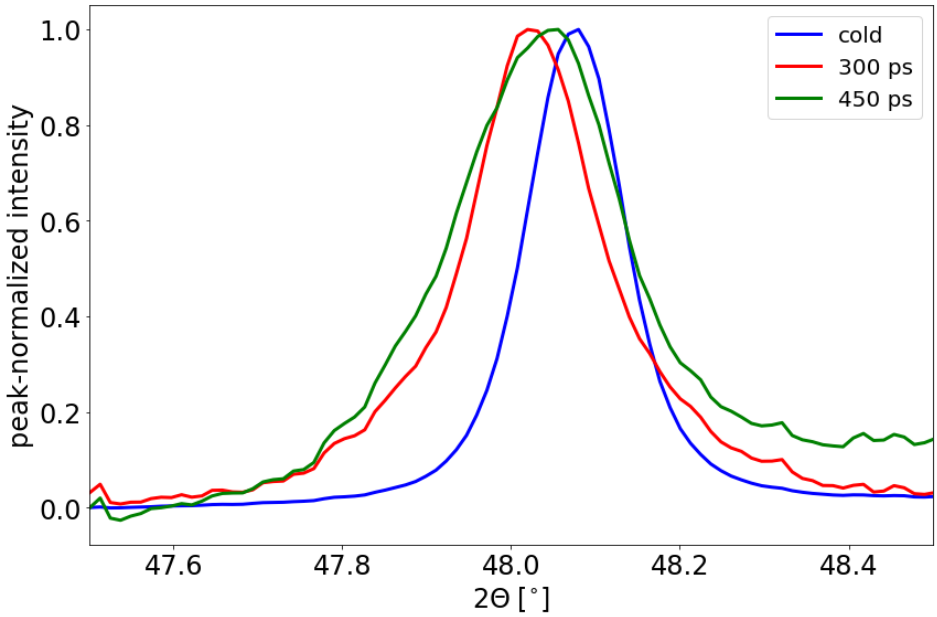

Figure 4.17: Peak-normalized diffraction data from ambient (blue) and excited (red and green) iron from the 110 reflection. Contrary to expectations, the excited peaks are slightly shifted to lower Bragg angles, indicating only heating, whereas compression of the material would have shifted to higher angles.

results most likely from a slight expansion due to laser heating. This is also visible in the fact, that the excited peaks posses a lower photon count and higher diffuse background, which is explained by the Debye-Waller effect. As the diffraction lines are still visible and no liquid diffraction is observed, the iron sample was not molten in the volume that was probed by the x-ray pulse at the two measured time delays.

There are two likely reasons we didn't see any compression. First, it could be that the timing procedure between x-ray and optical laser wasn't accurate enough and our measurement took place (at least for some of the acquired data sets) after shock breakout in already heated and expanding matter. Second, that the homogeneously compressed state predicted by the 1D MULTI simulation simply doesn't exist in the real world. To crosscheck the simulation results, my colleague Victorien Bouffetier set up new simulations with the FLASH code [167–170], in a two-dimensional geometry which can give insights into spatial variations of the shock wave. These simulations show a behaviour not captured by the 1D code: While similar peak pressures are reached, this is only the case for centre of the laser spot. The shock dissipates energy to the lateral sides within the same time span it needs to travel through the foils thickness. Due to the small focus needed to reach the peak pressure and the Gaussian shape of the beam, the pressure drops towards the sides is steep. With a beam jitter of the order of half the x-ray focus spot diameter, which unfortunately regularly occurred at HED, the probed pressure roughly halves. An additional factor is spatial and temporal misalignment between laser and x-rays due to drifts while raster-scanning the targets. Most likely, all these factors contributed, and as a result we did

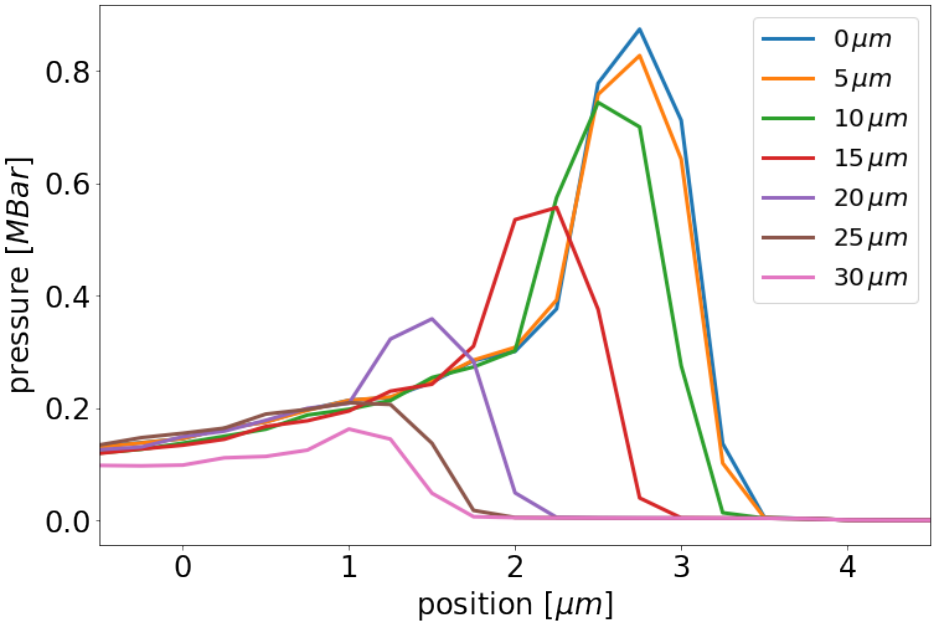

Figure 4.18: 2D simulation for the pressure distribution with the FLASH code at 500 ps delay with the same parameters as the 1d simulation (Fig. 4.11). The laser comes from the left side. Lineouts were taken at $5\,\mu m$ steps from the centre of the laser spot. Peak pressure and progression of the shock wave rapidly decline towards the sides due to the small Gaussian focus spot of the laser.

not detect the expected compressed states.

As I had to sum all runs from the delayed shots to get a reasonable signal for the diffraction, spatial misalignment seems a good explanation for location and shape of the 450 ps peak in the diffraction data (Fig. 4.17), which lies between the 300 ps and the cold peak and is wider than both, a sum of different hot and cold states. During the experiment we observed a rapid decline of the signal during the 450 ps scans on the online preview in run 293, after which we redid the spatial alignment procedure. A closer analysis of the scans revealed a systematic error to our measurements. During the fly scans, the position of the foil changes along the x-ray axis (Fig. 4.19). This has a profound effect on the scattering signal, as these shifts translate to a one-to-one shift along the energy axis. If approximated with a single Gaussian, the signal shifts almost linearly with the vertical motor position. A linear fit yields a slope of $2.5\,\mu m/mm$ height change, indicating a 0.14° tilt of the target frame within its holder (or of the foil relative to the target frame). This means, that all shots from a single 3 mm high target window can be added together without broadening the spectra too much, however several windows could be added together only after applying a correction factor. Much more important is the fact that this shift applies to the spatial overlap between x-rays and optical laser, too. It doesn't affect the power distribution within the laser pulse that much, as the shifts are well below the Rayleigh length of 1.5/mm. Instead, the important fact is that x-rays and laser are not propagating co-linearly but at an angle of $\sim 10^\circ$. Changing from one window to

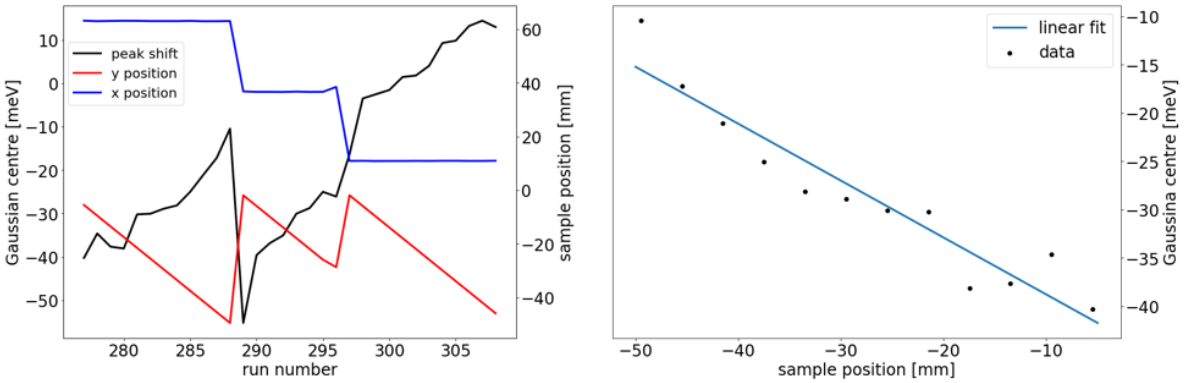

Figure 4.19: Investigation of the effect of the fly scans on the measurement. Left: the position of the central analyser signal on the detector changes for each DAQ run, which correspond to a single window on the target frame (black line, left axis). The red line indicate the position of the motor which shifts the target frame vertically and the blue line gives the horizontal shift (both right axis). Right: Correlation between vertical target position change and shift of the scattering signal for the first x-value.

the next offsets the centres of laser and x-ray focus by more than 10 % of the x-ray focus diameter. This means that each target window provided a different ensemble of states for the x-rays to probe, even without accounting for beam jitter. Over the duration of the scans, this shifted the overlap from the well aligned centres to probing almost cold material.

The diffraction data gives some information about what to expect from the inelastic scattering spectra. First, we observe that the iron is heated but not molten. This implies, that the intensity ratio of red- and blue-shifted photons is somewhere between 4.436 at room temperature and 1.276 at irons melting point at 1812 K. Due to Debye-Waller effect, the intensity of the quasielastic scattering should rise with temperature, too. Second, the material is not compressed but on the contrary ever so slightly expanded, so the phonon energies should be at around the same position as for the cold material, and not further out as one would expect in a compressed state with higher speed of sound.

This is indeed what we observe in the measured excited spectra. All loose the asymmetry present in the cold spectra while preserving similar widths at the base. Of course, the inability to separate inelastic and quasielastic features poses an even bigger problem for the symmetric spectra then it was for the asymmetric cold spectra. The symmetry can either be produced by a rising blue shifted or quasielastic feature, as both are a resulted of the heated material. Therefore, minuscule differences in shape strongly influence the fits necessary to obtain an accurate temperature (Fig. 4.20).

Using detailed balance becomes imprecise for higher temperatures, as the changes of the intensity ratio between the red- and blue-shifted feature become increasingly smaller: Whereas the ratio changes by a factor of 3.16 for the 1500 K jump from room temperature to melting point, the jump to 3300 K only changes the ratio

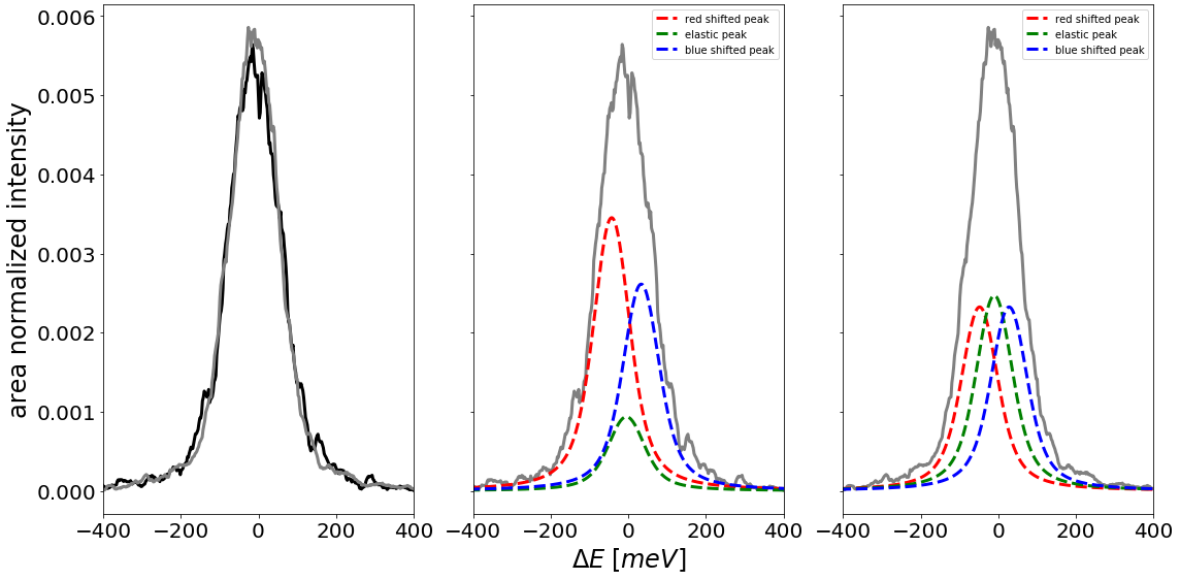

Figure 4.20: Two apparently similar excited spectra (left) come to a very different result with the same fitting procedure (middle, right) due to a lack of constraints on the ratio of quasielastic to inelastic scattering.

by 0.13. Keeping widths and phonon restrictions the same as for the cold data fits, the mean temperatures come out to be $6000\,K \pm 3300\,K$ for the 300 ps delay and $5800\,K \pm 5000\,K$ for 450 ps delay. These values exclude the roughly 50 % of data points, where the amplitude ratio of the best fit comes out to be an even one, indicating a unrealistically high temperature. Introducing an additional constraint by fitting all three analysers to a single intensity ratio within one run (a reasonable assumption as they should all measure the same temperature) doesn't change these numbers in a noticeable way.

In the IXS spectra we could see a clear asymmetry for cold iron, which is not present for the laser-heated shots. It is quite pronounced in the upper part of the spectrum, produced by the absence of blue shifted and lower levels of quasielastic photons. The average width at 70 % peak height changes from 78 meV ±12 meV in the cold iron to $113\,meV \pm 7\,meV$ (300 ps) or $106\,meV \pm 4\,meV$ (450 ps) in the heated material. This is a change of 45 % at 300 ps delay (35 % at 450 ps). In comparison the difference at the base (20 % peak height) is only 12 % for 300 ps delay and 5 % for 450 ps (Fig. 4.21).

Also, the heated spectra posses a higher number of photons per shot due to the increased diffuse scattering from the Debye-Waller effect. In later runs at 450 ps delay the number of photons per shot decreases due to the runoff in spatial overlap and approaches the level of the cold iron.

Because of these two effects we can conclude that we indeed observe transient laser-heated iron in our IXS signal, but we can't reasonably extract a temperature value via detailed balance. This IXS data is in agreement with x-ray diffraction which suggests a temperature below the melting point.

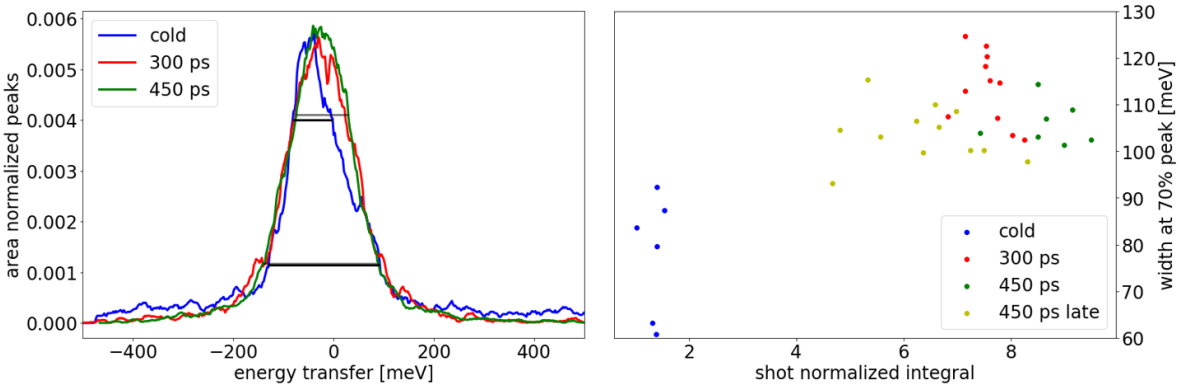

Figure 4.21: Left: comparison of a cold spectrum (blue) with heated ones at 300 ps (blue) and 450 ps (green) delay. Widths are roughly the same at the base but differ higher on the peak. Right: width at 70 % peak maximum versus the shot normalized photons in a spectrum. The excited spectra have a higher photon count than the cold spectra and are wider at the top of the peak. Both observations are indicators for a higher temperature. The late shots (yellow) get increasingly closer to the cold data due to loss of spatial overlap.

4.2.3 Summary

We performed an experiment on laser-excited iron in which we accomplished several goals which go beyond the achievements during the earlier diamond proof-of-principle experiment:

- we operated the setup in self-seeding mode rather than SASE which improves the amount of photons on the sample
- we replaced single crystal diamond by a thin polycrystalline Fe foil which is a material of higher scientific relevance
- we excited iron with a pulsed laser rather than heating it with a static heater which requires spatial and temporal overlap
- we raster-scanned several 1000 destructive exposures on individual samples rather than collecting data from one static sample position, which required sample preparation and specific motion control and triggering
- we fielded x-ray diffraction as additional diagnostic, which required mechanical setup and calibration

This added complexity in this first pump-probe experiment resulted also in a few setbacks:

- the spectral resolution was not sufficient for an accurate temperature measurement via detailed balance, due to a multitude of technical challenges with the experimental setup. The lack of a clear separation of the

quasielastic line and the inelastic scattering introduces too much arbitrariness for meaningful temperature measurement.

- we were unable to probe the expected laser-driven shock compression of iron. The low laser energy forced us to use a very tight focus, which introduced spatial overlap issues with the x-rays and a highly transient shock wave with strong lateral gradients.
- the mounting of the targets foils and the translation of the foils by the sample scanner motors was not precise enough to maintain overlap between pump and probe when scanning over several centimetres range.
- the very low x-ray photon count after the high-resolution monochromator and absence of dedicated timing tool led to timing errors comparable to the travelling time of the shock wave through the foil, making accurate timing of specific states increasingly difficult.

4.3 Electron - ion equilibration in metals

In contrast to the previously described experiments, the following experiment is not connected to high pressure science with the goal to infer material parameters from temperature and phonon scattering. Instead, the experiments presented in this section are about the interaction of an ultra-short pulse laser with solids. The two experiments in this chapter were conducted at the MEC instrument at LCLS. The first was LV2518 in October 2020, the second one was LY2720 in June 2022. Principal investigators for both experiments were Bob Nagler (SLAC, MEC, Stanford) and Thomas White (University of Nevada, Reno). Both experiments had the same goal of following the ion temperature evolution in a solid in the first few ps after a short pulse laser excitation. Both experiments had almost identical setups and the second one can be seen as a repetition/extension of the first campaign, which became necessary due to some difficulties. For LV2518, I could only participate remotely due to the Covid-19 pandemic and did some online analysis. For LY2720 I participated in all shifts in the control room and did online analysis. Afterwards, I analysed data from both experiments.

4.3.1 Experimental setup

The primary x-ray setup for these two experiments is similar to the previous experiments, with the main difference being that the IXS signal is collected in the non-collective regime (Fig. 4.3.1). This means for a photon energy of 7.492 keV, that the analysers are placed in a backscattering geometry, at a scattering angle of $\sim 170°$. This corresponds to a momentum transfer of $q = 7.56\,\text{Å}^{-1}$.

They are the same crystals which were used in the earlier described experiments, borrowed from the HED group at European XFEL as part of our collaboration. The detector, an ePix100, sits a few centimetres above the target, the same configuration as in the previous experiments. Another difference is, that the monochromator consisted of two channel-cut Si (533) monochromators placed inside the target chamber just 1 m in front of the sample position. The focusing CRLs are just 4 m upstream of the interaction point. They focus the beam down to a size of $\sim 10\,\mu m$ at sample position. This implies that the monochromator crystals are hit by an already focused and quite divergent x-ray beam. Nevertheless, the Si (533) is forgiving enough that no effect on the resolution due to the divergent impinging beam could be observed from the quasi-elastic scattering. But we observed the evolution of x-ray damage on the monochromator crystals during the experiment and had to change spots from time to time. Additional x-ray diagnostics exist in the form of ePix10k [171] behind the sample holder to collect the diffraction signal from the targets. Next, a HAPG von-Hamos type spectrometer [172] was placed in a close to backscattering geometry without cutting into the DCA beam path to collect IXS signal at larger energy transfers to get information on electronic features within the samples. X-ray diodes were employed to measure the intensity of the beam after the monochromators.

For the experiments, the MEC short pulse laser [128, 173] was used. It was frequency doubled by a nonlinear crystal placed within the target chamber to 400 nm and afterwards had a pulse energy of $\sim 1\,mJ$ within

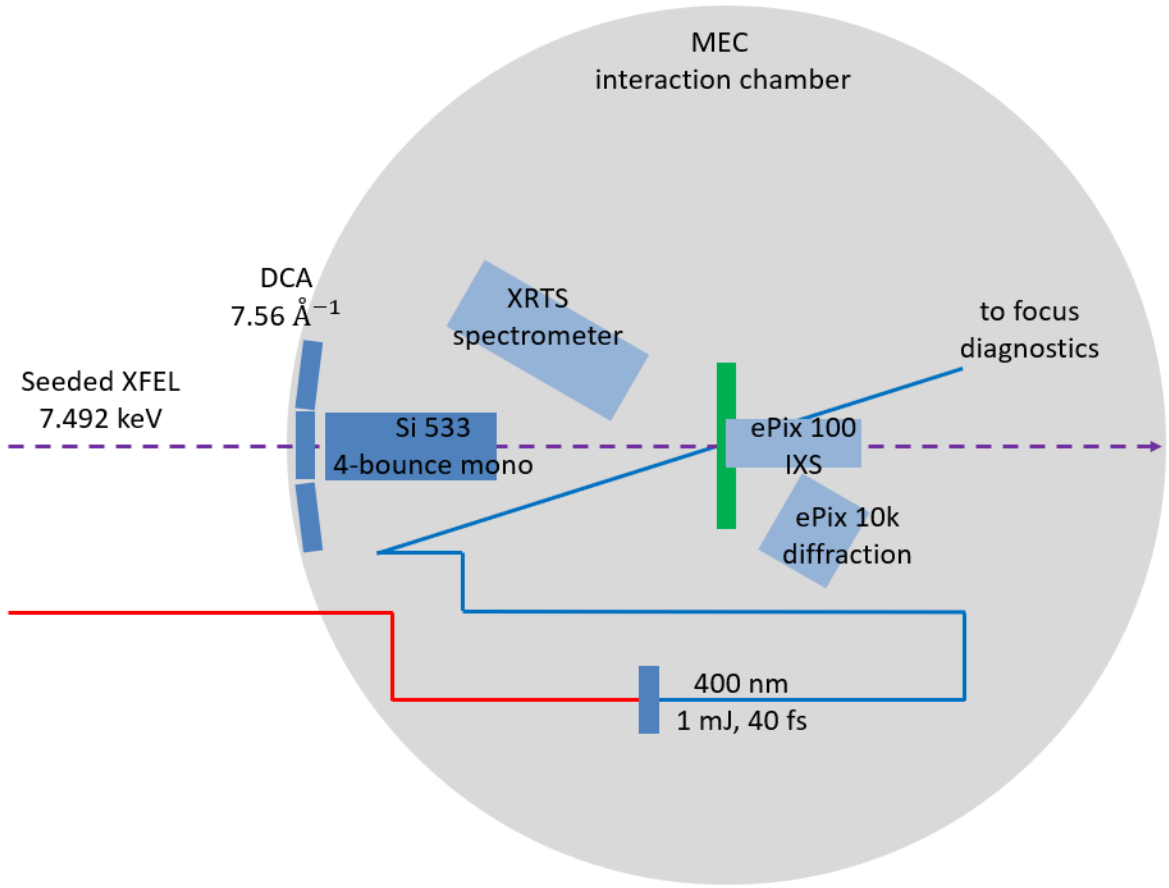

Figure 4.22: Schematic top view of the experimental setup inside the interaction chamber at MEC for the experiments lv2518 and ly2720. The 7.492 keV x-rays enter from the left. Inside the vacuum chamber they pass a 4-bounce Si (533) monochromator before interacting with the target. Three DCAs collect scattered radiation at an angle of $\sim 170^\circ$ and focus it onto an ePix100 detector above the target, forming a Rowland circle geometry. An additional ePix10k area detector sits behind the sample mount to collect diffraction signal. The x-ray Thomson scattering spectrometer (XRTS) was also placed in a backscattering geometry as a diagnostic for electronic features. A 800 nm is guided into the chamber, where it gets frequency doubled to 400 nm. It is then focused onto the sample at an angle of $\sim 10^\circ$ to the x-ray beam.

Figure 4.23: Sample holder for LY2720. On the left side is a collection of alignment and calibration targets. The three centre samples contain 50 nm thin copper targets on a $360 \times 360\,\mu$m nickel grid. The frame on the right side is an already shot gold foil target.

a duration of $\sim 40\,fs$. It was focused onto the sample at an angle of $\sim 10^{\circ}$ relative to the x-rays. The optical leakage behind the sample was used to diagnose pulse energies and image the focus spot for each individual shot. The focus size was on the order of $100\,\mu m$ FWHM, slightly changing with the laser pulse energy. The energy within the focus could be adjusted via the pump-laser energy and an iris. An absolutely calibrated equivalent-plane monitor was used to determine the laser pulse energy. The timing between x-rays and the optical laser was monitored with the MEC timing tool and semi-regularly checked at the sample position. The accuracy of the timing obtained from the timing tool, with the addition of some leeway to account for differences at the interaction point and the timing tool, comes out to be $\pm 300\,fs$.

The samples were planar metal foils of only 50 nm thickness produced by Luxel. They had an area of roughly $4 \times 4\,cm$ and were supported by a square nickel grid with a side length of $320\,\mu m$ (Fig 4.23), the nickel wires possessing a diameter of $40\,\mu m$. We used targets made out of gold, silver, titanium, and copper. To get a reasonable data rate of 1 Hz, we used a fly scan to raster the sample grids. As the synchronization was not precise enough, we decided to limit this kind of scans to two lines at once before realigning to the nickel grid. During the experiment, we took time delay series for gold at two different laser fluence levels, silver, titanium, and copper in the range from 0 to 50 ps delay.

4.3.2 Data treatment and errors

During the experiment we quickly realized that the motion of the sample stage could not be perfectly synchronized with the grid spacing of the supporting mesh of the foils. Therefore, some laser and/or x-ray pulses only hit the grid and not the intended foil location next to it, producing nickel diffraction lines in case of the x-rays. After noticing these events, we quickly stopped the motion and adjusted the spatial overlap with the mesh. But

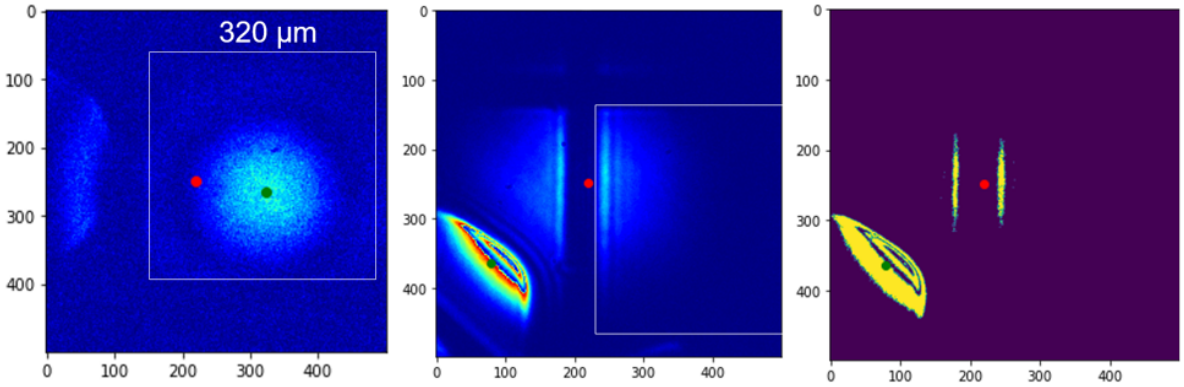

Figure 4.24: Images from the laser focus diagnostics. The nominal position of the x-rays as measured with a YAG screen is marked by the red dot. The left and middle images both show example events filtered out in the data analysis. Left: the x-rays probe too far from the laser maximum. Middle: both laser and x-rays hit the mesh structure supporting the foil. In both, empty grid space to the left and on the top can be seen where the laser hit before. Right: the middle image after the application of Otsu-thresholding. The green dot indicate the centre of mass of the largest object. These images were used to separate good and bad hits.

the nickel diffraction does not account for unwanted laser hits. For a good shot, the focus monitor should show a circular laser focus in the centre of the foil and far away from the support mesh, which covers the much smaller x-ray focus close to its centre. If the laser hits the grid or far away from the x-ray spot, the fluence level in the probed region is lower than we expect, leading to less heating. To obtain a meaningful data set from similar conditions, these misses need to be filtered out.

To separate all bad events from good hits, I used the images from the laser focus spot diagnostic, which images the laser focus and the area around it (Fig. 4.24). To classify the the events, I applied an Otsu-filter [174] to the images. This assigns either the 'background' or 'foreground' property to each pixel, thereby producing a binary image. In these binary images I then selected the largest object, which should be the laser focus in the correct grid space. Multiple objects are possible for example, if the halo of the laser focus leaks through previously shot grid spaces. I posed two criteria for the largest object to count the event as a good hit and take it into further data processing. First, a good focus in free space should be circular or at least elliptic, leading to the criteria of an eccentricity of 0.35 or smaller. If the laser gets too close to the mesh, this requirement will be violated. Next, to ensure spatial overlap between laser and x-rays and that roughly the same conditions are probed, the area around the nominal x-ray spot should consist out of 'foreground' pixels by more than 85 %. This also filters out events where the x-ray spot is close to a mesh line, which could potentially produce strong nickel diffraction.

After the shots were sorted according to the optical diagnostic, the analysis on the IXS data can begin. All events passing the test were processed by the single photon counting algorithm and had their curvature corrected

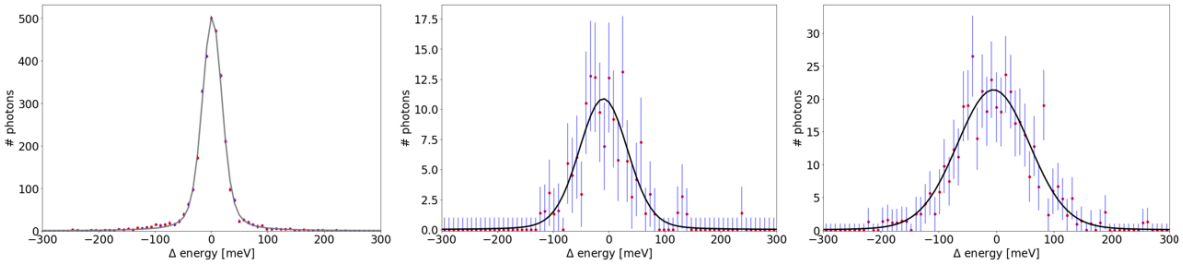

Figure 4.25: Combined spectra of all three analysers for three different time delays. Left: laser off, middle: 4 ps, and right: 35 ps. The cold spectrum has a FWHM close to the resolution limit of the setup, matching the width obtained from a thin PMMA sample. The other two time steps are both wider due to the heating. The black lines indicate a fit with a Voigt profile. The error bars show the Poisson counting error.

according to the procedure described for the 2191 experiment 4.1.1. As the signal level was very low (around 1 photon per shot for gold down to less than 0.2 for titanium) and the number of shots limited by measurement time and target costs, the signal of all three analysers was added together into a single spectrum before further analysis. As all three analysers were situated directly next to each other the deviations due to the different scattering vector of the outer analysers compared to the central analyser are small.

The correct offset to align the spectral axes of all analysers for further processing was determined from the cold gold spectra, where the individual analysers had enough signal to form a complete spectrum in reasonable time. This was possible due to a diffraction ring covering the analysers, which lead to a ~ 15 times higher photon count.

Heated ions and atoms in the gold will introduce a Doppler broadening in the scattered signal, as explained earlier 2.30. The narrow scattering from the cold gold was used as the standard to compare the temperature broadening against. To calculate this broadening, first the cold data was fitted with a Voigt profile using lmfit. For the heated curves, we assume that the broadening is Gaussian stemming from the velocity distributions of the ions. They were fitted with a Voigt profile too. The fits kept the Lorentzian part of the cold data fixed and took the Gaussian contribution as an unknown broadening convoluted with the Gaussian part of the cold fit (Fig. 4.25).

To assign a number to the ion temperature of the system, the width obtained from the fits is inserted into the equation for Doppler-broadening (Eq. 2.30)

$$T_i = \frac{1}{4}\frac{m_i c^2}{8ln2}\left(\frac{\Delta E}{E_0}\right)^2. \tag{4.4}$$

The next step is to estimate the errors on these values which were obtained by fitting. For that, I employed the module emcee [175] embedded into lmfit, which can use Markov chain Monte Carlo methods to estimate the probability function of parameters that agree with the given data set. Starting from the maximum likelihood

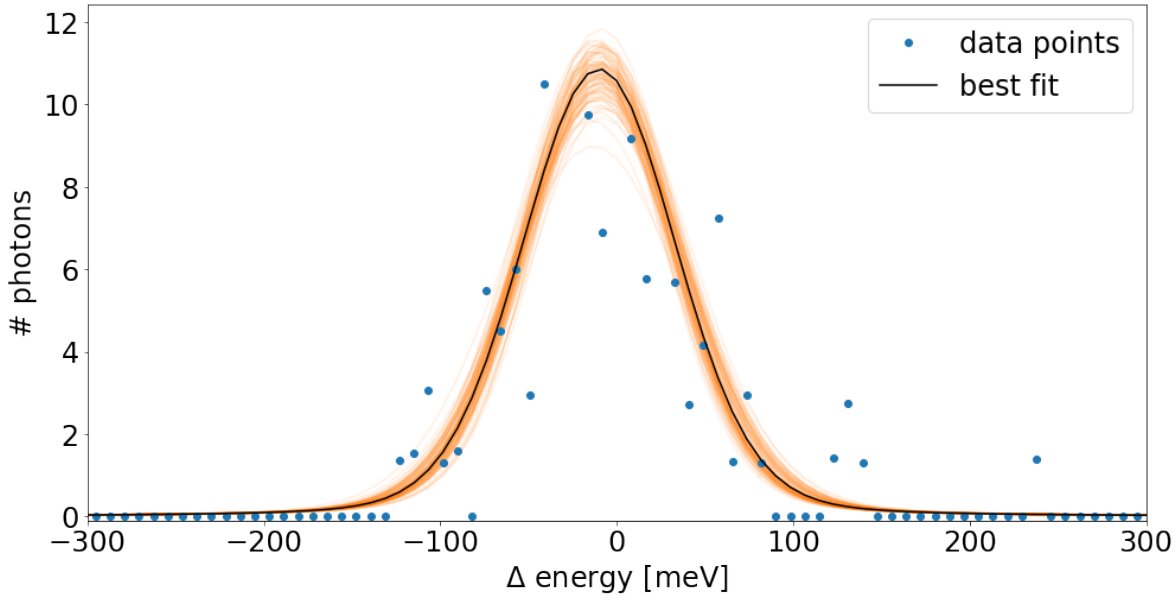

Figure 4.26: The maximum likelihood fit (black curve) to the data points calculated with the Python module SciPy. The module Emcee was used explore the parameter space of this fit. 100 randomly drawn samples out of 485000 are displayed here (orange curves). The errors of the fit parameters were taken from the $2\,\sigma$ range of these probability distributions, which is the area inside the white circles.

fit, it explores parameter space around it. I let 1000 walkers run a 10000 step chain and a 'burn-in' of the first 300 steps to discard the information about the starting values and let the walkers explore the parameter space. From these chains I sampled every 20th value (Fig. 4.26).

The resulting posterior probability distributions look all very similar to the one shown in the example image (Fig. 4.27). The symmetry of the two-dimensional projections off the diagonal indicates little correlations between the parameters. For the errors, I chose the $2\,\sigma$ range given by the posterior probability distribution. As the width is dependant on the broadening as well as the Lorentzian and Gaussian parts from the cold data, I propagated these errors to first obtain an error on the widths and then again to yield a final error on the ion temperature.

4.3.3 Ion temperature evolution in laser-pumped gold

During the LY2720 experiment we were able to measure excited gold at various time delays for two different fluence bands. The lower fluence is centred at $1.75\,\mathrm{J/cm^2} \pm 0.55\,\mathrm{J/cm^2}$, the higher at $4.63\,\mathrm{J/cm^2} \pm 1.05\,\mathrm{J/cm^2}$. Through the data analysis method described above (see 4.3.2) it is possible to obtain a direct measurement of the evolution of the ion temperature in the system. As the penetration of optical laser into the gold is only about $\sim 16\,nm$ [177], the energy transport within the sample mainly happens through ballistic electrons and electron-

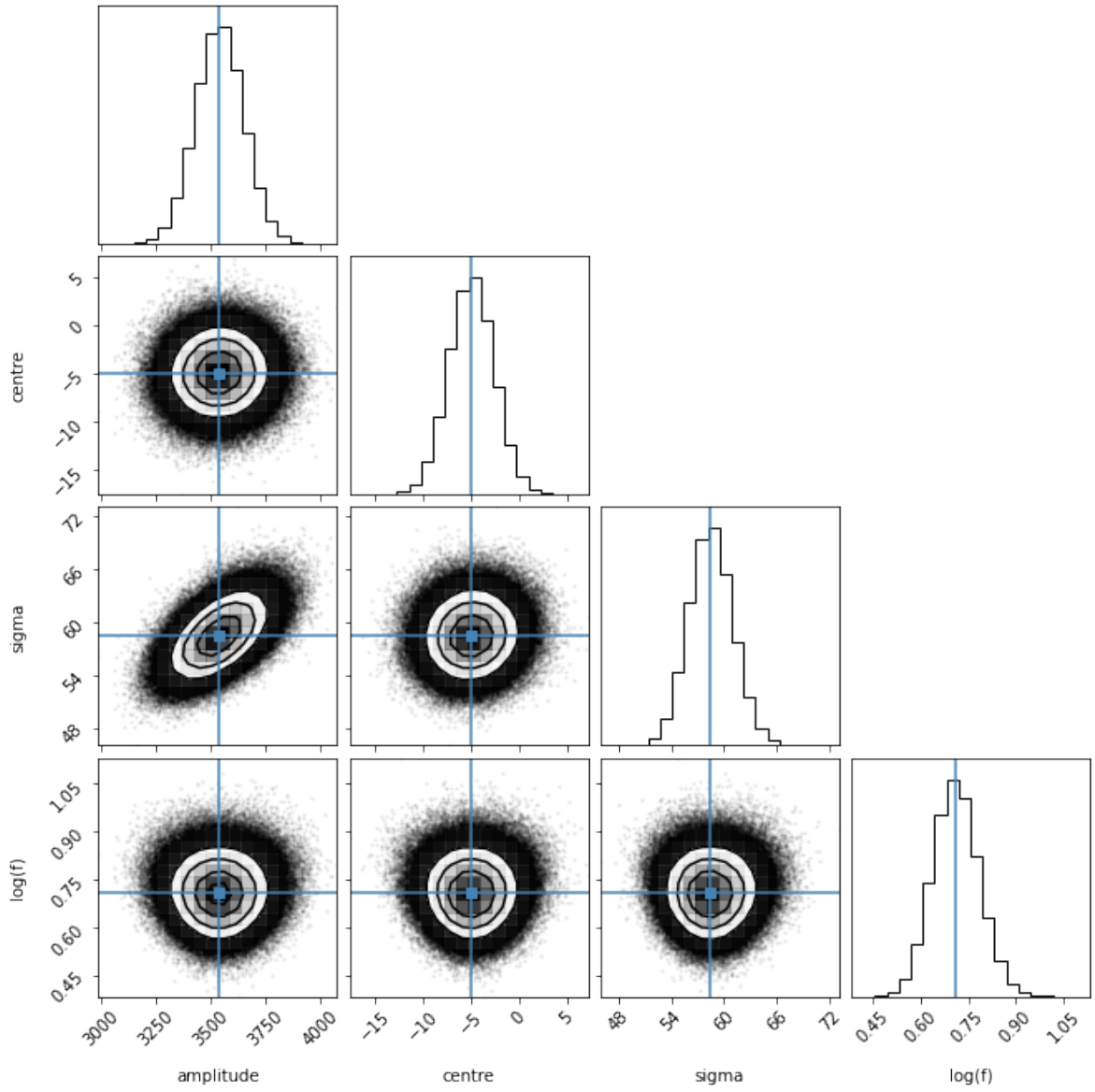

Figure 4.27: Visualization of the parameter space explored with emcee, generated with the Python module corner.py [176]. It shows the one (on the diagonal) and two dimensional (off diagonal) projections of the parameters probability distributions for a Voigt profile with the parameters: amplitude, centre, and sigma (broadening in addition to cold data). log(f) is the logarithm of the likelihood function. The blue lines indicate the position of the best fit parameters.

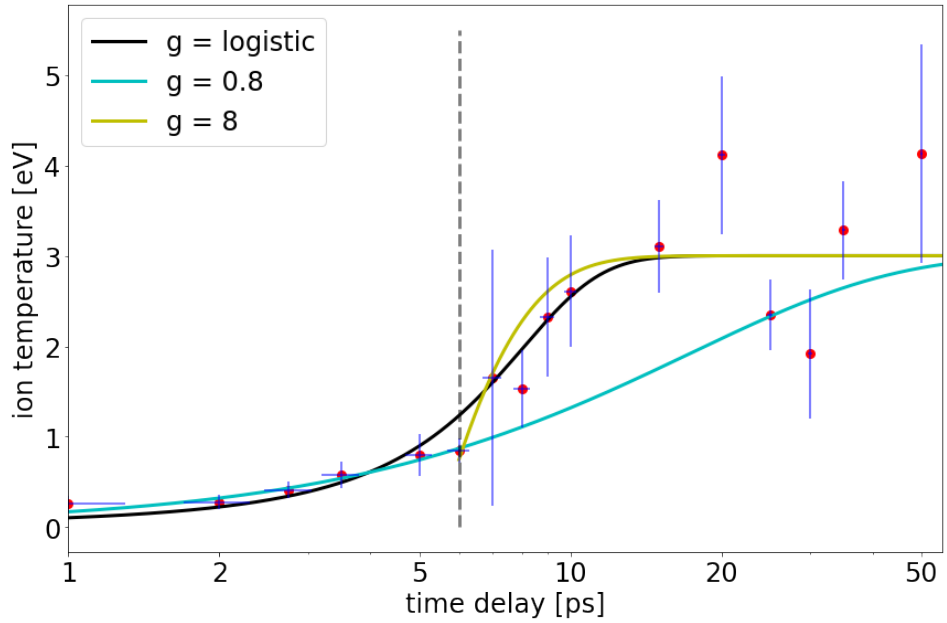

Figure 4.28: Ion temperature evolution of gold after excitation with an average fluence of $1.75 J/cm^2$ (red points). The dashed vertical line indicates the melting point. The solid lines represent calculated two-temperature models with different equilibration rates. The unit for the coupling parameter is $10^{17} \frac{W}{m^3 K}$.

electron collisions. Once the hot electron gas reaches thermal equilibrium, the electrons begin to diffuse into the bulk along the temperature gradient. While this process occurs, the hot electrons are losing energy to the ionic system and become cooler. The rate of this energy transfer is governed by the electron-ion coupling parameter g_{ei} and is well described by the two-temperature model (Eq. 2.8). As the electrons reach thermal equilibrium with the local lattice, the energy transport to distant and still cold parts of the bulk is determined by the lattice heat conductivity.

We can see this behaviour occur in the data point (Figs. 4.28, 4.29). Starting with the cold system, the ion temperature in both cases slowly begins to rise and then transitions into an area of faster heating before settling onto a final value in thermal equilibrium with the electron system. As can be seen from the disagreement between the measured data point and the lines according to calculated models, a simple two-temperature model with a single constant electron-ion coupling parameter g_{ei} is insufficient to properly describe the observed temperature evolution. Low values for the coupling constant fit well to the temperatures measured at early times < 4 ps but fail to reach thermal equilibrium fast enough to obey the data. In contrast, high values for g heat the system to quickly. The temperature models shown here were calculated with code based on the python module NTMpy [178]. For the calculations I used tabulated values at 300 K for the lattice heat capacity C_i [179], thermal conductivity K and electron specific heat constant A_e [180].

Due to the detailed analysis of the x-ray diffraction data performed by the group of T. White and the MEC

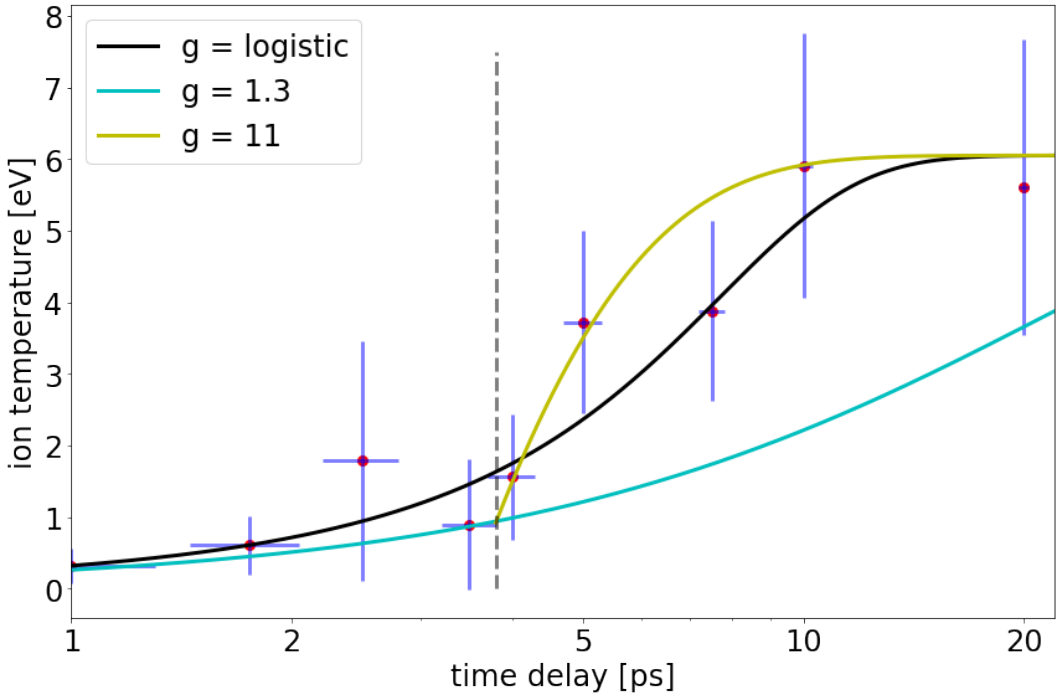

Figure 4.29: Ion temperature evolution of gold after excitation with an average fluence of $4.63 J/cm^2$ (red points). The dashed vertical line indicates the melting point. The solid lines represent calculated two-temperature models with different equilibration rates. The unit for the coupling parameter is $10^{17} \frac{W}{m^3 K}$

team, we could find that the moment where the disagreement between the calculated two-temperature model and data points becomes significant with the melting of the material, as seen by the disappearance of the diffraction lines due to the solid-liquid phase transition. For the lower fluence, melting occurs at around 6 ps, for the higher fluence around 3.8 ps.

Thus, we can demonstrate that a constant electron-ion coupling parameter fits well to the temperature evolution up until the melting point. After the phase transition, the evolution of the system can again be described with a constant coupling parameter, which is around 10 times higher (0.8×10^{17} *versus* 8×10^{17} $\frac{W}{m^3K}$ for the low fluence and 1.3×10^{17} *versus* 11×10^{17} $\frac{W}{m^3K}$ for the high fluence). Note that the coupling parameters are higher for the larger laser fluence. This indicates a dependence of the coupling parameter on the initial temperature of the electron bath after laser excitation, as measured by Mo *et al.* [181] with ultrafast electron diffraction and predicted by several theoretical models [182, 183]. Medvedev and Milov [183] additionally propose an almost linear dependence of the coupling parameter on the ion temperature, painting the overall picture that assuming a constant coupling even before melting is a simplified picture, as both electron and ion temperatures are quickly evolving. Therefore, a dynamic electron- and ion temperature dependent coupling parameter g_{ei} is probably what is happening, while our measurements are not precise enough to distinguish these dynamic changes from a constant value. The discontinuity at melting could also exist for a dynamically changing parameter when the coupling to the phonons in a solid changes to acoustic modes in the melt. A more accurate measurement is needed to determine these fine nuances. Also, a simultaneous measurement of the electron temperature will give a much more complete view of the overall process then just half of it as discussed here. Though we placed a spectrometer for this electron temperature measurement, the scattered signal was simply too weak for a reasonable analysis.

Finally, we have to consider on more aspect about the setup: As the analyser crystals were sitting above or very close to the x-ray axis, the measurement is sensitive to Doppler shifts along this axis. With the target foils at normal incidence and the laser at an angle of $\sim 10^\circ$ to the x-rays, this then coincides with the preferred direction for expansion of the samples due to heating. So latest from melting onwards, there is likely a component to the measured velocities stemming from the movement of the expanding target - and not from Doppler broadening. Unfortunately, we can not distinguish between this contributions within the measurement and will need additional measurements like VISAR or supporting simulations to quantify the expansion component.

4.3.4 Ion temperature evolution in other materials

As mentioned at the beginning of this section, we did not only perform the measurements on gold but also other metals, namely silver, titanium, and copper. With atomic numbers Z of 47, 22, and 29, the scattering cross section and thus the signal on the detector is correspondingly lower than in the case of gold, as it scales with Z.

In fact, running the same analysis scripts as for the gold yields no conclusive results for copper and titanium,

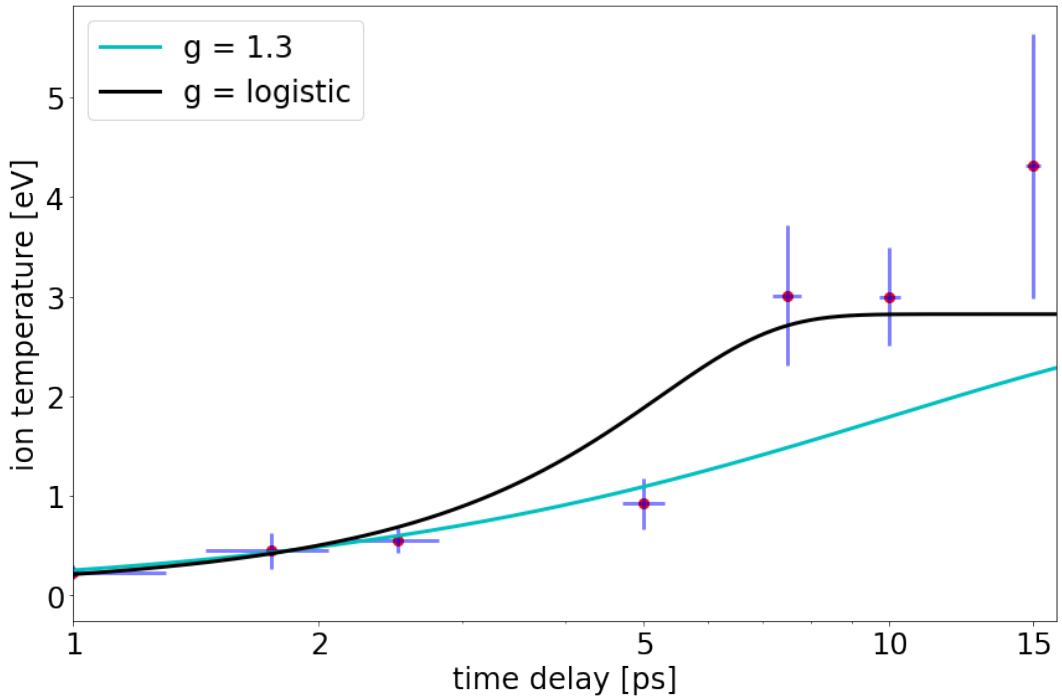

Figure 4.30: Measured ion temperature versus time delay for silver. Shown are the data points (red) and two calculated models for the temperature evolution. One with constant equilibration rate (cyan) and one dynamic (black).

as the signal-to-noise ratio is too low to fit curves to the data points. A comprehensive study would require much more samples and shots than we had available. However, an analysis for silver was possible (Fig. 4.30), though we only have data for one fluence band centred at $1.77 \pm 0.45 \frac{J}{cm^2}$ and a smaller number of time delays due to limited amounts of samples and increased number of shots necessary per data point to produce a sufficiently meaningful spectrum. Silver seems to show a temperature evolution similar to gold. A low g_{ei} fits the first data points, but raises the temperature too slow to fit the later points. A potential melting after 5 ps with corresponding jump in the coupling constant similar to gold can be imagined but is as off now unconfirmed by diffraction.

4.3.5 Summary

For the first time, we were able to directly observe the temporal evolution of the bulk ion temperature in laser-excited warm dense gold using inelastic x-ray scattering. We achieved this with sub-picosecond time resolution. From the data we could infer a several times higher electron-ion equilibration rate in the heated material than for the cold sample. This strong increase in the coupling parameter seems to correspond with the melting of the gold. In addition, we could observe that higher laser pulse energies used for the excitation result in a higher

equilibration rate. The same measurements were also attempted for silver, which displays a similar temporal evolution to gold.

Chapter 5

Conclusion and Outlook

5.1 Conclusion

The scope of this thesis was to develop and establish high-resolution inelastic x-ray scattering as a probe for temperature in warm dense matter states. A Si (533) monochromator together with diced analyzer crystals of the same cut form the core elements of the high-resolution inelastic scattering setup at the HED instrument at European XFEL, following similar user-provided instrumentation used at the MEC instrument at LCLS. In a proof-of-principle experiment it was shown that this spectrometer at HED performs very close to design values [127]. In addition, inelastic scattering from diamond at two different static temperatures confirmed the capabilities of the setup to determine temperature from collective inelastic scattering via detailed balance of the Stokes and anti-Stokes lines connected to phonon excitation and de-excitation.

After this successful demonstration, the technique was pushed to fulfill its design purpose in a new experiment, where the static sample was replaced with a dynamically excited target. Due to its geophysical relevance and abundance, solid-density iron was chosen. This experiment employed for the first time self-seeding of the XFEL in combination with the high-resolution spectrometer setup. Though we were unable to perform the experiment to its original goals, during this experiment and the succeeding data analysis we gained valuable knowledge and identified several challenges when performing this kind of experiment.

We successfully managed to operate the setup in self-seeded mode for the first time and also performed the very first experiment at the HED instrument employing the 1030 nm branch of the pp-laser. We obtained several thousand inelastically scattered photons from dynamically excited iron by raster-scanning a foil target with high repetition rate. The spectra from these photons show a clear difference to the scattering from the target without laser-excitation, which is validated by diffraction data obtained during the same campaign.

In two experiments at the MEC instrument at the LCLS we managed for the first time to successfully perform a direct measurement of the ion temperature in a dynamically evolving system. High-resolution IXS in

the non-collective regime was used to follow the ion temperature evolution of warm dense gold after excitation with fs-laser pulses. The experiments followed the temperature evolution in gold with picosecond time steps from room temperature to thermal equilibrium at 3 eV (6 eV, depending on laser fluence) after around 10 ps. The obtained data imposes boundaries to the value of the electron-ion coupling parameter g_{ei} and thus supports the validation or dismissal of theories describing the energy transfer in solids after the excitation with ultra-short pulsed lasers.

The technical developments and scientific experiments performed within the scope of this work demonstrate that high-resolution IXS experiments on laser driven states of matter to directly measure temperature or obtain material constants in compressed matter still pose a significant experimental challenge, even ten years after the first pioneering experiment at LCLS.

Nevertheless, when successfully performed, the data from these experiments opens up ways into previously unobtainable data sets. With the present setups, detailed characterization of dynamically created warm dense matter state in pressure, density and temperature will be possible, either for planetary interior science or fundamental laser-matter interaction.

5.2 Outlook

Of course, the above described experiments are only a snapshot of technical capabilities and scientific interest. Already at the time of writing this thesis, thoughts are put into new experiments and how to push the instrumentation further. What follows is a brief overview of some of these developments.

5.2.1 DiPOLE-100X Laser

New experimental opportunities are opened up by the commissioning of the DiPOLE-100X laser system at the HED instrument. In contrast to the pp-laser used in the iron experiment, it was designed to perform high repetition rate dynamic compression experiments. With a demonstrated performance of > 100 J per pulse at a rate of 10 Hz and a selection of phase plates, it is able to create homogeneous high-pressure states from ablation pressure in an area of a few hundred micrometres size. Thus, most of the issues we had in the iron experiment with spatial overlap, lateral gradients, homogeneity and walk-off between pump and probe will be eliminated.

This laser also possesses another great advantage over the existing high-power lasers at XFELs as it has a significantly higher shot rate. This property is especially suited for photon hungry experiments like the high-resolution IXS, where hundreds of shots are required for a single data point. This is of particular relevance when low-Z elements are involved, as is the case for many planetary compositions in gas or ice giants. DiPOLE-100X will enable IXS measurements for these laboratory astrophysics experiments within a realistic time duration so they become feasible inside a standard experiment slot. The system has also shown an unprecedented pulse

energy stability in first diffraction experiments, therefore providing very similar conditions on each shot, which increases the comparability of the data.

Planning for inelastic scattering experiments with both eV and meV resolutions by the user community is ongoing. They are expected to be scheduled in 2024/25.

5.2.2 Non-collective scattering from shocked samples

As discussed earlier, VISAR (see 1) is the default option in dynamic compression experiments to determine pressure via the surface particle speed at breakout. This method has several disadvantages, in that it is only a measurement of the surface particle velocity, not the bulk and relies on optical back reflection, giving a high reflectivity as a prerequisite. At high pressures it can also fail as materials become opaque. In contrast, measuring particle velocities via x-ray scattering is a bulk measurement. A shock wave will produce a shift of the bulk velocity inside the compressed material. If the correct geometry is chosen, this shift is large enough to be easily detectable with the high-resolution spectrometers presented in this work. As an example, a shock wave moving towards the detector will produce a shift of 50 meV in perfect backscattering for the x-rays for 7.5 keV photons and a particle velocity of 1000 m/s [184].

The shock wave will also increase the temperature in the compressed material. This will show itself in the Maxwell-Boltzmann distribution of the ions moving with the reference frame of the imparted particle velocity. This Doppler broadening due to temperature can be detected with the same setup, as demonstrated in the LY2720 experiment (see 4.3). An experiment to perform these measurements at MEC is proposed by B. Nagler (SLAC, CA, US) and T. White (Univ. Reno, NV, US).

5.2.3 Even Higher Spectral Resolution

The hr (high-resolution) IXS setups presented in the experiment section of this work all employ Si (533) channel-cut monochromators and diced analyzers crystals. As demonstrated above, the spectral resolution of this system is restricted to slightly above 40 meV. Any future collective scattering experiment therefore will need to study materials with phonon energy occupations around or above this value. Unfortunately, many solids under normal conditions have lower energy phonon modes, which will only become visible, if the sample is pressured enough to extend the phonon modes outside of the instrument function peak. Experiments which do not put the sample under considerable pressure (which would result in a very high sound speed), like the gold experiment discussed above, are consequently unfeasible in the collective scattering regime.

A first step in this direction was taken by the user group around E. McBride and A. Descamps (Univ. Belfast, UK) in the HED experiment 3071, ”Investigation of “Phonon Hardening” in ultrafast optically-pumped gold using high-resolution inelastic X-ray scattering”, from November 2022, for which I was the local contact – the liaison scientist between the users and the facility.

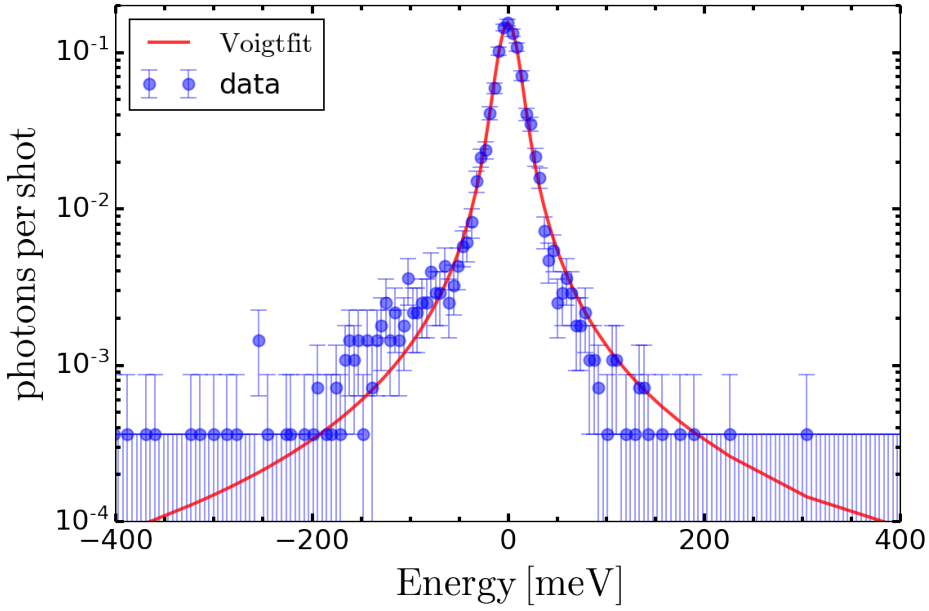

Figure 5.1: Quasi-elastic scattering from 50 μm PMMA while using Si (931) monochromator and analyzers measured during the HED experiment 3071. The FWHM value of the fit is 25 meV.

The experiment employed a Si (931) channel-cut monochromator with corresponding diced analyzer crystals at a photon energy of 10.896 keV to achieve a spectral resolution of ∼25 meV (Fig. 5.1). With this, or even better resolution at different crystal cuts, it becomes possible to study the materials with low frequency phonon modes - not limited to temperature measurements via detailed balance of the Stokes/anti-Stokes lines but also for a wider pool of effects concerning phonons or acoustic modes in dynamically excited matter, for which established hr-IXS setups at 3rd and 4th generation light sources lack the temporal resolution. In addition, the x-ray pulses need to contain a sufficient number of photons within the short time interval when the transient state exists, not only to measure noise but also an IXS signal.

5.2.4 X-ray Photon Correlation Spectroscopy

Lastly, x-ray photon correlation spectroscopy (XPCS) was recently proposed by G. Gregori (Univ. Oxford, UK). It could become a technique to determine temperature in dynamically excited matter states. In XPCS the coherence property of the FEL radiation is used to generate a speckle pattern on an area detector in the far-field. Changes in the structure of the sample will produce a change in the speckle pattern. Calculating the intensity auto-correlation function between these states enables conclusions on the motion of the atoms and thus, possibly temperature. XPCS is itself is already a well established method at XFELs, but mainly used with slower dynamics. The challenge for this technique will be whether it is possible to achieve the necessary spatial and temporal resolution.

Bibliography

[1] F. Graziani, M. P. Desjarlais, R. Redmer, and S. B. Trickey, eds., *Frontiers and Challenges in Warm Dense Matter*. Springer International Publishing, 2014.

[2] B. A. Buffett, "Earth's Core and the Geodynamo," *Science*, vol. 288, pp. 2007–2012, June 2000.

[3] T. G. Sharp and P. S. DeCarli, *Shock Effects in Meteorites*, pp. 653–678. University of Arizona Press, July 2006.

[4] D. S. Lauretta and H. Y. McSween, eds., *Meteorites and the Early Solar System II*. University of Arizona Press, July 2006.

[5] K. Falk, "Experimental methods for warm dense matter research," *High Power Laser Science and Engineering*, vol. 6, 2018.

[6] D. Riley, "Generation and characterisation of warm dense matter with intense lasers," *Plasma Physics and Controlled Fusion*, vol. 60, p. 014033, nov 2017.

[7] F. M. Bieniosek, J. J. Barnard, A. Friedman, E. Henestroza, J. Y. Jung, M. A. Leitner, S. Lidia, B. G. Logan, R. M. More, P. A. Ni, P. K. Roy, P. A. Seidl, and W. L. Waldron, "Ion-beam-driven warm dense matter experiments," *Journal of Physics: Conference Series*, vol. 244, p. 032028, Aug. 2010.

[8] J. Sun, D. D. Klug, and R. Martonák, "Structural transformations in carbon under extreme pressure: Beyond diamond," *The Journal of Chemical Physics*, vol. 130, May 2009.

[9] S. M. Clarke, J. P. S. Walsh, M. Amsler, C. D. Malliakas, T. Yu, S. Goedecker, Y. Wang, C. Wolverton, and D. E. Freedman, "Discovery of a Superconducting Cu-Bi Intermetallic Compound by High-Pressure Synthesis," *Angewandte Chemie International Edition*, vol. 55, pp. 13446–13449, Sept. 2016.

[10] M. G. Gorman, D. McGonegle, S. J. Tracy, S. M. Clarke, C. A. Bolme, A. E. Gleason, S. J. Ali, S. Hok, C. W. Greeff, P. G. Heighway, K. Hulpach, B. Glam, E. Galtier, H. J. Lee, J. S. Wark, J. H. Eggert, J. K. Wicks, and R. F. Smith, "Recovery of a high-pressure phase formed under laser-driven compression," *Physical Review B*, vol. 102, July 2020.

[11] D. Phillips, ed., *High Energy Density Welding Processes*, pp. 114–122. John Wiley & Sons, Ltd, 2016.

[12] W. M. Steen and J. Mazumder, *Laser Material Processing*. Springer London, 2010.

[13] S. Atzeni and J. Meyer-ter Vehn, *The Physics of Inertial Fusion*. Oxford University Press, June 2004.

[14] J. M. Walsh and R. H. Christian, "Equation of State of Metals from Shock Wave Measurements," *Physical Review*, vol. 97, pp. 1544–1556, Mar. 1955.

[15] F. Stacey and P. Davis, "High pressure equations of state with applications to the lower mantle and core," *Physics of the Earth and Planetary Interiors*, vol. 142, pp. 137–184, May 2004.

[16] R. B. Jacobs, "X-Ray Diffraction of Substances under High Pressures," *Physical Review*, vol. 54, pp. 325–331, Sept. 1938.

[17] Q. Johnson, A. Mitchell, R. N. Keeler, and L. Evans, "X-Ray Diffraction During Shock-Wave Compression," *Physical Review Letters*, vol. 25, pp. 1099–1101, Oct. 1970.

[18] G. E. Bacon and K. Lonsdale, "Neutron diffraction," *Reports on Progress in Physics*, vol. 16, pp. 1–61, Jan. 1953.

[19] M. Gemmi, E. Mugnaioli, T. E. Gorelik, U. Kolb, L. Palatinus, P. Boullay, S. Hovmöller, and J. P. Abrahams, "3D Electron Diffraction: The Nanocrystallography Revolution," *ACS Central Science*, vol. 5, pp. 1315–1329, July 2019.

[20] H. N. Chapman, A. Barty, M. J. Bogan, S. Boutet, M. Frank, S. P. Hau-Riege, S. Marchesini, B. W. Woods, S. Bajt, W. H. Benner, R. A. London, E. Plönjes, M. Kuhlmann, R. Treusch, S. Düsterer, T. Tschentscher, J. R. Schneider, E. Spiller, T. Möller, C. Bostedt, M. Hoener, D. A. Shapiro, K. O. Hodgson, D. van der Spoel, F. Burmeister, M. Bergh, C. Caleman, G. Huldt, M. M. Seibert, F. R. N. C. Maia, R. W. Lee, A. Szöke, N. Timneanu, and J. Hajdu, "Femtosecond diffractive imaging with a soft-X-ray free-electron laser," *Nature Physics*, vol. 2, pp. 839–843, nov 2006.

[21] S. P. Weathersby, G. Brown, M. Centurion, T. F. Chase, R. Coffee, J. Corbett, J. P. Eichner, J. C. Frisch, A. R. Fry, M. Gühr, N. Hartmann, C. Hast, R. Hettel, R. K. Jobe, E. N. Jongewaard, J. R. Lewandowski, R. K. Li, A. M. Lindenberg, I. Makasyuk, J. E. May, D. McCormick, M. N. Nguyen, A. H. Reid, X. Shen, K. Sokolowski-Tinten, T. Vecchione, S. L. Vetter, J. Wu, J. Yang, H. A. Dürr, and X. J. Wang, "Mega-electron-volt ultrafast electron diffraction at SLAC National Accelerator Laboratory," *Review of Scientific Instruments*, vol. 86, jul 2015.

[22] M. Z. Mo, X. Shen, Z. Chen, R. K. Li, M. Dunning, K. Sokolowski-Tinten, Q. Zheng, S. P. Weathersby, A. H. Reid, R. Coffee, I. Makasyuk, S. Edstrom, D. McCormick, K. Jobe, C. Hast, S. H. Glenzer, and

X. Wang, "Single-shot mega-electronvolt ultrafast electron diffraction for structure dynamic studies of warm dense matter," *Review of Scientific Instruments*, vol. 87, aug 2016.

[23] L. M. Barker, "Laser interferometry in shock-wave research," *Experimental Mechanics*, vol. 12, pp. 209–215, may 1972.

[24] P. M. Celliers, D. K. Bradley, G. W. Collins, D. G. Hicks, T. R. Boehly, and W. J. Armstrong, "Line-imaging velocimeter for shock diagnostics at the OMEGA laser facility," *Review of Scientific Instruments*, vol. 75, pp. 4916–4929, nov 2004.

[25] D. H. Dolan, "Accuracy and precision in photonic Doppler velocimetry," *Review of Scientific Instruments*, vol. 81, may 2010.

[26] W. J. M. Rankine, "XV. On the Thermodynamic Theory of Waves of Finite Longitudinal Disturbance," *Philosophical Transactions of the Royal Society of London*, vol. 160, pp. 277–288, dec 1870.

[27] P. H. Hugoniot, "Memoire sur la propagation du mouvement dans les corps etplus spécialement dans les gaz parfaits, 1e partie," *J. l'École Polytech.*, vol. 57, pp. 3–97, 1887.

[28] J. Stefan, "Über die Beziehung zwischen der Wärmestrahlung und der Temperatur," *Sitzungsber. Kaiserl. Akad. Wiss. Math. Naturwiss. Cl. II. Abth.*, vol. 79, no. 3, pp. 391–428, 1879.

[29] L. Boltzmann, "Ableitung des Stefan'schen Gesetzes, betreffend die Abhängigkeit der Wärmestrahlung von der Temperatur aus der electromagnetischen Lichttheorie," *Annalen der Physik*, vol. 258, pp. 291–294, Jan. 1884.

[30] D. L. McDonald, "Neutron diffraction study of the debye-waller factor for aluminum," *Acta Crystallographica*, vol. 23, pp. 185–191, Aug. 1967.

[31] A. Dunand, H. D. Flack, and K. Yvon, "Bonding study of tic and tin. i. high-precision x-ray-diffraction determination of the valence-electron density distribution, debye-waller temperature factors, and atomic static displacements in $\mathbf{TiC}_{0.94}$ and $\mathbf{TiN}_{0.99}$," *Physical Review B*, vol. 31, pp. 2299–2315, Feb. 1985.

[32] H. X. Gao and L.-M. Peng, "Parameterization of the temperature dependence of the debye–waller factors," *Acta Crystallographica Section A Foundations of Crystallography*, vol. 55, pp. 926–932, sep 1999.

[33] F. D. Vila, J. J. Rehr, H. H. Rossner, and H. J. Krappe, "Theoretical x-ray absorption Debye-Waller factors," *Physical Review B*, vol. 76, July 2007.

[34] S. M. Sharma and Y. M. Gupta, "Inherent issues regarding the use of *in situ* x-ray diffraction measurements to determine temperature in shock-compressed metals," *Physical Review B*, vol. 104, aug 2021.

[35] E. Burkel, "Phonon spectroscopy by inelastic x-ray scattering," *Reports on Progress in Physics*, vol. 63, pp. 171–232, jan 2000.

[36] F. Sette, M. H. Krisch, C. Masciovecchio, G. Ruocco, and G. Monaco, "Dynamics of Glasses and Glass-Forming Liquids Studied by Inelastic X-ray Scattering," *Science*, vol. 280, pp. 1550–1555, jun 1998.

[37] H. Sinn, "Spectroscopy with mev energy resolution," *Journal of Physics: Condensed Matter*, vol. 13, pp. 7525–7537, Aug. 2001.

[38] A. Q. R. Baron, "Introduction to High-Resolution Inelastic X-Ray Scattering," 2015.

[39] T. Scopigno, G. Ruocco, and F. Sette, "Microscopic dynamics in liquid metals: The experimental point of view," *Reviews of Modern Physics*, vol. 77, pp. 881–933, Sept. 2005.

[40] M. Bitter, S. von Goeler, R. Horton, M. Goldman, K. W. Hill, N. R. Sauthoff, and W. Stodiek, "Doppler-Broadening Measurements of X-Ray Lines for Determination of the Ion Temperature in Tokamak Plasmas," *Physical Review Letters*, vol. 42, pp. 304–307, Jan. 1979.

[41] W. Decking, S. Abeghyan, P. Abramian, A. Abramsky, A. Aguirre, C. Albrecht, P. Alou, M. Altarelli, P. Altmann, K. Amyan, V. Anashin, E. Apostolov, K. Appel, D. Auguste, V. Ayvazyan, S. Baark, F. Babies, N. Baboi, P. Bak, V. Balandin, R. Baldinger, B. Baranasic, S. Barbanotti, O. Belikov, V. Belokurov, L. Belova, V. Belyakov, S. Berry, M. Bertucci, B. Beutner, A. Block, M. Blöcher, T. Böckmann, C. Bohm, M. Böhnert, V. Bondar, E. Bondarchuk, M. Bonezzi, P. Borowiec, C. Bösch, U. Bösenberg, A. Bosotti, R. Böspflug, M. Bousonville, E. Boyd, Y. Bozhko, A. Brand, J. Branlard, S. Briechle, F. Brinker, S. Brinker, R. Brinkmann, S. Brockhauser, O. Brovko, H. Brück, A. Brüdgam, L. Butkowski, T. Büttner, J. Calero, E. Castro-Carballo, G. Cattalanotto, J. Charrier, J. Chen, A. Cherepenko, V. Cheskidov, M. Chiodini, A. Chong, S. Choroba, M. Chorowski, D. Churanov, W. Cichalewski, M. Clausen, W. Clement, C. Cloué, J. A. Cobos, N. Coppola, S. Cunis, K. Czuba, M. Czwalinna, B. D'Almagne, J. Dammann, H. Danared, A. de Zubiaurre Wagner, A. Delfs, T. Delfs, F. Dietrich, T. Dietrich, M. Dohlus, M. Dommach, A. Donat, X. Dong, N. Doynikov, M. Dressel, M. Duda, P. Duda, H. Eckoldt, W. Ehsan, J. Eidam, F. Eints, C. Engling, U. Englisch, A. Ermakov, K. Escherich, J. Eschke, E. Saldin, M. Faesing, A. Fallou, M. Felber, M. Fenner, B. Fernandes, J. M. Fernández, S. Feuker, K. Filippakopoulos, K. Floettmann, V. Fogel, M. Fontaine, A. Francés, I. F. Martin, W. Freund, T. Freyermuth, M. Friedland, L. Fröhlich, M. Fusetti, J. Fydrych, A. Gallas, O. García, L. Garcia-Tabares, G. Geloni, N. Gerasimova, C. Gerth, P. Geßler, V. Gharibyan, M. Gloor, J. Głowinkowski, A. Goessel, Z. Gołkebiewski, N. Golubeva, W. Grabowski, W. Graeff, A. Grebentsov, M. Grecki, T. Grevsmuehl, M. Gross, U. Grosse-Wortmann, J. Grünert, S. Grunewald, P. Grzegory, G. Feng, H. Guler, G. Gusev, J. L. Gutierrez, L. Hagge, M. Hamberg, R. Hanneken, E. Harms, I. Hartl, A. Hauberg, S. Hauf, J. Hauschildt, J. Hauser, J. Havlicek,

A. Hedqvist, N. Heidbrook, F. Hellberg, D. Henning, O. Hensler, T. Hermann, A. Hidvégi, M. Hierholzer, H. Hintz, F. Hoffmann, M. Hoffmann, M. Hoffmann, Y. Holler, M. Hüning, A. Ignatenko, M. Ilchen, A. Iluk, J. Iversen, J. Iversen, M. Izquierdo, L. Jachmann, N. Jardon, U. Jastrow, K. Jensch, J. Jensen, M. Jeżabek, M. Jidda, H. Jin, N. Johannson, R. Jonas, W. Kaabi, D. Kaefer, R. Kammering, H. Kapitza, S. Karabekyan, S. Karstensen, K. Kasprzak, V. Katalev, D. Keese, B. Keil, M. Kholopov, M. Killenberger, B. Kitaev, Y. Klimchenko, R. Klos, L. Knebel, A. Koch, M. Koepke, S. Köhler, W. Köhler, N. Kohlstrunk, Z. Konopkova, A. Konstantinov, W. Kook, W. Koprek, M. Körfer, O. Korth, A. Kosarev, K. Kosiński, D. Kostin, Y. Kot, A. Kotarba, T. Kozak, V. Kozak, R. Kramert, M. Krasilnikov, A. Krasnov, B. Krause, L. Kravchuk, O. Krebs, R. Kretschmer, J. Kreutzkamp, O. Kröplin, K. Krzysik, G. Kube, H. Kuehn, N. Kujala, V. Kulikov, V. Kuzminych, D. L. Civita, M. Lacroix, T. Lamb, A. Lancetov, M. Larsson, D. L. Pinvidic, S. Lederer, T. Lensch, D. Lenz, A. Leuschner, F. Levenhagen, Y. Li, J. Liebing, L. Lilje, T. Limberg, D. Lipka, B. List, J. Liu, S. Liu, B. Lorbeer, J. Lorkiewicz, H. H. Lu, F. Ludwig, K. Machau, W. Maciocha, C. Madec, C. Magueur, C. Maiano, I. Maksimova, K. Malcher, T. Maltezopoulos, E. Mamoshkina, B. Manschwetus, F. Marcellini, G. Marinkovic, T. Martinez, H. Martirosyan, W. Maschmann, M. Maslov, A. Matheisen, U. Mavric, J. Meißner, K. Meissner, M. Messerschmidt, N. Meyners, G. Michalski, P. Michelato, N. Mildner, M. Moe, F. Moglia, C. Mohr, S. Mohr, W. Möller, M. Mommerz, L. Monaco, C. Montiel, M. Moretti, I. Morozov, P. Morozov, D. Mross, J. Mueller, C. Müller, J. Müller, K. Müller, J. Munilla, A. Münnich, V. Muratov, O. Napoly, B. Näser, N. Nefedov, R. Neumann, R. Neumann, N. Ngada, D. Noelle, F. Obier, I. Okunev, J. A. Oliver, M. Omet, A. Oppelt, A. Ottmar, M. Oublaid, C. Pagani, R. Paparella, V. Paramonov, C. Peitzmann, J. Penning, A. Perus, F. Peters, B. Petersen, A. Petrov, I. Petrov, S. Pfeiffer, J. Pflüger, S. Philipp, Y. Pienaud, P. Pierini, S. Pivovarov, M. Planas, E. Pławski, M. Pohl, J. Polinski, V. Popov, S. Prat, J. Prenting, G. Priebe, H. Pryschelski, K. Przygoda, E. Pyata, B. Racky, A. Rathjen, W. Ratuschni, S. Regnaud-Campderros, K. Rehlich, D. Reschke, C. Robson, J. Roever, M. Roggli, J. Rothenburg, E. Rusiński, R. Rybaniec, H. Sahling, M. Salmani, L. Samoylova, D. Sanzone, F. Saretzki, O. Sawlanski, J. Schaffran, H. Schlarb, M. Schlösser, V. Schlott, C. Schmidt, F. Schmidt-Foehre, M. Schmitz, M. Schmökel, T. Schnautz, E. Schneidmiller, M. Scholz, B. Schöneburg, J. Schultze, C. Schulz, A. Schwarz, J. Sekutowicz, D. Sellmann, E. Semenov, S. Serkez, D. Sertore, N. Shehzad, P. Shemarykin, L. Shi, M. Sienkiewicz, D. Sikora, M. Sikorski, A. Silenzi, C. Simon, W. Singer, X. Singer, H. Sinn, K. Sinram, N. Skvorodnev, P. Smirnow, T. Sommer, A. Sorokin, M. Stadler, M. Steckel, B. Steffen, N. Steinhau-Kühl, F. Stephan, M. Stodulski, M. Stolper, A. Sulimov, R. Susen, J. Świerblewski, C. Sydlo, E. Syresin, V. Sytchev, J. Szuba, N. Tesch, J. Thie, A. Thiebault, K. Tiedtke, D. Tischhauser, J. Tolkiehn, S. Tomin, F. Tonisch, F. Toral, I. Torbin, A. Trapp, D. Treyer, G. Trowitzsch, T. Trublet, T. Tschentscher, F. Ullrich, M. Vannoni, P. Varela, G. Varghese, G. Vashchenko, M. Vasic, C. Vazquez-Velez, A. Verguet, S. Vilcins-Czvitkovits, R. Villanueva, B. Visentin, M. Viti, E. Vogel, E. Volobuev, R. Wagner, N. Walker, T. Wamsat, H. Weddig, G. We-

ichert, H. Weise, R. Wenndorf, M. Werner, R. Wichmann, C. Wiebers, M. Wiencek, T. Wilksen, I. Will, L. Winkelmann, M. Winkowski, K. Wittenburg, A. Witzig, P. Wlk, T. Wohlenberg, M. Wojciechowski, F. Wolff-Fabris, G. Wrochna, K. Wrona, M. Yakopov, B. Yang, F. Yang, M. Yurkov, I. Zagorodnov, P. Zalden, A. Zavadtsev, D. Zavadtsev, A. Zhirnov, A. Zhukov, V. Ziemann, A. Zolotov, N. Zolotukhina, F. Zummack, and D. Zybin, "A MHz-repetition-rate hard X-ray free-electron laser driven by a superconducting linear accelerator," *Nature Photonics*, may 2020.

[42] T. H. Maiman, "Stimulated Optical Radiation in Ruby," *Nature*, vol. 187, pp. 493–494, aug 1960.

[43] A. Kritcher, T. Döppner, D. Swift, J. Hawreliak, G. Collins, J. Nilsen, B. Bachmann, E. Dewald, D. Strozzi, S. Felker, O. Landen, O. Jones, C. Thomas, J. Hammer, C. Keane, H. Lee, S. Glenzer, S. Rothman, D. Chapman, D. Kraus, P. Neumayer, and R. Falcone, "Probing matter at Gbar pressures at the NIF," *High Energy Density Physics*, vol. 10, pp. 27–34, Mar. 2014.

[44] A. B. Zylstra, O. A. Hurricane, D. A. Callahan, A. L. Kritcher, J. E. Ralph, H. F. Robey, J. S. Ross, C. V. Young, K. L. Baker, D. T. Casey, T. Döppner, L. Divol, M. Hohenberger, S. Le Pape, A. Pak, P. K. Patel, R. Tommasini, S. J. Ali, P. A. Amendt, L. J. Atherton, B. Bachmann, D. Bailey, L. R. Benedetti, L. Berzak Hopkins, R. Betti, S. D. Bhandarkar, J. Biener, R. M. Bionta, N. W. Birge, E. J. Bond, D. K. Bradley, T. Braun, T. M. Briggs, M. W. Bruhn, P. M. Celliers, B. Chang, T. Chapman, H. Chen, C. Choate, A. R. Christopherson, D. S. Clark, J. W. Crippen, E. L. Dewald, T. R. Dittrich, M. J. Edwards, W. A. Farmer, J. E. Field, D. Fittinghoff, J. Frenje, J. Gaffney, M. Gatu Johnson, S. H. Glenzer, G. P. Grim, S. Haan, K. D. Hahn, G. N. Hall, B. A. Hammel, J. Harte, E. Hartouni, J. E. Heebner, V. J. Hernandez, H. Herrmann, M. C. Herrmann, D. E. Hinkel, D. D. Ho, J. P. Holder, W. W. Hsing, H. Huang, K. D. Humbird, N. Izumi, L. C. Jarrott, J. Jeet, O. Jones, G. D. Kerbel, S. M. Kerr, S. F. Khan, J. Kilkenny, Y. Kim, H. Geppert Kleinrath, V. Geppert Kleinrath, C. Kong, J. M. Koning, J. J. Kroll, M. K. G. Kruse, B. Kustowski, O. L. Landen, S. Langer, D. Larson, N. C. Lemos, J. D. Lindl, T. Ma, M. J. MacDonald, B. J. MacGowan, A. J. Mackinnon, S. A. MacLaren, A. G. MacPhee, M. M. Marinak, D. A. Mariscal, E. V. Marley, L. Masse, K. Meaney, N. B. Meezan, P. A. Michel, M. Millot, J. L. Milovich, J. D. Moody, A. S. Moore, J. W. Morton, T. Murphy, K. Newman, J.-M. G. Di Nicola, A. Nikroo, R. Nora, M. V. Patel, L. J. Pelz, J. L. Peterson, Y. Ping, B. B. Pollock, M. Ratledge, N. G. Rice, H. Rinderknecht, M. Rosen, M. S. Rubery, J. D. Salmonson, J. Sater, S. Schiaffino, D. J. Schlossberg, M. B. Schneider, C. R. Schroeder, H. A. Scott, S. M. Sepke, K. Sequoia, M. W. Sherlock, S. Shin, V. A. Smalyuk, B. K. Spears, P. T. Springer, M. Stadermann, S. Stoupin, D. J. Strozzi, L. J. Suter, C. A. Thomas, R. P. J. Town, E. R. Tubman, C. Trosseille, P. L. Volegov, C. R. Weber, K. Widmann, C. Wild, C. H. Wilde, B. M. Van Wonterghem, D. T. Woods, B. N. Woodworth, M. Yamaguchi, S. T. Yang, and G. B. Zimmerman, "Burning plasma achieved in inertial fusion," *Nature*, vol. 601, pp. 542–548, Jan. 2022.

[45] D. Strickland and G. Mourou, "Compression of amplified chirped optical pulses," *Optics Communications*, vol. 56, pp. 219–221, Dec. 1985.

[46] C. Radier, O. Chalus, M. Charbonneau, S. Thambirajah, G. Deschamps, S. David, J. Barbe, E. Etter, G. Matras, S. Ricaud, V. Leroux, C. Richard, F. Lureau, A. Baleanu, R. Banici, A. Gradinariu, C. Caldararu, C. Capiteanu, A. Naziru, B. Diaconescu, V. Iancu, R. Dabu, D. Ursescu, I. Dancus, C. A. Ur, K. A. Tanaka, and N. V. Zamfir, "10 PW peak power femtosecond laser pulses at ELI-NP," *High Power Laser Science and Engineering*, vol. 10, 2022.

[47] A. L. Garcia, H. Höppner, A. Pelka, C. Bähtz, E. Brambrink, S. D. D. Cafiso, J. Dreyer, S. Göde, M. Hassan, T. Kluge, J. Liu, M. Makita, D. Möller, M. Nakatsutsumi, T. R. Preston, G. Priebe, H.-P. Schlenvoigt, J.-P. Schwinkendorf, M. Šmíd, A.-M. Talposi, M. Toncian, U. Zastrau, U. Schramm, T. E. Cowan, and T. Toncian, "ReLaX: the Helmholtz International Beamline for Extreme Fields high-intensity short-pulse laser driver for relativistic laser–matter interaction and strong-field science using the high energy density instrument at the European X-ray free electron laser facility," *High Power Laser Science and Engineering*, vol. 9, 2021.

[48] P. Gibbon, *Short Pulse Laser Interactions with Matter: An Introduction*. PUBLISHED BY IMPERIAL COLLEGE PRESS AND DISTRIBUTED BY WORLD SCIENTIFIC PUBLISHING CO., Sept. 2005.

[49] V. E. Fortov, *Extreme States of Matter*. Springer International Publishing, 2016.

[50] R. P. Drake, *High-Energy-Density Physics*. Springer International Publishing, 2018.

[51] P. Agostini, F. Fabre, G. Mainfray, G. Petite, and N. K. Rahman, "Free-Free Transitions Following Six-Photon Ionization of Xenon Atoms," *Physical Review Letters*, vol. 42, pp. 1127–1130, Apr. 1979.

[52] M. Ammosov, N. Delone, and V. Krainov, "Tunnel ionization of complex atoms and of atomic ions in an alternating electromagnetic field," *Sov. Phys.*, 1986.

[53] C.-L. Pan, C.-H. Lin, C.-S. Yang, and A. Zaytsev, *Laser Ablation of Polymethylmethacrylate (PMMA) by Phase- Controlled Femtosecond Two-Color Synthesized Waveforms*. InTech, Dec. 2016.

[54] W. S. Fann, R. Storz, H. W. K. Tom, and J. Bokor, "Direct measurement of nonequilibrium electron-energy distributions in subpicosecond laser-heated gold films," *Physical Review Letters*, vol. 68, pp. 2834–2837, May 1992.

[55] W. S. Fann, R. Storz, H. W. K. Tom, and J. Bokor, "Electron thermalization in gold," *Physical Review B*, vol. 46, pp. 13592–13595, Nov. 1992.

[56] Anisimov, S. I. and Kapeliovich, B. L. and Perel'Man, T. L., ""Electron emission from metal surfaces exposed to ultrashort laser pulses"," *Soviet Journal of Experimental and Theoretical Physics*, vol. 39, pp. 375–377, 1974.

[57] D. W. Forslund, J. M. Kindel, K. Lee, E. L. Lindman, and R. L. Morse, "Theory and simulation of resonant absorption in a hot plasma," *Physical Review A*, vol. 11, pp. 679–683, Feb. 1975.

[58] K. G. Estabrook, E. J. Valeo, and W. L. Kruer, "Two-dimensional relativistic simulations of resonance absorption," *The Physics of Fluids*, vol. 18, pp. 1151–1159, Sept. 1975.

[59] P. J. Wegner, J. M. Auerbach, T. A. B. Jr., S. N. Dixit, J. K. Lawson, J. A. Menapace, T. G. Parham, D. W. Swift, P. K. Whitman, and W. H. Williams, "NIF final optics system: frequency conversion and beam conditioning," in *Optical Engineering at the Lawrence Livermore National Laboratory II: The National Ignition Facility* (M. A. Lane and C. R. Wuest, eds.), vol. 5341, pp. 180 – 189, International Society for Optics and Photonics, SPIE, 2004.

[60] S. I. Anisimov, A. M. Prokhorov, and V. E. Fortov, "Application of high-power lasers to study matter at ultrahigh pressures," *Soviet Physics Uspekhi*, vol. 27, pp. 181–205, Mar. 1984.

[61] F. F. Chen, *Introduction to Plasma Physics and Controlled Fusion*. Springer International Publishing, 2016.

[62] B. Dorner, E. Burkel, T. Illini, and J. Peisl, "First measurement of a phonon dispersion curve by inelastic X-ray scattering," *Zeitschrift für Physik B Condensed Matter*, vol. 69, pp. 179–183, jun 1987.

[63] F. Sette, G. Ruocco, M. Krisch, U. Bergmann, C. Masciovecchio, V. Mazzacurati, G. Signorelli, and R. Verbeni, "Collective Dynamics in Water by High Energy Resolution Inelastic X-Ray Scattering," *Physical Review Letters*, vol. 75, pp. 850–853, jul 1995.

[64] G. L. Squires, *Introduction to the Theory of Thermal Neutron Scattering (3rd ed.)*. Cambridge University Press, mar 2012.

[65] W. Schuelke, *Electron Dynamics by Inelastic X-Ray Scattering*. PRACTITIONER LAW, 2007.

[66] D. Attwood, *Soft X-rays and Extreme Ultraviolet Radiation*. Cambridge University Press, 1999.

[67] F. Schwabl, *Advanced Quantum Mechanics*. Springer Berlin Heidelberg, 2008.

[68] E. Burkel, "Introduction to x-ray scattering," *Journal of Physics: Condensed Matter*, vol. 13, pp. 7477–7498, aug 2001.

[69] S. K. Sinha, "Theory of inelastic x-ray scattering from condensed matter," *Journal of Physics: Condensed Matter*, vol. 13, pp. 7511–7523, aug 2001.

[70] P. Dirac, "The quantum theory of the emission and absorption of radiation," *Proceedings of the Royal Society of London. Series A, Containing Papers of a Mathematical and Physical Character*, vol. 114, pp. 243–265, mar 1927.

[71] F. Schwabl, *Quantum Mechanics*. Springer Berlin Heidelberg, 2007.

[72] J. Thomson, *Conduction of Electricity Through Gases*. Cambridge physical series, University Press, 1906.

[73] S. J. J. Thomson and G. P. Thomson, "Conduction of Electricity through Gases," *The Journal of Physical Chemistry*, vol. 38, pp. 987–987, July 1934.

[74] J. D. Jackson, *Classical Electrodynamics*. WILEY, 1998.

[75] N. D. Ashcroft, Neil W.; Mermin, *Solid state physics*. Saunders College Publishing, 1976.

[76] C. Doppler, "Über das farbige Licht der Doppelsterne und einiger anderer Gestirne des Himmels," *Abhandlungen der Königl. Böhm. Gesellschaft der Wissenschaften*, vol. 2, pp. 465–482, 1842.

[77] J. C. Maxwell, *Illustrations of the dynamical theory of gases. Part I. On the motions and collisions of perfectly elastic spheres. The London, Edinburgh and Dublin philosophical magazine and journal of science*, vol. ser.4:v.19 (1860:Jan.-June). London, Taylor & Francis, [1840-1944], 1860. https://www.biodiversitylibrary.org/bibliography/58679.

[78] J. C. Maxwell, *Illustrations of the dynamical theory of gases. Part II. On the process of diffusion of two or more kinds of moving particles among one another. The London, Edinburgh and Dublin philosophical magazine and journal of science*, vol. ser.4:v.20 (1860:July-Dec.). London, Taylor & Francis, [1840-1944], 1860. https://www.biodiversitylibrary.org/bibliography/58679.

[79] L. Boltzmann, "Weitere Studien über das Wärmegleichgewicht unter Gasmolekülen.," *Sitzungsberichte Akademie der Wissenschaften*, vol. 66, pp. 275–370, 1872.

[80] A. M. Kondratenko and E. L. Saldin, "Generating Of Coherent Radiation By A Relativistic Electron beam In An ondulator," *Part. Accel.*, vol. 10, pp. 207–216, 1980.

[81] G. Geloni, V. Kocharyan, and E. Saldin, "A novel self-seeding scheme for hard X-ray FELs," *Journal of Modern Optics*, vol. 58, pp. 1391–1403, sep 2011.

[82] E. L. Saldin, E. A. Schneidmiller, and M. V. Yurkov, *The Physics of Free Electron Lasers*. Springer Berlin Heidelberg, 1999.

[83] H. P. Freund and T. M. Antonsen, *Principles of Free Electron Lasers*. Springer International Publishing, 2018.

[84] E. J. Jaeschke, S. Khan, J. R. Schneider, and J. B. Hastings, eds., *Synchrotron Light Sources and Free-Electron Lasers*. Springer International Publishing, 2016.

[85] P. Schmüser, M. Dohlus, J. Rossbach, and C. Behrens, *Free-Electron Lasers in the Ultraviolet and X-Ray Regime*. Springer International Publishing, 2014.

[86] J. Larmor, "On the theory of the magnetic influence on spectra and on the radiation from moving ions," *The London, Edinburgh, and Dublin Philosophical Magazine and Journal of Science*, vol. 44, pp. 503–512, dec 1897.

[87] Y. V. Shvyd'ko, S. Stoupin, A. Cunsolo, A. H. Said, and X. Huang, "High-reflectivity high-resolution X-ray crystal optics with diamonds," *Nature Physics*, vol. 6, pp. 196–199, Jan. 2010.

[88] K.-J. Kim, "An analysis of self-amplified spontaneous emission," *Nuclear Instruments and Methods in Physics Research Section A: Accelerators, Spectrometers, Detectors and Associated Equipment*, vol. 250, pp. 396–403, Sept. 1986.

[89] N. Hartmann, G. Hartmann, R. Heider, M. S. Wagner, M. Ilchen, J. Buck, A. O. Lindahl, C. Benko, J. Grünert, J. Krzywinski, J. Liu, A. A. Lutman, A. Marinelli, T. Maxwell, A. A. Miahnahri, S. P. Moeller, M. Planas, J. Robinson, A. K. Kazansky, N. M. Kabachnik, J. Viefhaus, T. Feurer, R. Kienberger, R. N. Coffee, and W. Helml, "Attosecond time-energy structure of x-ray free-electron laser pulses," *Nature Photonics*, vol. 12, pp. 215–220, Mar. 2018.

[90] Feldhaus, J. and Saldin, E.L. and Schneider, J.R. and Schneidmiller, E.A. and Yurkov, M.V., "Possible application of x-ray optical elements for reducing the spectral bandwidth of an x-ray sase fel," *Optics Communications*, vol. 140, pp. 341–352, Aug. 1997.

[91] E. Saldin, E. Schneidmiller, and M. Yurkov, "Statistical properties of radiation from VUV and X-ray free electron laser," *Optics Communications*, vol. 148, pp. 383–403, mar 1998.

[92] C. Darwin, "The Theory of X-ray Reflexion," *Phil. Mag. 6, 27, 315-333*, 1914.

[93] P. P. Ewald, "Zur Begründung der Kristalloptik," *Annalen der Physik*, vol. 359, no. 23, pp. 519–556, 1917.

[94] B. W. Baterman and H. Cole, "Dynamical Diffraction of X Rays by Perfect Crystals," *Reviews of Modern Physics*, vol. 36, pp. 681–717, jul 1964.

[95] J. Als-Nielsen and D. McMorrow, *Elements of Modern X-ray Physics*. John Wiley & Sons, Inc., mar 2011.

[96] A. Authier, *Dynamical Theory of X-Ray Diffraction*. OUP Oxford, 2003.

[97] Y. Shvyd'ko, *X-Ray Optics*. Springer Berlin Heidelberg, 2004.

[98] W. H. Miller, *A treatise on crystallography*. Cambridge, For J. & J. J. Deighton, 1839.

[99] Y. V. Shvyd'ko, E. Gerdau, J. Jäschke, O. Leupold, M. Lucht, and H. D. Rüter, "Exact Bragg backscattering of x rays," *Physical Review B*, vol. 57, pp. 4968–4971, mar 1998.

[100] M. Deutsch and M. Hart, "High-energy x-ray anomalous dispersion correction for silicon," *Physical Review B*, vol. 37, pp. 2701–2703, feb 1988.

[101] S. A. Stepanov, "X-ray server: an online resource for simulations of x-ray diffraction and scattering," in *Advances in Computational Methods for X-Ray and Neutron Optics* (M. S. del Rio, ed.), SPIE, oct 2004.

[102] *X-Ray Server URL: http://x-server.gmca.aps.anl.gov*.

[103] X. Dong, D. Shu, and H. Sinn, "Design of a cryo-cooled artificial channel-cut crystal monochromator for the European XFEL," *AIP Conference Proceedings*, vol. 1741, p. 040027, July 2016.

[104] L. Wollenweber, "A high-resolution crystal monochromator for the European X-ray Free-Electron Laser," Master's thesis, Universität Hamburg, 2018.

[105] P. Mason, S. Banerjee, J. Smith, T. Butcher, J. Phillips, H. Höppner, D. Möller, K. Ertel, M. D. Vido, I. Hollingham, A. Norton, S. Tomlinson, T. Zata, J. S. Merchan, C. Hooker, M. Tyldesley, T. Toncian, C. Hernandez-Gomez, C. Edwards, and J. Collier, "Development of a 100 J, 10 Hz laser for compression experiments at the High Energy Density instrument at the European XFEL," *High Power Laser Science and Engineering*, vol. 6, 2018.

[106] "www.hibef.eu."

[107] S. Serkez, G. Geloni, M. Guetg, V. Kocharyan, S. Liu, and E. Saldin, "Delay-detune scan for longitudinal electron beam characterization at free-electron lasers," *Physical Review Accelerators and Beams*, vol. 23, dec 2020.

[108] S. Serkez, O. Gorobtsov, D. E. Rivas, M. Meyer, B. Sobko, N. Gerasimova, N. Kujala, and G. Geloni, "Wigner distribution of self-amplified spontaneous emission free-electron laser pulses and extracting its autocorrelation," *Journal of Synchrotron Radiation*, vol. 28, pp. 3–17, jan 2021.

[109] P. Kirkpatrick and A. V. Baez, "Formation of Optical Images by X-Rays," *Journal of the Optical Society of America*, vol. 38, p. 766, Sept. 1948.

[110] J. H. Underwood, T. W. Barbee, and C. Frieber, "X-ray microscope with multilayer mirrors," *Applied Optics*, vol. 25, p. 1730, June 1986.

[111] D. H. Bilderback, S. A. Hoffman, and D. J. Thiel, "Nanometer Spatial Resolution Achieved in Hard X-Ray Imaging and Laue Diffraction Experiments," *Science*, vol. 263, pp. 201–203, Jan. 1994.

[112] V. Aristov, Y. Basov, G. Kulipanov, V. Pindyurin, A. Snigirev, and A. Sokolov, "Focusing properties of a Bragg-Fresnel lens in the white spectrum of synchrotron radiation," *Nuclear Instruments and Methods in Physics Research Section A: Accelerators, Spectrometers, Detectors and Associated Equipment*, vol. 274, pp. 390–393, Jan. 1989.

[113] B. Lai, W. B. Yun, D. Legnini, Y. Xiao, J. Chrzas, P. J. Viccaro, V. White, S. Bajikar, D. Denton, F. Cerrina, E. Di Fabrizio, M. Gentili, L. Grella, and M. Baciocchi, "Hard x-ray phase zone plate fabricated by lithographic techniques," *Applied Physics Letters*, vol. 61, pp. 1877–1879, Oct. 1992.

[114] S. Lagomarsino, A. Cedola, P. Cloetens, S. Di Fonzo, W. Jark, G. Soullié, and C. Riekel, "Phase contrast hard x-ray microscopy with submicron resolution," *Applied Physics Letters*, vol. 71, pp. 2557–2559, Nov. 1997.

[115] B. Lengeler, C. G. Schroer, B. Benner, T. F. Günzler, M. Kuhlmann, J. Tümmler, A. S. Simionovici, M. Drakopoulos, A. Snigirev, and I. Snigireva, "Parabolic refractive X-ray lenses: a breakthrough in X-ray optics," *Nuclear Instruments and Methods in Physics Research Section A: Accelerators, Spectrometers, Detectors and Associated Equipment*, vol. 467-468, pp. 944–950, jul 2001.

[116] C. Masciovecchio, U. Bergmann, M. Krisch, G. Ruocco, F. Sette, and R. Verbeni, "A perfect crystal X-ray analyser with meV energy resolution," *Nuclear Instruments and Methods in Physics Research Section B: Beam Interactions with Materials and Atoms*, vol. 111, pp. 181–186, apr 1996.

[117] C. Masciovecchio, U. Bergmann, M. Krisch, G. Ruocco, F. Sette, and R. Verbeni, "A perfect crystal X-ray analyser with 1.5 meV energy resolution," *Nuclear Instruments and Methods in Physics Research Section B: Beam Interactions with Materials and Atoms*, vol. 117, pp. 339–340, sep 1996.

[118] R. Verbeni, M. Kocsis, S. Huotari, M. Krisch, G. Monaco, F. Sette, and G. Vanko, "Advances in crystal analyzers for inelastic X-ray scattering," *Journal of Physics and Chemistry of Solids*, vol. 66, pp. 2299–2305, dec 2005.

[119] G. Blaj, P. Caragiulo, G. Carini, S. Carron, A. Dragone, D. Freytag, G. Haller, P. Hart, J. Hasi, R. Herbst, S. Herrmann, C. Kenney, B. Markovic, K. Nishimura, S. Osier, J. Pines, B. Reese, J. Segal, A. Tomada, and M. Weaver, "X-ray detectors at the Linac Coherent Light Source," *Journal of Synchrotron Radiation*, vol. 22, pp. 577–583, apr 2015.

[120] A. Mozzanica, A. Bergamaschi, S. Cartier, R. Dinapoli, D. Greiffenberg, I. Johnson, J. Jungmann, D. Maliakal, D. Mezza, C. Ruder, L. Schaedler, B. Schmitt, X. Shi, and G. Tinti, "Prototype characteri-

zation of the JUNGFRAU pixel detector for SwissFEL," *Journal of Instrumentation*, vol. 9, pp. C05010–C05010, May 2014.

[121] A. Mozzanica, A. Bergamaschi, M. Brueckner, S. Cartier, R. Dinapoli, D. Greiffenberg, J. Jungmann-Smith, D. Maliakal, D. Mezza, M. Ramilli, C. Ruder, L. Schaedler, B. Schmitt, X. Shi, and G. Tinti, "Characterization results of the JUNGFRAU full scale readout ASIC," *Journal of Instrumentation*, vol. 11, pp. C02047–C02047, Feb. 2016.

[122] H. H. Johann, "Die Erzeugung lichtstarker Röntgenspektren mit Hilfe von Konkavkristallen," *Zeitschrift für Physik*, vol. 69, pp. 185–206, may 1931.

[123] J. M. DuMond and H. A. Kirkpatrick, "A Direct Spectrum of the Structure and Shift of the Compton Line with Helium Gas as the Scatterer," *Physical Review*, vol. 52, pp. 419–436, sep 1937.

[124] S. Huotari, G. Vankó, F. Albergamo, C. Ponchut, H. Graafsma, C. Henriquet, R. Verbeni, and G. Monaco, "Improving the performance of high-resolution X-ray spectrometers with position-sensitive pixel detectors," *Journal of Synchrotron Radiation*, vol. 12, pp. 467–472, jun 2005.

[125] S. Huotari, F. Albergamo, G. Vankó, R. Verbeni, and G. Monaco, "Resonant inelastic hard x-ray scattering with diced analyzer crystals and position-sensitive detectors," *Review of Scientific Instruments*, vol. 77, p. 053102, may 2006.

[126] M. Moretti Sala, K. Martel, C. Henriquet, A. Al Zein, L. Simonelli, C. J. Sahle, H. Gonzalez, M.-C. Lagier, C. Ponchut, S. Huotari, R. Verbeni, M. Krisch, and G. Monaco, "A high-energy-resolution resonant inelastic X-ray scattering spectrometer at ID20 of the European Synchrotron Radiation Facility," *Journal of Synchrotron Radiation*, vol. 25, pp. 580–591, Mar 2018.

[127] L. Wollenweber, T. R. Preston, A. Descamps, V. Cerantola, A. Comley, J. H. Eggert, L. B. Fletcher, G. Geloni, D. O. Gericke, S. H. Glenzer, S. Göde, J. Hastings, O. S. Humphries, A. Jenei, O. Karnbach, Z. Konopkova, R. Loetzsch, B. Marx-Glowna, E. E. McBride, D. McGonegle, G. Monaco, B. K. Ofori-Okai, C. A. J. Palmer, C. Plückthun, R. Redmer, C. Strohm, I. Thorpe, T. Tschentscher, I. Uschmann, J. S. Wark, T. G. White, K. Appel, G. Gregori, and U. Zastrau, "High-resolution inelastic x-ray scattering at the high energy density scientific instrument at the European X-Ray Free-Electron Laser," *Review of Scientific Instruments*, vol. 92, p. 013101, jan 2021.

[128] B. Nagler, B. Arnold, G. Bouchard, R. F. Boyce, R. M. Boyce, A. Callen, M. Campell, R. Curiel, E. Galtier, J. Garofoli, E. Granados, J. Hastings, G. Hays, P. Heimann, R. W. Lee, D. Milathianaki, L. Plummer, A. Schropp, A. Wallace, M. Welch, W. White, Z. Xing, J. Yin, J. Young, U. Zastrau, and H. J. Lee, "The Matter in Extreme Conditions instrument at the Linac Coherent Light Source," *Journal of Synchrotron Radiation*, vol. 22, pp. 520–525, apr 2015.

[129] T. Tschentscher, C. Bressler, J. Grünert, A. Madsen, A. Mancuso, M. Meyer, A. Scherz, H. Sinn, and U. Zastrau, "Photon Beam Transport and Scientific Instruments at the European XFEL," *Applied Sciences*, vol. 7, p. 592, jun 2017.

[130] S. Abeghyan, M. Bagha-Shanjani, G. Chen, U. Englisch, S. Karabekyan, Y. Li, F. Preisskorn, F. Wolff-Fabris, M. Wuenschel, M. Yakopov, and J. Pflueger, "First operation of the SASE1 undulator system of the European X-ray Free-Electron Laser," *Journal of Synchrotron Radiation*, vol. 26, pp. 302–310, feb 2019.

[131] U. Zastrau, K. Appel, C. Baehtz, O. Baehr, L. Batchelor, A. Berghäuser, M. Banjafar, E. Brambrink, V. Cerantola, T. E. Cowan, H. Damker, S. Dietrich, S. D. D. Cafiso, J. Dreyer, H.-O. Engel, T. Feldmann, S. Findeisen, M. Foese, D. Fulla-Marsa, S. Göde, M. Hassan, J. Hauser, T. Herrmannsdörfer, H. Höppner, J. Kaa, P. Kaever, K. Knöfel, Z. Konôpková, A. L. García, H.-P. Liermann, J. Mainberger, M. Makita, E.-C. Martens, E. E. McBride, D. Möller, M. Nakatsutsumi, A. Pelka, C. Plueckthun, C. Prescher, T. R. Preston, M. Röper, A. Schmidt, W. Seidel, J.-P. Schwinkendorf, M. O. Schoelmerich, U. Schramm, A. Schropp, C. Strohm, K. Sukharnikov, P. Talkovski, I. Thorpe, M. Toncian, T. Toncian, L. Wollenweber, S. Yamamoto, and T. Tschentscher, "The High Energy Density Scientific Instrument at the European XFEL," *Journal of Synchrotron Radiation*, vol. 28, pp. 1393–1416, aug 2021.

[132] H. Sinn, M. Dommach, B. Dickert, M. D. Felice, X. Dong, J. Eidam, D. Finze, I. Freijo-Martin, N. Gerasimova, N. Kohlstrunk, D. L. Civita, F. Meyn, V. Music, M. Neumann, M. Petrich, B. Rio, L. Samoylova, S. Schmidtchen, M. Störmer, A. Trapp, M. Vannoni, R. Villanueva, and F. Yang, "The SASE1 X-ray beam transport system," *Journal of Synchrotron Radiation*, vol. 26, pp. 692–699, apr 2019.

[133] T. Maltezopoulos, F. Dietrich, W. Freund, U. F. Jastrow, A. Koch, J. Laksman, J. Liu, M. Planas, A. A. Sorokin, K. Tiedtke, and J. Grünert, "Operation of X-ray gas monitors at the European XFEL," *Journal of Synchrotron Radiation*, vol. 26, pp. 1045–1051, jun 2019.

[134] J. Grünert, M. P. Carbonell, F. Dietrich, T. Falk, W. Freund, A. Koch, N. Kujala, J. Laksman, J. Liu, T. Maltezopoulos, K. Tiedtke, U. F. Jastrow, A. Sorokin, E. Syresin, A. Grebentsov, and O. Brovko, "X-ray photon diagnostics at the European XFEL," *Journal of Synchrotron Radiation*, vol. 26, pp. 1422–1431, aug 2019.

[135] N. Kujala, W. Freund, J. Liu, A. Koch, T. Falk, M. Planas, F. Dietrich, J. Laksman, T. Maltezopoulos, J. Risch, F. Dall'Antonia, and J. Grünert, "Hard x-ray single-shot spectrometer at the European X-ray Free-Electron Laser," *Review of Scientific Instruments*, vol. 91, p. 103101, oct 2020.

[136] A. Madsen, J. Hallmann, G. Ansaldi, T. Roth, W. Lu, C. Kim, U. Boesenberg, A. Zozulya, J. Möller, R. Shayduk, M. Scholz, A. Bartmann, A. Schmidt, I. Lobato, K. Sukharnikov, M. Reiser, K. Kazarian,

and I. Petrov, "Materials Imaging and Dynamics (MID) instrument at the European X-ray Free-Electron Laser Facility," *Journal of Synchrotron Radiation*, vol. 28, pp. 637–649, feb 2021.

[137] S. Makarov, M. Makita, M. Nakatsutsumi, T. Pikuz, N. Ozaki, T. R. Preston, K. Appel, Z. Konopkova, V. Cerantola, E. Brambrink, J.-P. Schwinkendorf, I. Mohacsi, T. Burian, J. Chalupsky, V. Hajkova, L. Juha, V. Vozda, B. Nagler, U. Zastrau, and S. Pikuz, "Direct LiF imaging diagnostics on refractive X-ray focusing at the EuXFEL High Energy Density instrument," *Journal of Synchrotron Radiation*, vol. 30, pp. 208–216, jan 2023.

[138] M. Pergament, G. Palmer, M. Kellert, K. Kruse, J. Wang, L. Wissmann, U. Wegner, M. Emons, D. Kane, G. Priebe, S. Venkatesan, T. Jezynski, F. Pallas, and M. J. Lederer, "Versatile optical laser system for experiments at the European X-ray free-electron laser facility," *Optics Express*, vol. 24, p. 29349, dec 2016.

[139] H. P. Liermann, Z. Konôpková, K. Appel, C. Prescher, A. Schropp, V. Cerantola, R. J. Husband, J. D. McHardy, M. I. McMahon, R. S. McWilliams, C. M. Pépin, J. Mainberger, M. Roeper, A. Berghäuser, H. Damker, P. Talkovski, M. Foese, N. Kujala, O. B. Ball, M. A. Baron, R. Briggs, M. Bykov, E. Bykova, J. Chantel, A. L. Coleman, H. Cynn, D. Dattelbaum, L. E. Dresselhaus-Marais, J. H. Eggert, L. Ehm, W. J. Evans, G. Fiquet, M. Frost, K. Glazyrin, A. F. Goncharov, H. Hwang, Z. Jenei, J.-Y. Kim, F. Langenhorst, Y. Lee, M. Makita, H. Marquardt, E. E. McBride, S. Merkel, G. Morard, E. F. O'Bannon, C. Otzen, E. J. Pace, A. Pelka, J. S. Pigott, V. B. Prakapenka, R. Redmer, C. Sanchez-Valle, M. Schoelmerich, S. Speziale, G. Spiekermann, B. T. Sturtevant, S. Toleikis, N. Velisavljevic, M. Wilke, C.-S. Yoo, C. Baehtz, U. Zastrau, and C. Strohm, "Novel experimental setup for megahertz X-ray diffraction in a diamond anvil cell at the High Energy Density (HED) instrument of the European X-ray Free-Electron Laser (EuXFEL)," *Journal of Synchrotron Radiation*, vol. 28, pp. 688–706, apr 2021.

[140] P. A. Frey and G. H. Reed, "The Ubiquity of Iron," *ACS Chemical Biology*, vol. 7, pp. 1477–1481, Aug. 2012.

[141] J.-P. Poirier, "Light elements in the Earth's outer core: A critical review," *Physics of the Earth and Planetary Interiors*, vol. 85, pp. 319–337, Sept. 1994.

[142] D. Alfè, M. J. Gillan, and G. D. Price, "Temperature and composition of the Earth's core," *Contemporary Physics*, vol. 48, pp. 63–80, Mar. 2007.

[143] T. Lay, J. Hernlund, and B. A. Buffett, "Core-mantle boundary heat flow," *Nature Geoscience*, vol. 1, pp. 25–32, Jan. 2008.

[144] S. Anzellini, A. Dewaele, M. Mezouar, P. Loubeyre, and G. Morard, "Melting of Iron at Earth's Inner Core Boundary Based on Fast X-ray Diffraction," *Science*, vol. 340, pp. 464–466, Apr. 2013.

[145] S. J. Turneaure, S. M. Sharma, and Y. M. Gupta, "Crystal Structure and Melting of Fe Shock Compressed to 273 GPa: In Situ X-Ray Diffraction," *Physical Review Letters*, vol. 125, Nov. 2020.

[146] A. B. Belonoshko, N. V. Skorodumova, A. Rosengren, and B. Johansson, "Elastic Anisotropy of Earth's Inner Core," *Science*, vol. 319, pp. 797–800, Feb. 2008.

[147] S. Tateno, K. Hirose, Y. Ohishi, and Y. Tatsumi, "The Structure of Iron in Earth's Inner Core," *Science*, vol. 330, pp. 359–361, Oct. 2010.

[148] V. Cerantola, E. Bykova, I. Kupenko, M. Merlini, L. Ismailova, C. McCammon, M. Bykov, A. I. Chumakov, S. Petitgirard, I. Kantor, V. Svitlyk, J. Jacobs, M. Hanfland, M. Mezouar, C. Prescher, R. Rüffer, V. B. Prakapenka, and L. Dubrovinsky, "Stability of iron-bearing carbonates in the deep Earth's interior," *Nature Communications*, vol. 8, July 2017.

[149] J. M. Kaa, C. Sternemann, K. Appel, V. Cerantola, T. R. Preston, C. Albers, M. Elbers, L. Libon, M. Makita, A. Pelka, S. Petitgirard, C. Plückthun, V. Roddatis, C. J. Sahle, G. Spiekermann, C. Schmidt, A. Schreiber, R. Sakrowski, M. Tolan, M. Wilke, U. Zastrau, and Z. Konôpková, "Structural and electron spin state changes in an x-ray heated iron carbonate system at the Earth's lower mantle pressures," *Physical Review Research*, vol. 4, July 2022.

[150] C. Albers, R. Sakrowski, L. Libon, G. Spiekermann, B. Winkler, C. Schmidt, L. Bayarjargal, V. Cerantola, S. Chariton, N. Giordano, H. Gretarsson, J. Kaa, H.-P. Liermann, M. Sundermann, N. Thiering, M. Tolan, M. Wilke, and C. Sternemann, "Fe^{3+}-hosting carbon phases in the deep Earth," *Physical Review B*, vol. 105, feb 2022.

[151] H. K. Mao, J. Xu, V. V. Struzhkin, J. Shu, R. J. Hemley, W. Sturhahn, M. Y. Hu, E. E. Alp, L. Vocadlo, D. Alfè, G. D. Price, M. J. Gillan, M. Schwoerer-Böhning, D. Häusermann, P. Eng, G. Shen, H. Giefers, R. Lübbers, and G. Wortmann, "Phonon Density of States of Iron up to 153 Gigapascals," *Science*, vol. 292, pp. 914–916, may 2001.

[152] A. Descamps, B. K. Ofori-Okai, K. Appel, V. Cerantola, A. Comley, J. H. Eggert, L. B. Fletcher, D. O. Gericke, S. Göde, O. Humphries, O. Karnbach, A. Lazicki, R. Loetzsch, D. McGonegle, C. A. J. Palmer, C. Plueckthun, T. R. Preston, R. Redmer, D. G. Senesky, C. Strohm, I. Uschmann, T. G. White, L. Wollenweber, G. Monaco, J. S. Wark, J. B. Hastings, U. Zastrau, G. Gregori, S. H. Glenzer, and E. E. McBride, "An approach for the measurement of the bulk temperature of single crystal diamond using an X-ray free electron laser," *Scientific Reports*, vol. 10, sep 2020.

[153] E. E. McBride, T. G. White, A. Descamps, L. B. Fletcher, K. Appel, F. P. Condamine, C. B. Curry, F. Dallari, S. Funk, E. Galtier, M. Gauthier, S. Göde, J. B. Kim, H. J. Lee, B. K. Ofori-Okai, M. Oliver,

A. Rigby, C. Schoenwaelder, P. Sun, T. Tschentscher, B. B. L. Witte, U. Zastrau, G. Gregori, B. Nagler, J. Hastings, S. H. Glenzer, and G. Monaco, "Setup for meV-resolution inelastic X-ray scattering measurements and X-ray diffraction at the Matter in Extreme Conditions endstation at the Linac Coherent Light Source," *Review of Scientific Instruments*, vol. 89, p. 10F104, oct 2018.

[154] D. Windisch and P. Becker, "Silicon lattice parameters as an absolute scale of length for high precision measurements of fundamental constants," *physica status solidi (a)*, vol. 118, pp. 379–388, apr 1990.

[155] M. Newville, T. Stensitzki, D. B. Allen, and A. Ingargiola, "LMFIT: Non-Linear Least-Square Minimization and Curve-Fitting for Python," 2014.

[156] J. L. Warren, J. L. Yarnell, G. Dolling, and R. A. Cowley, "Lattice Dynamics of Diamond," *Physical Review*, vol. 158, pp. 805–808, jun 1967.

[157] E. Burkel, ed., *Inelastic Scattering*. Springer Berlin Heidelberg, 1991.

[158] M. Schwoerer-Böhning, A. T. Macrander, and D. A. Arms, "Phonon Dispersion of Diamond Measured by Inelastic X-Ray Scattering," *Physical Review Letters*, vol. 80, pp. 5572–5575, jun 1998.

[159] O. Karnbach, *X-Ray Thomson Scattering as DynamicTemperature and Microstructure Diagnostic*. PhD thesis, University of Oxford, 2022.

[160] P. Mason, M. Divoký, K. Ertel, J. Pilař, T. Butcher, M. Hanuš, S. Banerjee, J. Phillips, J. Smith, M. D. Vido, A. Lucianetti, C. Hernandez-Gomez, C. Edwards, T. Mocek, and J. Collier, "Kilowatt average power 100 J-level diode pumped solid state laser," *Optica*, vol. 4, p. 438, apr 2017.

[161] R. Ramis, R. Schmalz, and J. Meyer-Ter-Vehn, "MULTI — a computer code for one-dimensional multigroup radiation hydrodynamics," *Computer Physics Communications*, vol. 49, pp. 475–505, jun 1988.

[162] T. Preston, S. Göde, J.-P. Schwinkendorf, K. Appel, E. Brambrink, V. Cerantola, H. Höppner, M. Makita, A. Pelka, C. Prescher, K. Sukharnikov, A. Schmidt, I. Thorpe, T. Toncian, A. Amouretti, D. Chekrygina, R. Falcone, K. Falk, L. Fletcher, E. Galtier, M. Harmand, N. Hartley, S. Hau-Riege, P. Heimann, L. Huang, O. Humphries, O. Karnbach, D. Kraus, H. Lee, B. Nagler, S. Ren, A. Schuster, M. Smid, K. Voigt, M. Zhang, and U. Zastrau, "Design and performance characterisation of the HAPG von Hámos Spectrometer at the High Energy Density Instrument of the European XFEL," *Journal of Instrumentation*, vol. 15, pp. P11033–P11033, nov 2020.

[163] M. Hu, W. Sturhahn, T. Toellner, P. Hession, J. Sutter, and E. Alp, "Data analysis for inelastic nuclear resonant absorption experiments," *Nuclear Instruments and Methods in Physics Research Section A: Accelerators, Spectrometers, Detectors and Associated Equipment*, vol. 428, pp. 551–555, jun 1999.

[164] C. Prescher and V. B. Prakapenka, "DIOPTAS: a program for reduction of two-dimensional X-ray diffraction data and data exploration," *High Pressure Research*, vol. 35, pp. 223–230, jun 2015.

[165] G. I. Kerley, "Multiphase equation of state for iron," tech. rep., feb 1993.

[166] Y. S. Touloukian, R. K. Kirby, R. E. Taylor, and P. D. Desai, *Thermophysical Properties of Matter*, vol. Volume 12. IFEPlenum, New York, 1975.

[167] B. Fryxell, K. Olson, P. Ricker, F. X. Timmes, M. Zingale, D. Q. Lamb, P. MacNeice, R. Rosner, J. W. Truran, and H. Tufo, "FLASH: An Adaptive Mesh Hydrodynamics Code for Modeling Astrophysical Thermonuclear Flashes," *The Astrophysical Journal Supplement Series*, vol. 131, pp. 273–334, nov 2000.

[168] A. Dubey, K. Antypas, M. K. Ganapathy, L. B. Reid, K. Riley, D. Sheeler, A. Siegel, and K. Weide, "Extensible component-based architecture for FLASH, a massively parallel, multiphysics simulation code," *Parallel Computing*, vol. 35, pp. 512–522, oct 2009.

[169] P. Tzeferacos, M. Fatenejad, N. Flocke, G. Gregori, D. Lamb, D. Lee, J. Meinecke, A. Scopatz, and K. Weide, "FLASH magnetohydrodynamic simulations of shock-generated magnetic field experiments," *High Energy Density Physics*, vol. 8, pp. 322–328, dec 2012.

[170] P. Tzeferacos, M. Fatenejad, N. Flocke, C. Graziani, G. Gregori, D. Lamb, D. Lee, J. Meinecke, A. Scopatz, and K. Weide, "FLASH MHD simulations of experiments that study shock-generated magnetic fields," *High Energy Density Physics*, vol. 17, pp. 24–31, dec 2015.

[171] G. Blaj, A. Dragone, C. J. Kenney, F. Abu-Nimeh, P. Caragiulo, D. Doering, M. Kwiatkowski, B. Markovic, J. Pines, M. Weaver, S. Boutet, G. Carini, C.-E. Chang, P. Hart, J. Hasi, M. Hayes, R. Herbst, J. Koglin, K. Nakahara, J. Segal, and G. Haller, "Performance of ePix10k, a high dynamic range, gain auto-ranging pixel detector for FELs," in *AIP Conference Proceedings*, Author(s), 2019.

[172] U. Zastrau, A. Woldegeorgis, E. Foerster, R. Loetzsch, H. Marschner, and I. Uschmann, "Characterization of strongly-bent HAPG crystals for von-Hamos x-ray spectrographs," *Journal of Instrumentation*, vol. 8, pp. P10006–P10006, oct 2013.

[173] M. P. Minitti, J. S. Robinson, R. N. Coffee, S. Edstrom, S. Gilevich, J. M. Glownia, E. Granados, P. Hering, M. C. Hoffmann, A. Miahnahri, D. Milathianaki, W. Polzin, D. Ratner, F. Tavella, S. Vetter, M. Welch, W. E. White, and A. R. Fry, "Optical laser systems at the Linac Coherent Light Source," *Journal of Synchrotron Radiation*, vol. 22, pp. 526–531, apr 2015.

[174] N. Otsu, "A Threshold Selection Method from Gray-Level Histograms," *IEEE Transactions on Systems, Man, and Cybernetics*, vol. 9, pp. 62–66, jan 1979.

[175] D. Foreman-Mackey, D. W. Hogg, D. Lang, and J. Goodman, "emcee: The MCMC Hammer," 2012.

[176] D. Foreman-Mackey, A. Price-Whelan, W. Vousden, G. Ryan, M. Pitkin, V. Zabalza, Jsheyl, Arfon Smith, G. Ashton, L. Singer, M. Smith, E. Rice, A. Deline, A. Nitz, B. J. Brewer, B. Sipöcz, D. W. Hogg, E. Gentry, H. Rein, Hennadii Madan, I. Czekala, NeutralKaon, J. Matthews, J. Tocknell, K. Barbary, , Marlon, R. Prechelt, S. M. C. Hair, and S. Hoyer, "dfm/corner.py: corner v2.2.2rc3," 2023.

[177] P. B. Johnson and R. W. Christy, "Optical Constants of the Noble Metals," *Physical Review B*, vol. 6, pp. 4370–4379, dec 1972.

[178] L. Alber, V. Scalera, V. Unikandanunni, D. Schick, and S. Bonetti, "NTMpy: An open source package for solving coupled parabolic differential equations in the framework of the three-temperature model," *Computer Physics Communications*, vol. 265, p. 107990, aug 2021.

[179] A. M. James and M. P. Lord, *Macmillan's chemical and physical data*. Macmillan, 1992.

[180] D. E. Gray, ed., *American Institute of Physics Hanbook*. McGraw-Hill, 3rd ed., 1972.

[181] M. Z. Mo, Z. Chen, R. K. Li, M. Dunning, B. B. L. Witte, J. K. Baldwin, L. B. Fletcher, J. B. Kim, A. Ng, R. Redmer, A. H. Reid, P. Shekhar, X. Z. Shen, M. Shen, K. Sokolowski-Tinten, Y. Y. Tsui, Y. Q. Wang, Q. Zheng, X. J. Wang, and S. H. Glenzer, "Heterogeneous to homogeneous melting transition visualized with ultrafast electron diffraction," *Science*, vol. 360, pp. 1451–1455, jun 2018.

[182] Z. Lin, L. V. Zhigilei, and V. Celli, "Electron-phonon coupling and electron heat capacity of metals under conditions of strong electron-phonon nonequilibrium," *Physical Review B*, vol. 77, feb 2008.

[183] N. Medvedev and I. Milov, "Electron-phonon coupling in metals at high electronic temperatures," *Physical Review B*, vol. 102, aug 2020.

[184] O. Karnbach, P. G. Heighway, D. McGonegle, R. E. Rudd, G. Gregori, and J. S. Wark, "Molecular dynamics simulations of inelastic x-ray scattering from shocked copper," *Journal of Applied Physics*, vol. 130, p. 125901, sep 2021.